HOKKAIDO UNIVERSITY

Title	Construction and Modification of Ternary Metal Sulfide for Efficient Photocatalytic CO_2 Reduction
Author(s)	王，琦
Degree Grantor	北海道大学
Degree Name	博士(理学)
Dissertation Number	甲第15409号
Issue Date	2023-03-23
DOI	https://doi.org/10.14943/doctoral.k15409
Doc URL	https://hdl.handle.net/2115/91500
Type	doctoral thesis
File Information	WANG_Qi.pdf

Hokkaido University Collection of Scholarly and Academic Papers : HUSCAP

Construction and Modification of Ternary Metal Sulfide for Efficient Photocatalytic CO_2 Reduction

(三元系金属硫化物の組成および表面構造制御による効率的な光触媒CO_2還元に関する研究)

Qi Wang

Graduate School of Chemical Sciences and Engineering

Hokkaido University

2023

Contents

Contents

Contents

Abstract

Photocatalytic carbon dioxide reduction is one of the most promising strategies to solve the energy crisis and achieve the global carbon cycle. Developing and designing highly efficient photocatalysts for photocatalytic CO_2 reduction under visible light has become a hot topic over the world. Metal sulfide-based materials have been widely used in photocatalytic CO_2 reduction due to their low cost, high stability, and suitable band structure. However, the metal sulfide photocatalysts still suffer obvious drawbacks, such as high photogenerated electron-hole pairs recombination rate, less reactive sites, and so on. To overcome these drawbacks, two fundamental strategies can be considered: the construction of suitable electronic structures and abundant reaction sites. Therefore, this thesis focuses on the rational design of metal sulfide photocatalysts with appropriate electronic structures by modifying the elemental ratio and constructing more reactive sites on the catalyst surface through surface engineering.

In chapter 1, a general background about semiconductor-based photocatalytic CO_2 reduction and the concept of photocatalysts were introduced. Then, the key factors and common strategies for enhancing photocatalytic activity were discussed. In the end, the ongoing research beyond ternary metal sulfide was summarized.

In chapter 2, the facile fabrication of Cd-In-S (CIS) colloidal nanocrystals was constructed as an efficient visible light-responsive photocatalyst for the conversion of CO_2 to CO. Both experimental and theoretical investigations reveal the importance of Cd to In ratio, which positively influences not only the charge carrier separation rate but also the electronic structures of the CIS samples. In particular, the light absorption ability, redox potential of photo-induced electrons, and charge transfer ability from CIS to the cobalt-based cocatalyst were effectively modulated, endowing the optimized sample with a high CO evolution rate of 22.9 μmol h^{-1} and selectivity up to 80% under visible light irradiation. This work's findings provide guidance for designing and constructing ternary metal sulfide materials for CO_2 conversion by modulating elemental ratio.

In chapter 3, the non-stoichiometric Ag-In-S quantum dots (QDs) was constructed as highly efficient and robust photocatalysts for visible-light-driven photocatalytic reduction of CO_2 to syngas at atmospheric pressure and room temperature. The introduction of $Co(bpy)_3^{2+}$ (bpy = 2’2-bipyridine) cocatalyst can promote the conversion of CO_2 to CO reaction and meanwhile improve the photo-stability of Ag-In-S QDs. The photocatalytic activity and selectivity of Ag-In-S QDs are strongly dependent on the Ag to In molar ratios, and the optimized sample exhibits the highest CO evolution rate of 9.20 μmol h$^{-1,}$ and H_2 evolution rate of 3.13 μmol h^{-1}, corresponding to the CO selectivity of 74.61%, outperforming most of the reported QDs based photocatalysts. This work provides a new example of Cd and Pb free QDs photocatalysts for efficient and stable CO_2 photoreduction.

In chapter 4, a $CdS_{0.8}CdSe_{0.2}$ colloidal quantum dot was prepared by a simple method as an excellent visible light reactive photocatalyst for the reduction of CO_2 to carbon monoxide. In addition, vacancy defects were created on the quantum dot surface by a simple acidic solution etching method to enhance the photocatalytic carbon dioxide reduction activity. The optimal sample exhibited the highest CO production rate of 19.79 μmol h^{-1} and selectivity of up to 77%. It can be demonstrated that the surface vacancy defects contribute to the outstanding performance of photocatalytic CO_2 reduction. In this paper, the role of the introduction of Cd vacancies in the photocatalytic CO_2 reduction activity is presented and discussed. This work provides guidance and theoretical insight for vacancy construction on QDs for potential photocatalytic CO_2 reduction.

In chapter 5, an overall summary of this dissertation work was presented. This thesis presents a systematic study on the elemental ratio modification of metal sulfides and their surface defects construction for efficient photocatalytic CO_2 reduction. By adjusting the proportion of metal elements in the ternary metal sulfide, the electronic structure of the catalyst can be effectively tuned, which is an effective way to improve photocatalytic performance. The construction of more reactive sites on the catalyst surface by surface etching can directly affect surface catalysis. The relevant findings of this study deepen the understanding of metal sulfide photocatalysts for CO_2 reduction.

Chapter 1 Introduction

1.1 Background of photocatalytic CO_2 reduction

In the last century, as human society has advanced, the demand for finite fossil fuels has risen. This has led to the release of substantial amounts of carbon dioxide during combustion, resulting in an increase in the concentration of carbon dioxide in the Earth's atmosphere. This increase has caused devastating consequences, including global warming, melting of polar ice caps, and rising sea levels.[1-5] In response, there is a growing interest in developing strategies to convert carbon dioxide from the atmosphere into renewable fuels, such as carbon monoxide, methane, methanol formate, and other hydrocarbons. This is considered to be one of the most promising approaches to address both the issue of reducing CO_2 concentration and the challenge of energy shortages.[6, 7]

Up to now, several technologies have been developed to convert carbon dioxide into hydrocarbon fuels and other chemicals. (1) biotransformation or biocatalysis using outdoor photobioreactor of microalgae; (2) chemical transformation through organic reaction or mineralization carbonation; (3) photochemical transformation; and (4) electrochemical transformation. [8] Among these methods, photocatalytic reduction of CO_2 to renewable fuels has many advantages and broad prospects, such as: (1) the original carbon source can be wasted CO_2 released from human activities; (2) the driving force (light) is renewable energy; (3) the catalytic conditions are relatively mild and controllable, such as controllable temperature and normal pressure; and (4) the carbon source can be utilized and recycled without secondary pollution. In short, by using photocatalytic reduction of carbon dioxide, the concentration of carbon dioxide can be reduced in the atmosphere in response to global warming while producing renewable fuels to alleviate the severe energy crisis under mild conditions. [9]

Linear CO_2 is quite stable among various carbon-contained chemicals due to its much larger bond energy of C=O (750 $kJ\cdot mol^{-1}$) than other carbon-contained bonds, such as C-H (411 $kJ\cdot mol^{-1}$), C-C (336 $kJ\cdot mol^{-1}$), and C=C (327 $kJ\cdot mol^{-1}$). [10] Thus, photocatalytic carbon dioxide reduction usually requires a lot of energy to overcome the C=O bond. It is the main challenge to achieving CO_2 reduction at the current stage.

1.2 Basic mechanism of photocatalytic CO_2 reduction

The photocatalytic reaction mechanism is based on the energy band theory of solid-state physics. The photocatalyst has a band structure consisting of a conduction band (CB), valence band (VB), and forbidden band (band gap). In low temperatures, the energy levels of VB are full of valence electrons, while there are few electrons in CB. The detailed process of photocatalyst can be explained as follows. When the photocatalyst receives the proton, whose energy is equal to or larger than its band gap, the electrons (e^-) in VB would be excited to CB, leaving the same number of holes (h^+) in VB. [11] The photo-generated electrons and holes will migrate to the surface of photocatalysts and participate the redox reactions with the adsorbent. At the same time, the photogenerated electron hole will also recombine the surface of photocatalysts under the electrostatic force. [12] In particular, photocatalytic CO_2 reduction mainly contains five steps as follows: [13]

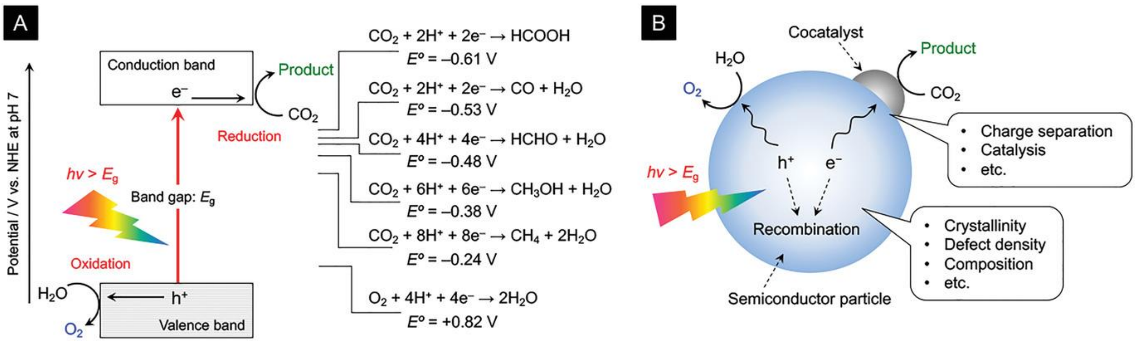

Figure 1.1 A) The illustration of redox potential for CO_2 reduction and water oxidation. B) The illustration of the total photocatalytic reaction process as well as the factors affecting the photocatalytic process. [2]

1) The adsorption of CO_2 on the surface of photocatalysts. As the initial step of the catalytic process, CO_2 adsorption as well as activation play an essential role in the subsequent CO_2 reduction reaction. On the one hand, if the catalyst surface has a good ability of CO_2 adsorption, the photogenerated electrons are more easily captured by the adsorbed CO_2 on the catalyst surface after migration from the catalyst inside to the catalyst surface, which can reduce the photogenerated electron-hole recombination rate and improve the efficiency of photogenerated electron utilization. [14] On the other hand, carbon dioxide as a very stable non-polar molecule has a linear structure whose high activation energy needs to be overcome, as we have mentioned. [15] After adsorption on the catalyst surface, CO_2 interacts with the surface atoms of the catalyst and becomes a

locally charged active species. Compared to CO_2, the charged CO_2 undergoes bending, and its LUMO energy level is lowered, further decreasing its energy barrier to accept electrons. [16] Moreover, the morphology of CO_2 adsorption on the surface of catalyst is determined by the chemistry property of the catalyst surface, which also has an essential influence on the subsequent photocatalytic reduction process.

2) Photogenerated carriers are generated in photoexcited semiconductors. The number of photogenerated carriers produced by semiconductor photocatalysts is decided by the energy of the excitation photons and its band gap. In contrast, the energy band edges of the semiconductor determine the redox ability. A positive VB edge of a semiconductor could lead to a strong oxidation ability of h^+, while a negative CB edge endows e^- with a strong reduction ability. [17] [18] Besides, the delocalization of the VB and CB would also influence the migration ability of e^- and h^+. These properties of band structure dramatically affect the photocatalytic ability. [19]

3) Migration of photoinduced electron-hole pairs to the catalyst surface. Since the rate of charge carriers recombination (~10^{-9} s) is much faster than the reaction rate (~10^{-3}-10^{-8} s), the quicker the migration of photogenerated carriers would lead to a lower chance of their recombination, indicating more effective photogenerated carriers could participate the photocatalytic reaction. [20]

4) The photogenerated carriers react with the adsorbed carbon dioxide and water on the catalyst surface. Theoretically, if the VB of the catalyst is higher than the redox potential required for water oxidation (E^{Θ} = 1.23 eV, vs. NHE), the holes diffusing to the surface of catalyst will oxidize the H_2O or hydroxyl groups and produce hydroxyl radicals ($\cdot OH$), H^+ and O_2. After the generation of H^+, it may further participate in the reduction reaction of CO_2 or may compete with CO_2 for electrons and be reduced to H_2.[21] Currently, the reaction of CO_2 reduction with H^+ is now agreed to be a multi-step reaction involving multiple electrons, with different reaction pathways, as shown in Table 1.1. [2] By promoting the oxidation reaction of water, it not only increases the consumption rate of photogenerated holes and inhibits the charge carriers recombination, but also provides abundant H^+ for the reduction of CO_2, thus increasing the reaction rate of CO_2 with H^+. [22]

5) Desorption of CO_2 reduction products. If the CO_2 reduction products are not desorbed from the catalyst surface in time, the active sites at the surface will be covered,

leading to a decreasing reaction cativity. Therefore, the desorption of the CO_2 reduction product also has an important influence on the yield of the product. [23] [24]

These five steps together determine the reaction kinetics of the catalyst photocatalytic reduction of CO_2 and the reaction products. If all five steps are carried out efficiently, excellent, and durable CO_2 conversion efficiency can be obtained.

Table 1.1 Possible CO_2 reduction pathway and their redox potential. [2]

Reactions	E^{Θ} (V) *vs*. NHE at pH=7
$CO_2+e^-\rightarrow CO_2^-$	-1.90
$CO_2+2H^++2e^-\rightarrow HCOOH$	-0.61
$CO_2+2H^++2e^-\rightarrow CO+H_2O$	-0.53
$CO_2+4H^++4e^-\rightarrow HCHO+H_2O$	-0.48
$CO_2+4H^++4e^-\rightarrow C+2H_2O$	-0.20
$CO_2+6H^++6e^-\rightarrow CH_3OH+H_2O$	-0.38
$CO_2+8H^++8e^-\rightarrow CH_4+2H_2O$	-0.24
$CO_2+9H^++9e^-\rightarrow C_2H_5OH+12OH^-$	-0.33

1.3 Photocatalysts for CO_2 reduction

The above discussions have indicated that the photocatalysis process contains five steps: CO_2 adsorption, photoinduced electron-hole generation, charge carrier migration, redox reaction on the surface, and product desorption. Accordingly, the promising photocatalysts have the following features: good CO_2 adsorption ability, suitable band structure, low charge carrier recombination rate, abundant surface active sites, and efficient product desorption ability. [25] In the past few decades, an enormous amount of photocatalysts have been put forward and used for photocatalytic CO_2 reduction reactions. According to composition of the material, I divided the photocatalysts for CO_2 reduction into the following categories: oxide photocatalysts, carbon contained photocatalysts, sulfide photocatalysts, and other photocatalysts.

1.3.1 Oxide photocatalysts for CO_2 reduction

Metal oxide photocatalyst is a large class of photocatalysts that have been widely investigated because of their low toxicity, cost effective, and chemical stability. Among the various oxide photocatalysts, TiO_2 is the photocatalyst that has been most studied since it was first reported by Fijishima and Honda. [21] [26] The photocatalytic reduction of CO_2 using TiO_2 suffers from low photoconversion efficiency due to its fast charge carrier recombination. Furthermore, bare TiO_2 can only utilize 5% sunlight for photocatalytic reactions due to its relatively large band gap value. Accordingly, the modification on TiO_2 photocatalysts mainly focuses on reducing the photogenerated electron-hole pairs recombination rate and energy band engineering. [27] Liu and coworkers described a La-modified TiO_2 (La-TiO_2) prepared by the sol-gel method for photocatalytic reduction of CO_2.[28] It was found that during the synthesis process, the La_2O_3 were generated on the TiO_2 surface. Due to the basic properties of La_2O_3, its presence could effectively adsorb CO_2 onto its surface, and the increase of CO_2 concentration on the TiO_2 surface was beneficial to promote the CO_2 reduction reaction. At the same time, a small fraction of La atoms was doped into the TiO_2 lattice by replacing Ti atoms. Due to the doping of La, the light absorption edge of La-TiO_2 was red-shifted compared to pristine TiO_2. Furthermore, the electron paramagnetic resonance (EPR) tests indicated that the surface Ti^{3+} sites were generated dur to the La modification, which facilitated the binding of CO_2 and the migration of charge carriers. The photocatalytic activity of La-TiO_2 for CH_4 production through CO_2 reduction was found to be 13 times higher than that of pristine TiO_2, as a result of the experiment.

Zinc oxide (ZnO) is typical non-titanium oxide, which has been extensively studied as a photocatalyst for carbon dioxide reduction due to its unique electronic structures. Up to now, developing and constructing ZnO-based photocatalysts using in CO_2 photoreduction have attached researchers’ attention. Similar to TiO_2, ZnO also suffers drawbacks, such as poor charge carrier mobility, high photogenerated electron-hole pairs recombination rate, and dissolution at acidic pH. Many strategies have been applied to moderate ZnO to enhance its photocatalytic ability to overcome these drawbacks. Doping ZnO with nonmetallic anions, such as carbon, nitrogen, sulfur, etc., is considered a useful method to improve the photocatalytic activity of ZnO by enhancing photogenerated electron-hole separation ability and increasing light absorption. Recently, Oliveira and coworkers reported a nitrogen-doped zinc oxide as efficient photocatalyst for CO_2 reduction.[29]

They indicated that the O atoms were partially substituted by N, causing changes in the crystallinity of ZnO, leading to an efficient photocatalytic CO_2 reduction by the presence of exposed surface active sites in the photoreduction reaction. These surface exposed active centers generated more structural defects, further improving the carrier kinetic reaction. As a result, CH_4 production rate as high as 0.21 mol $L^{-1}g^{-1}h^{-1}$ was obtained after 24 h of reaction of the 2 wt% N-ZnO photocatalyst in a NaOH solution at 40 °C under UV-Vis light irradiation (254-400 nm).

In summary, metal oxide photocatalysts are mainly limited by insufficient charge carriers separation ability and broad band gap. Even though TiO_2 photocatalysts have been extensively investigated, other metal oxides are still far from industrial applications due to various drawbacks.

1.3.2 Carbon-contained photocatalysts for CO_2 reduction

Carbon-contained photocatalysts, such as Ti_3C_2, MoC, and carbon nitride, have received increasing attention due to their cost-effectiveness, chemical stability, good electrical conductivity, and easy preparation. The potential applications of these materials in CO_2 photoreduction have been widely studied. Graphitic carbon nitride (g-C_3N_4), since it was first reported in 2009, it has received the most attention and become one of the hottest fields in photocatalytic hydrogen generation. Compared to other widely investigated photocatalysts, graphitic carbon nitride is usually regarded as an environment-friendly and sustainable photocatalyst for CO_2 reduction. [30] For example, g-C_3N_4 shows chemical stability in aqueous and organic solvents and can be easily prepared from commercial chemicals (such as melamine, urea, and pyridine) with a high production yield. Meanwhile, as a member of 2-dimensional semiconductors, g-C_3N_4 also has a large specific surface area, exposing abundant possible active sites and adsorption sites. However, g-C_3N_4 still suffers from low photocatalytic activity, low visible light utilization, and so on. For further improving the photocatalytic performance of g-C_3N_4, many strategies have been applied to modify its band structures, morphologies, and active sites.

Tang and co-workers [31] applied the in-situ hydrothermal deposition method for synthesizing the Mg-doped g-C_3N_4, which showed a broadened light absorption region and longer charge carrier lifetime compared to pristine g-C_3N_4. They revealed that the Mg atom acted as the electron mediate for enhancing the electron-hole separation ability and reduce the photogenerated electron-pair recombination rate (Figure 1.2a). The optimal sample showed CH_4 production of 17.09 μmol g^{-1} and CO production of 4.13 μmol g^{-1} under 6h irradiation, which was about 1.96 and 2.8 times compared to those of pure g-C_3N_4. From Tang's work, we could know that element doping as efficient method successfully modulate and enhance the photocatalytic activity. Meanwhile, structural design and noble metal loading are two effective methods to modify g-C_3N_4. As a typical instance, Tu et al. [32] reported the g-C_3N_4 with controllable N vacancies by heating pristine g-C_3N_4 at different temperatures under hydrogen fluent. As shown in Figure 1.2b, the characterization and DFT calculation revealed that there was an intermediate energy level generated below the conduction band edge caused by nitrogen vacancies. As a result, the photogenerated electrons could be more easily excited to CB or intermediate level, which could enhance the electron-hole separation ability. The optimal g-C_3N_4 nanosheets with the nitrogen vacancies exhibited an AQY of 4.2% at 420 nm and showed five times activity of CO_2 reduction compared to bulk g-C_3N_4. Another typical work reported by Sun and co-authors demonstrated Pt nanoparticle loaded g-C_3N_4 for selectively reducing CO_2 to CH_4 with H_2O. [33] The authors unraveled that Pt-support electronic interaction between the nanoparticle and g-C_3N_4 improved the electron transfer between g-C_3N_4 to the Pt nanoparticle. Moreover, the competitive H_2 generation reaction was completely suppressed by forming Pt^{2+} species on the Pt nanoparticle. As a result, a CH_4 production rate as high as 14.8 μmol g^{-1} h^{-1} with 100% selectivity was obtained under the optimal sample.

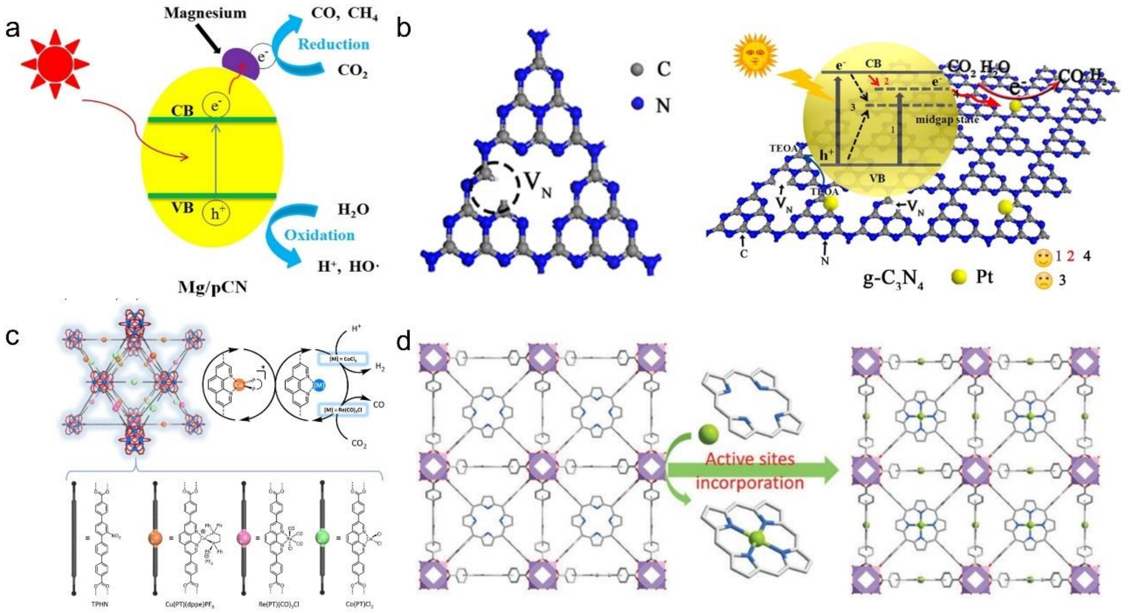

Figure 1.2 (a) Proposed mechanism for the photocatalytic CO_2 reduction and H_2O

oxidation on Mg/p-CN photocatalyst. [31] (b) The model of nitrogen vacancies in g-C_3N_4. (c) Schematic illustration of g-C_3N_4 with nitrogen vacancies (VN) for photoreduction of CO_2 to CO and H_2 evolution. [32] (d) Illustration of frame structures and linked ligands of mPT-Cu/Re MOFs and mPTCu/Co. [34] (e) A three-dimensional network of MOF-525-Co is shown, highlighting its highly porous framework and integrated active sites.[35]

Metal-organic frameworks (MOFs) are carbon-containing materials that have been extensively studied for their potential use in photocatalytic CO_2 reduction. They are constructed from metal ions or clusters that are linked together with organic linkers.[36] MOFs can be used in photocatalysis due to their following features: tunable light absorption ability with a wide light absorption range, controllable electron-hole separation ability; good CO_2 adsorption ability; well-dispersed active sites, and so on. Recently, MOFs have been widely investigated as promising candidates for photocatalytic CO_2 reduction and got the great achievements. The designing and modification of MOFs for efficient photocatalytic CO_2 reduction mainly focus on the selection and modulation of metal clusters as well as organic linkers. As a typical work, Feng and co-workers designed a multifunctional zirconium polyphenolate-decorated-(metallo) porphyrin MOF containing Cu photosensitizers and Re catalysts. [34] The designed MOF with electron-rich conjugated porphyrin linker centered with Co-metallation showed excellent CO_2 adsorption ability and photocatalytic CO_2 reduction to CO rate of 14 μmol $g^{-1}h^{-1}$ without loading any cocatalysts under visible light irradiation as shown in Figure 1.2c. The ESR study and theoretical calculation unraveled that the metalloporphyrin in the designed MOF was the most critical factor for enhancing CO_2 adsorption ability to improve photocatalytic CO_2 reduction. Another representative work reported by Zhang et al. demonstrated a porphyrin-based MOF (MOF-525(Zr)-Co) with Co single atom for efficient CO_2 reduction to CH_4. (Figure 1.2d) [35]. The mechanism study indicated that the single atom Co could receive excited electrons from porphyrin units due to its unsaturated coordination to accelerate the CO_2 reduction reaction. As a result, the CH_4 production rate reached as high as 36.67 mmol $g^{-1}h^{-1}$.

1.3.3 Sulfide photocatalysts for CO_2 reduction

The catalytic activity of sulfide-based photocatalytic materials is very promising. In the past few decades, there have been many reports about metal sulfide photocatalysts used for CO_2. As shown in Figure 1.3, almost all sulfide photocatalysts are composed of metal cations in the d10 configuration. The conduction band is generally formed of d or sp orbitals of metal elements, while the valence band is usually formed by S3p orbitals. This composition makes metal sulfides suitable energy edges, wide light response region, and fast charge carrier migration ability, which is suitable for photocatalytic CO_2 reduction. Furthermore, compared to previously mentioned metal oxides and carbon-contained photocatalysts, metal sulfide photocatalysts have narrower band gaps and abundant active sites, which could be used as photocatalysts directly in photocatalytic CO_2 reduction. Metal sulfides can be classified into binary, ternary, and polynary metal sulfides based on their composition. The following mentioned works are summarized in Table 1.2.

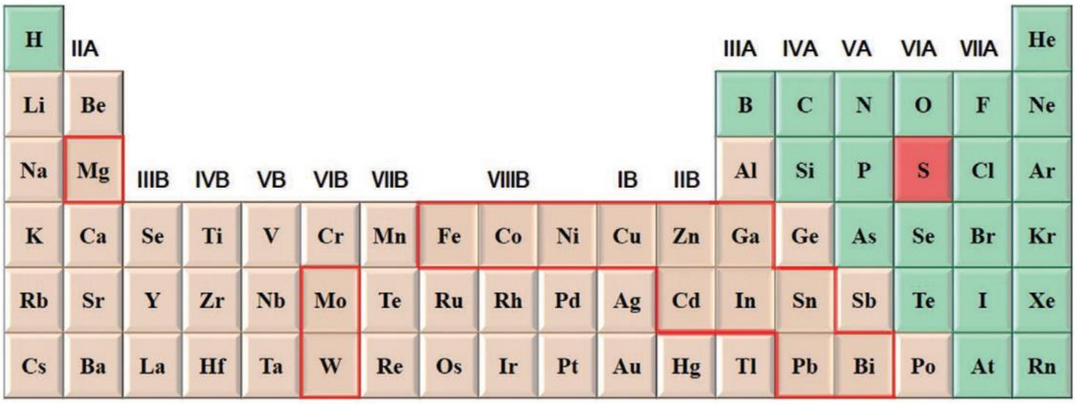

Figure 1.3. Chemical elements can be utilized to construct metal sulfide photocatalysts for CO2 reduction.[37]

Table 1.2 Systematic summary of metal sulfide photocatalysts for CO_2 photoreduction.

Family	Photocatalyst	Reactant	Light source	Product	Production rate	Ref.
IIB-VIA	hollow CdS particle	$Co(bpy)_3$ H_2O TEOA	300W Xe lamp	CO H_2	3758 μmol g^{-1} h^{-1} 1588 μmol g^{-1} h^{-1}	[38]
	CdS/TiO_2	$NaHCO_3$ H_2O	LED lamps	CH_4	11.9 mmol g^{-1} m^{-2}	[39]
	Cd^{2+} modified ZnS	K_2SO_3 H_2O $KHCO_3$	200 W Hg-Xe lamp	HCOOH CO H_2	11.19 mmol g^{-1} h^{-1} 0.05 mmol g^{-1} h^{-1} 0.54 mmol g^{-1} h^{-1}	[40]
	ZnS with Zn vacancies	K_2SO_3 H_2O $KHCO_3$	300W Xe lamp	HCOOH CO H_2	6.2 μmol h^{-1} 0.04 μmol g^{-1} h^{-1} 1.5 μmol g^{-1} h^{-1}	[41]
	$Cd_{1-x}Zn_xS$	H_2O	LED lamps	CH_4 CO H_2	0.22 μmol g^{-1} h^{-1} 2.9 μmol g^{-1} h^{-1} 0.16 μmol g^{-1} h^{-1}	[42]
IIB-IIIA-VIA	$ZnIn_2S_4$ layer with Zn vacancies	H_2O	300W Xe lamp	CO O_2	33.2 μmol g^{-1} h^{-1} 13.7 μmol g^{-1} h^{-1}	[43]
	$Zn_xIn_2S_{3+x}$, (x=1–5)	H_2O	300W Xe lamp	CO	40.4 μmol g^{-1} h^{-1}	[44]
	In_2S_3-$CdIn_2S_4$	$Co(bpy)_3$ H_2O TEOA	300W Xe lamp	CO H_2	825.4 μmol g^{-1} h^{-1} 260 μmol g^{-1} h^{-1}	[45]
	$CdIn_2S_4/ZnIn_2S_4$	$Co(bpy)_3$ $KHCO_3$ TEOA	300W Xe lamp	CO H_2	1194.5 μmol g^{-1} h^{-1} 475.7 μmol g^{-1} h^{-1}	[46]
I-III-VI	$TiO_2/CuInS_2$	H_2O $NaHCO_3$ H_2SO_4	350W Xe lamp	CH_4 CH_3OH	2.5 μmol g^{-1} h^{-1} 0.86 μmol g^{-1} h^{-1}	[47]
I-II-IV-VI	Cu_2ZnSnS_4	H_2O	Xe lamp AM 1.5 filter	CH_4	118.75 ppm g^{-1} h^{-1}	[48]
	$WO_3/TiO_2/Cu_2ZnSnS_4$	H_2O	400W Xe lamp	CO CH_4	26.6 μmol g^{-1} h^{-1} 2.47 μmol g^{-1} h^{-1}	[49]

Binary metal sulfides are a series of chemicals which is composed by a metal element as well as sulfur. They have attracted much attention because of their simple geometry structure, facile synthesis, and photoluminescence properties. [50, 51] As shown in Figure 1.4a, binary metal sulfides usually show cubic zinc-blende and hexagonal wurtzite. [52]Among the various binary metal sulfides, CdS is the most investigated metal sulfide with many advantages, such as narrow band gap, negative CB position, and also abundant exposed active sites (Cd atoms) for photocatalytic CO_2 reduction. [53, 54] As a result, CdS-based materials have achieved fruitful results in visible light-driven catalytic reactions, such as the hydrogen generation reaction and the reduction of carbon dioxide into hydrocarbon fuels. However, severe photocorrosion during the photocatalytic process dramatically frustrates the photoactivity of CdS. In addition, the charge separation rate of pristine CdS still should be improved. Therefore, many strategies have been carried out to enhance the photocatalytic performance, selectivity, and stability of CdS in the conversion of CO_2 into solar fuels. Typically, Zhang et al. [38] designed a unique hollow structured CdS in spheres and applied it in photocatalytic carbon dioxide reduction, as shown in Figure 1.4b. Benefiting from the designed hierarchical topology, the highest CO production rate as high as 1337 μmol g^{-1} h^{-1} was achieved with $Co(bpy)_3^{2+}$as cocatalyst under visible light irradiation, other phases of CdS showed a relatively lower photocatalytic activity. Furthermore, the CO production rate was further improved to 3758 μmol g^{-1} h^{-1} after loading an golden cluster as a co-catalyst (0.25 wt% optimized deposition). Another representative work reported by Low and co-workers [39] described a membrane-like CdS nanosheets and TiO_2 composite, which was applied in the photoreduction of CO_2 to CH_4 reactions. They used in-situ irradiated X-ray photoelectron spectroscopy (ISI-XPS) techniques, and first principle calculation to reveal that the photogenerated electron-hole pair migration follows a typical Z-scheme pathway, caused by the internal electric field. (Figure 1.4c) As shown in Figure 1.4d, the formation of heterojunction in Z-scheme enabled the CdS/TiO_2 catalyst to efficiently extract photogenerated carriers and maintain enhanced redox properties. As a result, excellent CO_2 photoreduction performance was achieved with a CH_4 formation rate of 11.9 mmol h^{-1} m^{-2} under simulated solar light irradiation, which is 6.4 times compared to the performance of pristine TiO_2.

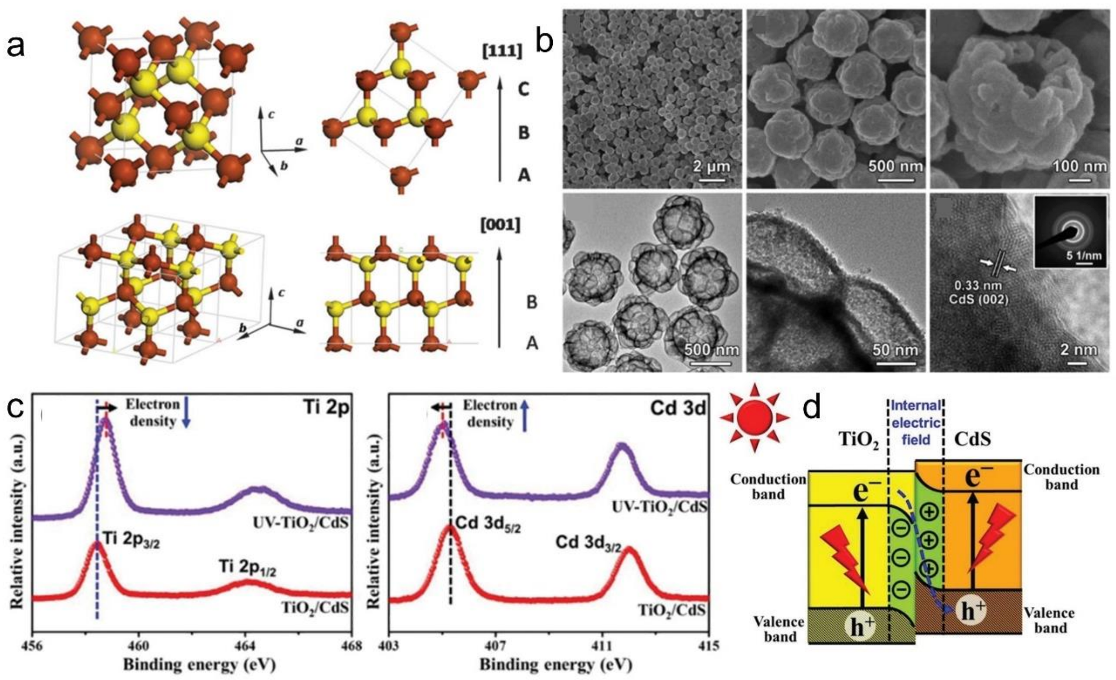

Figure 1.4 (a) A diagram shown to illustrate the crystal structures of zinc-blende and wurtzite.[52] (b) FESEM images, TEM images, and SAED pattern of CdS sample. [38] (c) XPS spectra of Cd 3d states and Ti 2p states of TiO_2/CdS sample. (d) A schematic is presented to demonstrate the migration of charge carriers on TiO_2/CdS under the influence of an internal electric field. [39]

As another IIB-VIA binary metal sulfide, the ZnS with direct band gap has been much investigated in the application of photocatalysis. [55-57] Figure 1.5a shows two main polymorphs of ZnS, namely zinc blende with a band gap of 3.72 eV and wurtzite with a band gap of 3.77 eV. [58] The former has a band gap of 3.72 eV. In 1998, Fujiwara et al. demonstrated the ability of colloidal ZnS nanocrystals to form CO_2 photoreduction to CO and formate ($HCOO^-$). [59] To date, much research on the application of ZnS nanocrystals in CO_2 reduction has focused on achieving high catalytic efficiency. For example, our group reported a Cd^{2+}-modified colloidal ZnS photocatalyst. [40] Cd^{2+} grafted on ZnS nanocrystals successfully trapped photogenerated electrons and participated in the photoreduction of CO_2, obtaining higher total yields of CO and HCOOH as high as 11.19 mmol g^{-1} h^{-1} and a high apparent quantum efficiency of 76% at 280 nm. (Figure 1.5b) Another representative work reported by our group was using a simple acid etching treatment on ZnS nanocrystal to achieve a high HCOOH production rate and a high selectivity of 86.6%.[41] They used ESR measurement and EDS test to confirm the generation of Zn vacancies. Finally, the theoretical study indicated that the generated Zn vacancies could be carried out as active sites for carbon dioxide reduction while suppressing competitive H_2 generation reaction. (Figure 1.5c)

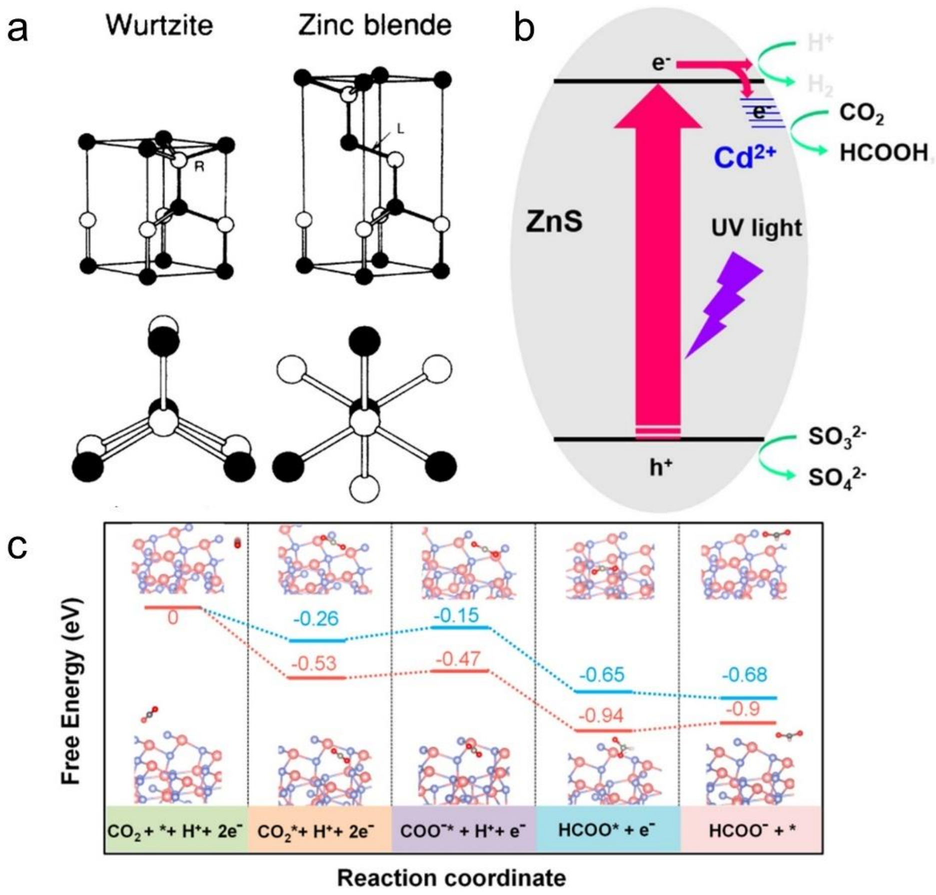

Figure 1.5 (a) Three perspectives of the crystal structures of zinc-blende and wurtzite.[58] (b) Illustration of how the Cd^{2+} cocatalyst promotes the separation of photo-generated electrons and enhances the selectivity of CO_2 reduction towards HCOOH. [40] (c) A diagram depicting the free energy pathways for the conversion of CO_2 into formate on a pristine ZnS surface and a V_{Zn}-ZnS surface. [41]

Besides binary metal sulfides, ternary metal sulfides (TMSs) are showing more and more potential for the photocatalytic CO_2 reduction. TMSs are a series of metal sulfides that are composited by three elements. Compared to binary metal sulfides, TMSs show more possibility in band structure engineering by composition modification. I divide the TMSs photocatalysts into the following types according to their elemental composition: IIB-VIA, IIB-IIIA-VIA, and IB-IIIA-VIA. [60, 61]

IIB-VIA (IIB=Cd, Zn; VIA=S, Se, Te) ternary sulfide is the solid solution of IIB-VIA photocatalyst, such as $Cd_xZn_{1-x}S$, CdS_xSe_{1-x}, and so on. It is widely accepted that IIB-VIA-VIA and IIB-IIB-VIA solid solution photocatalysts always show better activity than pristine IIB-VIA photocatalysts. [62, 63] Kozlova et al. reported $Cd_{1-x}Zn_xS$ solid solutions by a simple two-step technique for efficient photocatalytic CO_2 reduction. [42] The $Cd_{1-x}Zn_xS$ solid solutions showed a highly elemental ratio dependent activity, and the $Cd_{0.94}Zn_{0.06}S$ possessed the highest photocatalytic CO and CH_4 generation ability, which was about twice and four times than those of CdS and ZnS, respectively.

IIB-IIIA-VIA have become promising catalyst for CO_2 photoreduction because of unique photoelectric properties, controllable band structure, rapid electron migration ability, and high stability compared to other ternary metal sulfide. To achieve valence symmetry in the configuration of ternary metal sulfide, the S in the IIB-IIIA-VIA usually exists in the reduced state of -2. At the same time, cation IIB exhibits an oxidation state of +4 or +2, while cation IIIA has an oxidation state of +2 or +3. Thus, IIB-IIIA-VIA usually shows the ionic structure of IIB-IIIA$_2$-VIA$_4$. In addition, the presence of p-blocking ions withd10 conformation (e.g., In^{3+}) gives IIB-IIIA-VIA excellent photocatalytic properties. Therefore, extensive studies have focused on IIB-IIIA-VIA photocatalysts (e.g., $ZnIn_2S_4$, $CdIn_2S_4$, $CaIn_2S_4$, etc.) to enhance the performance of CO_2 photoreduction.

$ZnIn_2S_4$ is a typical IIB-IIIA-VIA sulfide. Because of its suitable band gap and remarkable chemical stability, it has been widely investigated. [64-66] In the typical layered $ZnIn_2S_4$ in hexagonal structure, all atoms located along the c-axis. The Zn and S atoms are bound to form ZnS_4 unit, while the In and S atoms form InS_4 unit or InS_6 unit. (Figure 1.6a) The construction of nanoscale Zn vacancies on a single cell $ZnIn_2S_4$ layer surface with an very thin thickness of 2.46 nm was cleverly achieved via a simple tunable method by Jiao et al. [43] (Figure 1.6b and c) In ZIS samples with high concentrations of zinc vacancies, photoexcited electrons were transferred from the conduction band of as-prepared $ZnIn_2S_4$ to Zn vacancy traps extremely fast (≈15 picosecond) and a prolonged photogenerated electron-hole lifetime was achieved, elucidating the enhanced charge carrier lifetime and charge migration ability. (Figure 1.6d) Thus, the $ZnIn_2S_4$ with abundant Zn vacancies on the surface exhibited a high CO production rate as high as 33.2 $\mu mol\ g^{-1}\ h^{-1}$. Wu et al. found that structural defects caused by non-chemical components were shown a bad influence on the separation and migration of photoinduced electrons and holes. [44] With more Zn/In ratio, defects caused by non-chemical components lead to a wider band gap, which hinders the separation of photoinduced electron-hole. The kinetics of the photoinduced electron-hole are suppressed because of the energy barrier caused by geometry defects of the $Zn_xIn_2S_{3+x}$ photocatalyst. Thus, perfect structural ZIS catalysts showed the best CO_2 photoreduction performance under visible light. (Figure 1.6e)

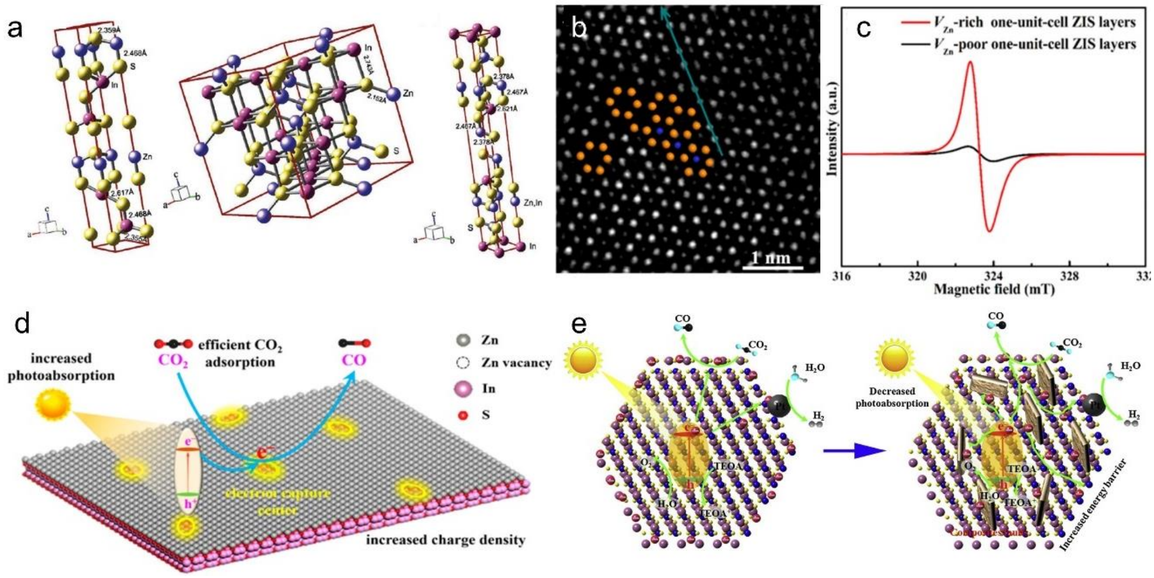

Figure 1.6 (a) View of structures of hexagonal, cubic, and rhombohedral $ZnIn_2S_4$. [67] (b) High-Angle Annular Dark Field Scanning-STEM images and (c) EPR spectra of V_{Zn}-poor and V_{Zn}-rich $ZnIn_2S_4$ layers. (d) Illustration of the photocatalytic carbon dioxide reduction to carbon monoxide on the V_{Zn}-rich $ZnIn_2S_4$ layers. [43] (e) Illustration of mechanism in our photoreduction of CO_2 with or without composites faults.[44]

As one of the critical components of the IIB-IIIA-VIA sulfides, the semiconductor $CdIn_2S_4$ [68-71] shows a cubic spinel configuration whose space group is Fd3m. The S atom is linked to the Cd atoms to form the CdS_4 tetrahedron, while it is coordinated to the In atom to forms the InS_6 octahedron (Figure 1.7a). The investigation of the electron distribution characteristics of $CdIn_2S_4$ found that the energy levels of the conduction band are formed by the states of the 5s and/or 5p orbitals of the Cd and In atoms. At the same time, the edge of the valance band is composed of electron states of the S 3p orbitals. Because of its suitable band gap of about 2.3 eV and broad photoresponsive area, $CdIn_2S_4$ has been studied by researchers in a series of photooxidation reaction applications, such as H_2 production, CO_2 reduction, and bacterial inactivation. Currently, the works using

$CdIn_2S_4$ for photocatalytic CO_2 reduction mainly focus on the construction of $CdIn_2S_4$-based heterojunction. The representative work described by Wang and co-workers demonstrated a hierarchical In_2S_3-$CdIn_2S_4$ heterostructure nanotube as a catalyst for photocatalytic CO_2 reduction. [45] (Figure 1.7b and c) The optimal sample showed about 13 times compared to the activity of In_2S_3. They indicated that the superior photocatalytic performance can be attributed to the unique heterojunction with a extended specific surface area and charge carrier separation ability. Recently, Zhang and co-works constructed $CdIn_2S_4/ZnIn_2S_4$ heterojunction as an effective catalyst using in photocatalytic CO_2 conversion. [46] The best sample exhibited a CO production rate of 1194.5 μmol g^{-1} h^{-1}, 62.2% higher compared to the activity of pristine $CdIn_2S_4$. The mechanism study confirmed that the improved photocatalytic activity came from abundant vacancies and Z-scheme transfer mode. (Figure 1.7d and e)

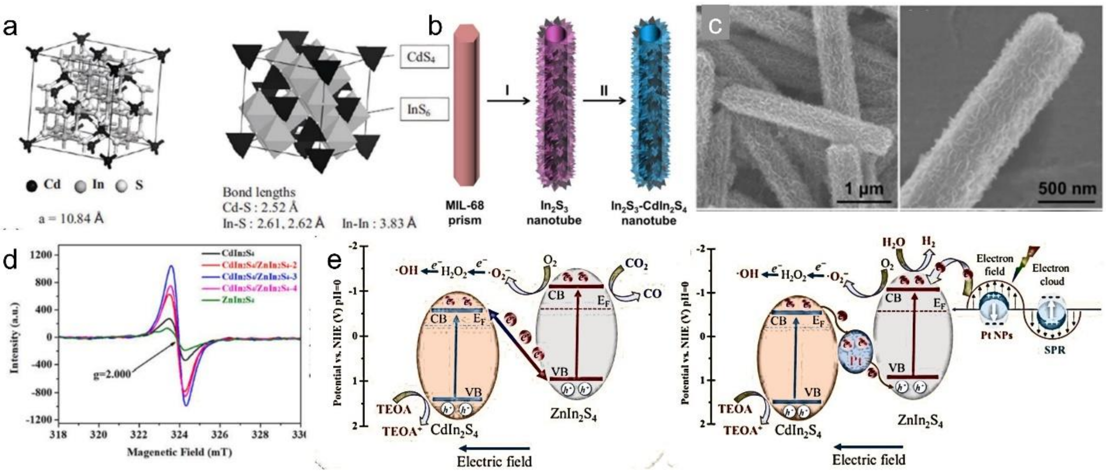

Figure 1.7 (a) Crystal structures of $CdIn_2S_4$. [37] (b) The illustration of the synthesize process of the hierarchical In_2S_3-$CdIn_2S_4$ heterostructured nanotube. (c) FESEM images of hierarchical In_2S_3-$CdIn_2S_4$ nanotubes,[45] (d) EPR spectra of the as-prepared photocatalysts. (e) Proposed Z-scheme charge transfer for (a) $CdIn_2S_4/ZnIn_2S_4$ and (b) $CdIn_2S_4/ZnIn_2S_4$-4/Pt.[46]

Ternary metal sulfide IB-IIA-VIA, in which IB is Cu or Ag, IIIA is Al, In or Ga; VIA is S, has also been widely studied as semiconductor photocatalysts and attracted great interest in the industrial field. These ternary sulfides are usually used as light absorbers for solar cells or photoelectrochemical devices due to their suitable band gaps of 0.8 eV to 2.0 eV. Especially $CuInS_2$ and $AgInS_2$, they have widely used for photocatalytic applications.

Cu-In-S contains three typical crystal structure, including the chalcopyrite structure, the cubic zinc-blende structure, and the hexagonal wurtzite structure. (Figure 1.8a) In general, the chalcopyrite structure of $CuInS_2$ prefer to form below 1253 K, while the remained 2 phases could be high-energy metastable states that transform from the chalcopyrite phase at high temperatures. Because of the narrow band gap, $CuInS_2$ based photocatalysts are developed as highly promising and sustainable catalysts in application of photocatalytic H_2 generation, CO_2 conversion, and pollutant degradation. [72-74] Xu et al. using a hydrothermal route synthesized TiO_2 nanofibers coated with $CuInS_2$ nanosheets as thin as 10 nm, which exhibited excellent reduction performance towards CO_2, producing CH_4 or CH_3OH (Figure 1.8b). [47] A maximum CH_4 production rate of 2.5 μmol h^{-1} g^{-1} and only a very small amount of methanol (0.86 μmol h^{-1} g^{-1}) was achieved via TiO_2 with an optimum support of $CuInS_2$ (2.5%). The result indicated that the formation of $TiO_2/CuInS_2$ heterojunction is able to facilitate charge migration and extraction during photoexcitation, thereby increasing the yield of CO_2-reduced hydrocarbons. (Figure 1.8c)

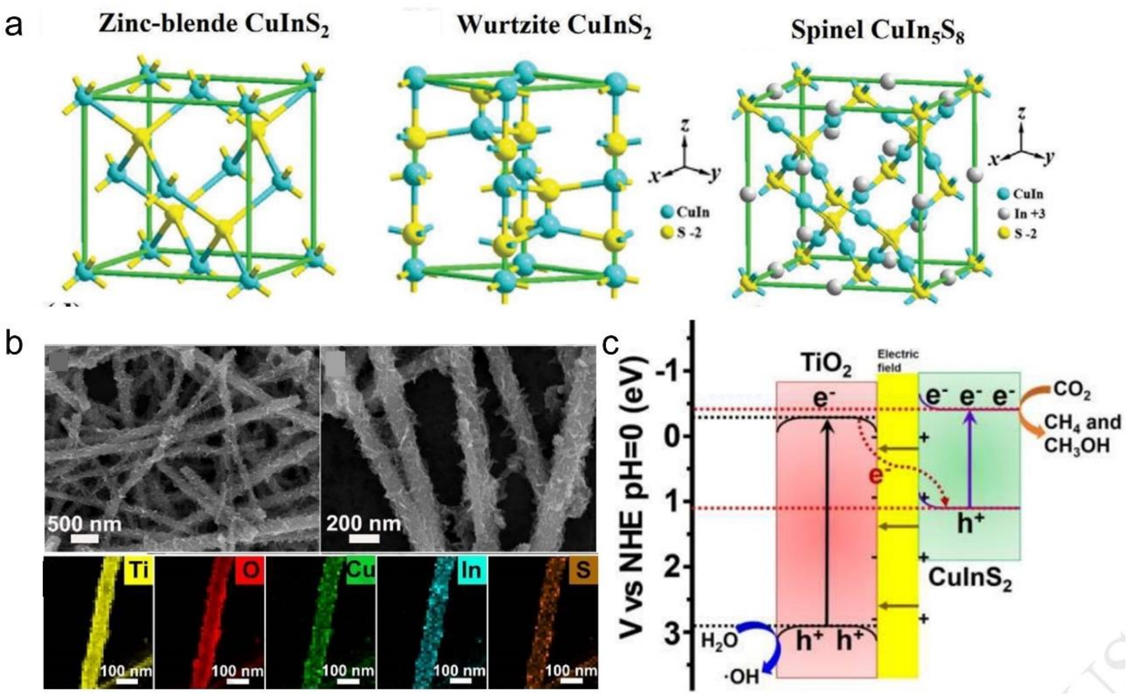

Figure 1.8 (a) structural models of zinc-blende $CuInS_2$, wurtzite $CuInS_2$, spinel $CuIn_5S_8$. [37] (b) SEM images of each samples. Energy dispersive spectrometry mapping of titanium, oxygen, copper, indium, and sulfur elements of selected sample. (c) Schematic illustration of the photoinduced charge carrier migration in $CuInS_2/TiO_2$ after light irradiation.[47]

Until now, polynary metal sulfides for photocatalytic CO_2 reduction have been investigated limited due to the difficulty of their synthesize process, complex structure, and composition. However, the representative sulfides of the I_2-II-IV-VI_4 family, the significant progress in solar photovoltaics of Cu_2ZnSnS_4 (CZTS) semiconductors has been widely studied due to their environmental friendliness, unique photovoltaic properties, and narrow band gap (≈1.5 eV). [75] (Figure 1.9a) DFT calculations on the band structure of Cu_2ZnSnS_4 indicate that the ideal positions of conduction band edge and valance band edge are favorable for photocatalytic CO_2 reduction and the water oxidation. [76] As a representative work, Kim et al. [48] constructed polycrystalline CZTS-coated TiO_2 by a double process of thermal injection method and annealing treatment. The introduction of Cu_2ZnSnS_4 significantly extended the photoresponse range, which could promote the performance of the CZTS/TiO_2 composite catalyst in the photoreduction of CO_2. Furthermore, the extended specific surface area caused by the mesoporous structure generated after annealing treatment. Meanwhile, the improved electron-hole migration due to the inert electric field of the p-n heterojunction is also critical reason contributing to photocatalytic performance. (Figure 1.9b) Recently, a ternary hybrid heterojunction WO_3/TiO_2/CZTS was prepared by Raza and co-workers. [49] In this experiment, the best CO_2 photoreduction activities, respectively achieved CO generation of 26.6 and hydrogen generation of 2.47 μmol g^{-1} h^{-1}, with an AQE of 0.52%. (Figure 1.9c) In addition, combining CZTS and broadband ZnO semiconductors to form Z-junctions is also considered a promising method to improve the photogenerated electron-hole migration ability and further enhance the photoreduction activity. (Figure 1.9d) The CZTS/ZnO photocatalyst exhibited higher CH_4 evolution efficiency as high as138.90 ppm g^{-1} h^{-1}, 31 times higher compared to the activity of pristine ZnO nanorods under simulated light.

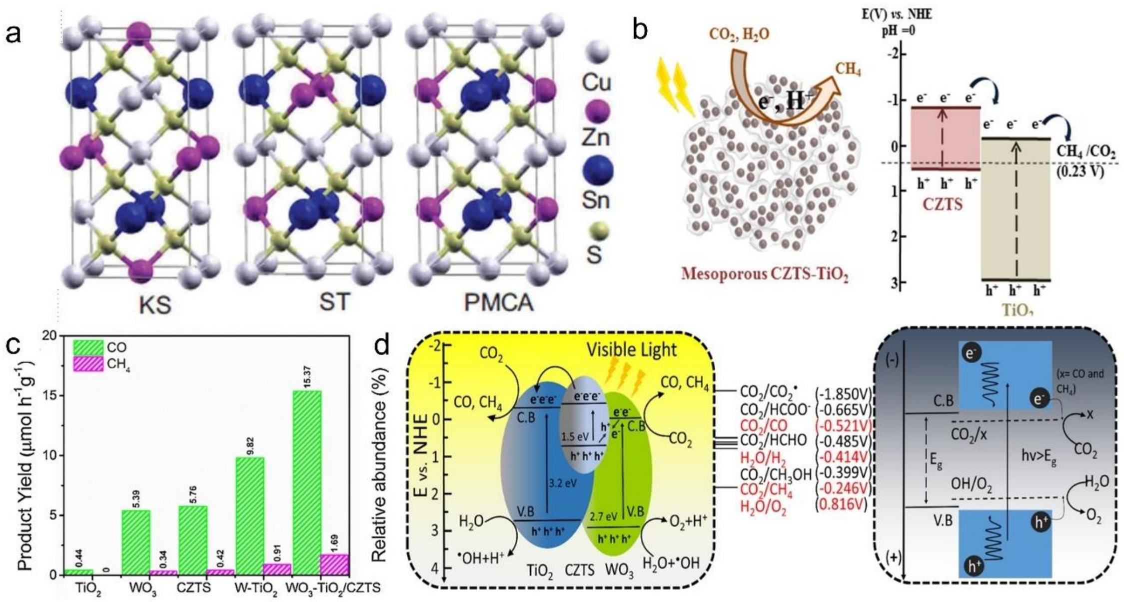

Figure 1.9 (a) The crystal structure of Cu_2ZnSnS_4 in 3 typical structure, including KS, ST as well as PMCA.[77]. (b) Schematic illustration for detailed mechanism of charge carrier migration and surface reaction of CZTS-TiO_2 samples. [48] (c) The yield rates over the as-prepared sample. The detailed mechanism of charge carrier migration and surface reaction of over the WO_3-TiO_2/CZTS heterostructure. [49]

1.4 Modification of metal sulfide photocatalyst

Currently, the photocatalytic $CO_{2\ \mathrm{reduction}}$ activity by metal sulfide still falls short of satisfactory levels for practical applications. In order to improve the photoreduction of CO_2 ability of metal sulfide photocatalysts, the following points can be considered: improve the separation and transfer of charges, construct more active sites, promote light absorption, optimize the position of the band gap, reduce cost and toxicity, and improve cycle stability. In order to achieve the above goals, a series of semiconductor modification methods have been studied, including modifying the crystal structure and morphology, loading co-catalysts, building heterostructures with other semiconductors, energy band engineering, forming solid solutions, and so on. Recently, many researchers used these methods to enhance the catalytic CO_2 photoreduction performance and stability of metal sulfide photocatalysts, and outstanding results have been achieved. In this section, I will discuss some important and representative strategies in detail with some typical examples.

1.4.1 Surface engineering

For semiconductor photocatalysts, the microstructure is directly related to absorption of light irradiation, the surface area between the reactants (CO_2, H_2O, and so on), and the exposure of the reaction sites. By surface engineering, such as morphology modulation or defect engineering, the activity of the catalyst can be effectively increased. [78, 79] For instance, by introducing cation or anion vacancies to photocatalysts, both the band structure and the electron-hole separation ability could be tuned effectively to control the performance of the photocatalyst. In addition to defect engineering, morphology modulation is another widely used surface engineering method for modifying photocatalysts. For example, by exposing different facets of photocatalysts, the photocatalytic performance could be influenced dramatically because of the different structural geometry and band structures. In consequence, surface engineering is widely carried out for the enhancement of metal sulfide photocatalysts for improving their photocatalytic efficiency.

Lou's group designed heterogeneously structured $ZnIn_2S_4/In_2O_3$ catalysts as potential candidates for solar-driven sustainable and efficient CO_2 photoreduction reactions. [80] The designed complex hollow scaffolds with bifacial heterogeneous shells as well as ultrathin 2D nanosheet units greatly facilitate the migration of photoinduced electrons and holes, enhancing CO_2 adsorption ability and exposing a wealth of active sites for catalytic reaction on surface. Therefore, the best $ZnIn_2S_4$-In_2O_3 sample exhibits excellent activity in carbon dioxide deoxygenation reduction and a relatively high CO production rate as high as 3075 μmol $h^{-1}g^{-1}$. As a representative work focused on morphology modulation, Wang et al. designed the cadmium sulfide nanosheets (CdS NSs) whose terminal planes were mainly S^{2-}layers along out-of-plane [001] direction as efficient photocatalysts. [81] The prepared sample showed remarkable photocatalytic performance of CO evolution rate as high as 2.13 mol g^{-1} h^{-1} while the selectivity of CO reached 99%. Moreover, a high AQE of 42.1% was achieved using light from the AM 1.5G simulator. The mechanism study indicated that the S^{2-} termination endowed the prepared nanosheet with facet dependent redox active sites. Such excessive active sites could efficiently improve photoinduced electron-hole separation ability and facilitates the balanced extraction of photogenerated charge carrier pairs by decreasing the diffusion distance of the hole along the (001) direction.

1.4.2 Supporting co-catalyst

Currently, photocatalysts for CO_2 reduction usually suffer from lack of active sites, fast charge carrier separation, and limited selectivity. Supporting appropriate co-catalyst on semiconductor photocatalysts is an excellent way to solve the above issues. It is widely accepted that cocatalysts serve four key roles for enhancing photocatalytic reaction as follows: 1) lowering the activation energy of CO_2 reduction; 2) promoting photoinduced electrons and holes migration ability to suppress charge carrier recombination; 3) improving selectivity by enhancing the main rection or suppressing competitive reaction; 4) maintain the catalyst by consuming excess photoinduced charge carrier. [7]

Precious metal cocatalysts could effectively promote the photoinduced electron-hole migration ability and improve the photocatalytic performance. Zhang et al. designed effective Z-scheme photocatalysts g-C_3N_4/$ZnIn_2S_4$ for solar induced carbon dioxide conversion by choosing gold nanoparticles as co-catalyst. [82] The best CN/Au/ZIS sample obtained the carbon monoxide evolution rate of 242.3 μmol h^{-1} g^{-1} and the high selectivity up to 94.1%. The enhanced performance was caused by the Au nanoparticles, which could facilitate charge migration ability and enhance the photogenerated charge carriers separation efficiency. However, though precious metal cocatalyst usually shows excellent photocatalytic activity, the high cost is always a big drawback that limits their industrialization. Recently, developing low-cost and effective cocatalysts has become a hot research area. Ren et al. reported a well dispersed Co on black phosphorus nanoflakes (BP-Co) as a co-catalyst using in photoreduction of carbon dioxide under irradiation of the solar light (>420 nm). [83] The carbon monoxide production rate was as high as 88.6 μmol h^{-1} under optimal sample. The authors believed that the excellent CO_2 reduction ability can be attributed to the interaction between Co and P, which show a high electron concentration property for effective photocatalytic reduction. They believed that the high electron concentration of BP-Co cocatalyst might generate extended electron density for enhancing photo excited electrons to reduction reactions. Another representative work reported by Jiang et al. [84] demonstrated a spinel-type $CuCo_2O_4$ nanoplate as a cocatalyst by the solvothermal way as well as appropriate air calcination treatment. They loaded it on CdS and found that 1.0 wt% $CuCo_2O_4$ loading on CdS showed the best photoreduction of carbon dioxide performance with a carbon monoxide production rate as high as 40 μmol h^{-1} with a TON of 142. The mechanism study revealed that there were mesoporesrich in the prepared $CuCo_2O_4$, and the mesopores $CuCo_2O_4$ in could promote the generation of active sites on surface and facilitate the charge carrier separation ability to improve the photocatalytic carbon dioxide reduction performance.

1.4.3 Heterojunction

By forming semiconductor/semiconductor heterostructures, narrow band gap semiconductors can be used to sensitize wide band gap semiconductors. In a common sensitization mechanism, photogenerated electrons are transferred from the CB of semiconductors with small band gaps to the CB of semiconductors with large band gaps. At same time, the photoinduced holes remain in the VB position of the narrow bandgap semiconductors, which realizes the spatial separation of photogenerated charge carriers, reduces the probability of charge carrier recombination, and enhances the lifetime of photogenerated electrons. Among them, TiO_2 has been widely studied as a classic case for ternary metal sulfide heterojunction. $ZnIn_2S_4/TiO_2$ Z-scheme junctions were constructed because of the suitable band structure of $ZnIn_2S_4$ and TiO_2 to facilitate charge separation by Yang et al. [85] The best hierarchical $ZnIn_2S_4/TiO_2$ junction showed the highest photocatalytic CO_2 reduction activity with a 39-times enhancement in CH_4 evolution rate up to 1.135 µmol g^{-1} h^{-1} which is much higher than the pure $ZnIn_2Sn_4$ without co-catalyst and sacrificial reagent. Huang et al. [86] constructed $CdIn_2S_4/Co_3O_4$ heterojunction by a single-point solvothermal way, endowing the effective charge carrier separation along the interface of $CdIn_2S_4$ and Co_3O_4. The shorter emission lifetime and diminished PL peak compared to pure $CdIn_2S_4$ suggest that carrier separation and diffusion are accelerated, and the opportunity for photogenerated charge recombination is effectively reduced in $CdIn_2S_4/Co_3O_4$. As a result, the CO yield of the $CdIn_2S_4/Co_3O_4$ photocatalytic system increased to 26 µmol h^{-1}.

1.4.4 Energy band engineering

Generally, the band structure could be optimized by introducing structural defects or chemical impurities into the crystal lattice of the semiconductor. It can not only adjust its conductivity, such as electron concentration, carrier mobility, and lifetime, but also reduce its forbidden band to absorb more photons, which could be regarded as one of the most efficient strategies in photocatalyst modulation.

1.4.4.1 Doping

In most cases, the appropriate amount of impurities doping will result in the formation of localized or delocalized electronic states. It not only enhances the absorption of photons but also improves the migration efficiency of charge carriers. In addition, various impurities are confined in a small nanocrystal, which can increase the disorder effect, thereby changing its electronic structure due to the quantum confinement effect. During the past few decades, metal cation doping, non-metallic anion doping, and non-metal molecular doping have been widely investigated in photocatalytic CO_2 reduction.

The light doping with metal ions (with low doping content) can introduce local electronic states, such as forming a donor level on the valence band or forming an acceptor energy under the CB of the wide band gap photocatalyst, narrowering their band gap and enhancing the photocatalytic performance. Generally, La^{3+}, Rh^{5+}, Cr, Zn^{2+}, Sb^{5+}, $Nb^{5+,}$ and Ta^{5+} cations can be used to form accept energy levels in the CB. The donor energy levels in the VB can be formed by impurities Pb^{2+}, Bi^{2+}, Sn^{2+}, Ag^{+}, and Ni^{2+} cations. On the other hand, the heavy doping (with a relatively high dopant content) can form an intermediate energy level by introducing a delocalized electronic state in the middle of the band gap to achieve wide band gap multiphoton excitation. Metal ion impregnation is also effective for narrow band gap photocatalysts that respond to visible light. Metal ion impregnation can improve its electronic structure, such as carrier mobility and conductivity, and promote carrier transport and separation, thereby greatly improving photocatalytic activity.

Pang and co-workers [87] reported a nickel doped zinc sulfide for efficient photocatalytic carbon dioxide reduction. The mechanistic investigation indicated that the doped nickel could enhance light absorption ability and the introduced abundant S vacancies to ZnS. As a result, the optimized sample (0.1% doping amount) achieved outstanding selectivity with HCOOH evolution rate, and excellent QE of 59.1% at 340 nm and 5.6 % at 420 nm. The authors also researched the influence of doping amount on the photocatalytic performance of ZnS and pointed out that the excessive doping amount would instead result in a reduction of S vacancies leading to a diminishing of photocatalytic CO_2 activity. As representative of heavy doping work, Sabban et al. [88]used a simple hydrothermal method to fabricate carbon-doped (20.78 atomic % amount) SnS_2 (SnS_2-C) nanostructured photocatalysts. The photochemical quantum efficiency of SnS_2-C was extremely higher (≈0.72%) compared to pristine SnS_2

(≈0.0028%), with a CH_3CHO production rate of ≈13.98 μmol/100 mg cat^{-h}, almost 250 times higher compared to pristine SnS_2 (≈0.055 μmol/100 mg cat^{-h}). The obviously enhanced performance of SnS_2-C was attributed to the lower conduction band edges under influenced by the micro strains and the more effective adsorption ability of CO_2 by carbon doped.

1.4.4.2 Elemental ratio modification

The elemental ratio modification is an effective energy band engineering strategy that can improve the photocatalytic performance of semiconductor materials. It could make full use of the advantages of different elements and realize the continuity of the band structure by controlling and changing the elemental ratio of multi-component semiconductor materials. Adjust the elemental ratio to achieve the best balance between visible light absorption and redox potential, thereby effectively improving photocatalytic activity. So far, people have researched and explored a variety of molar ratio dependent semiconductors that can be used for photocatalytic carbon dioxide reduction. Wang and co-workers [89]reported Cu_3SnS_4 with multi ratios of Cu (I/II) and Sn (II/IV) for the highly selective and effective photocatalytic reduction of carbon dioxide. They used first-principle calculation to reveal that the CB edge of Cu_3SnS_4 was composed by Sn(II) 5p orbital, which can be easily tuned by adjusting the Sn(II) content. The optimal sample achieved reactivity up to 22.65 μmol g^{-1}h^{-1} for CH_4 and selectivity as high as 83.10 % for CH_4.

1.4.5 Size modulation

It is widely accepted that the size of the photocatalyst highly influences photocatalytic efficiency by affecting the reactants adsorption, the photoinduced charge carriers generation as well as separation, and the surface reduction or oxidation reactions.[90] Generally speaking, reducing the scale of photocatalysts could not only increase the surface area to expose enough active sites and adsorb more reactants but also reduce the distance of excited electrons transferring to the catalyst surface to inhibit the photogenerated electron-hole recombination. Currently, researchers have developed numerous micro-scale photocatalysts, such as nanoclusters, nanowires, nanosheets, and so on.

Among different micro-scale materials, semiconductor quantum dots (QDs) show unique photoluminescence properties and receive much attention from the photocatalysis area. QDs are a class of materials whose radii are smaller than the exciton Bohr radius in three dimensions, appearing unique properties different from both bulk semi-conductors and single-atoms or separated molecules. QDs exhibit unique properties in light absorption and exciton generation because of quantum confinement effects. For instance, the redox potentials of the photoinduced charge carriers could be easily modulated by size controlling. Moreover, the abundance of exposed active sites enhances probability of reactant absorbed on QDs , thus enhancing the interfacial charge transfer ability for photocatalysis. Nowadays. QDs have been widely investigated in photocatalysis, especially photocatalytic CO_2 reduction.

Currently, QDs are usually used as light absorbers and combined with other cocatalysts to perform photocatalytic CO_2 reduction. (Figure 1.10a) As a typical work, Bi et al. reported a positively charged dinuclear cobalt complexes (Co_2L) as cocatalyst coupling with water-soluble CdS QDs with the negative charge for efficient photocatalytic CO_2 reduction. [91] The result indicated that negatively charged CdS QDs showed excellent photocatalytic performance on carbon dioxide to carbon monoxide with a turnover number or TON as high as 1380 with the assistance of the Co cocatalyst. (Figure 1.10b) The authors attributed the excellent performance to the optimized charge carrier transfer between quantum dots photocatalysts and co-catalysts in the assemble electrostatic interaction. However, because there is a noncovalent interaction between the QDs and cocatalysts, cocatalysts usually tend to fall off the surface of the QD, resulting in a decrease in catalytic activity. Constructing strong interaction between the cocatalyst and QDs surface is a good strategy to solve this problem. Wang et al. developed nickel doped cadmium sulfide quantum dots (Ni:CdS) as effective photocatalysts for CO_2 reduction by simply adding Ni^{2+} into the precursor the during the synthesis process. [92] The enhanced photocatalytic CO_2 activity achieved on optimal sample showed 3.9 and 4.9 times higher than pristine cadmium sulfide quantum dots with Ni^{2+} cation and Ni-contained ligand. Moreover, the selectivity of carbon dioxide reduction to carbon-contained products in the Ni:CdS QDs-based photosystem is close to 100%. The mechanism investigation indicated that the doped metal sites not only trapped photoexcited electrons at surface catalytic sites but also suppressed the H_2 generation reaction. These two features carried out by doped Ni^{2+} synergistically enhanced the photocatalytic CO_2 reduction reaction. (Figure 1.10c).

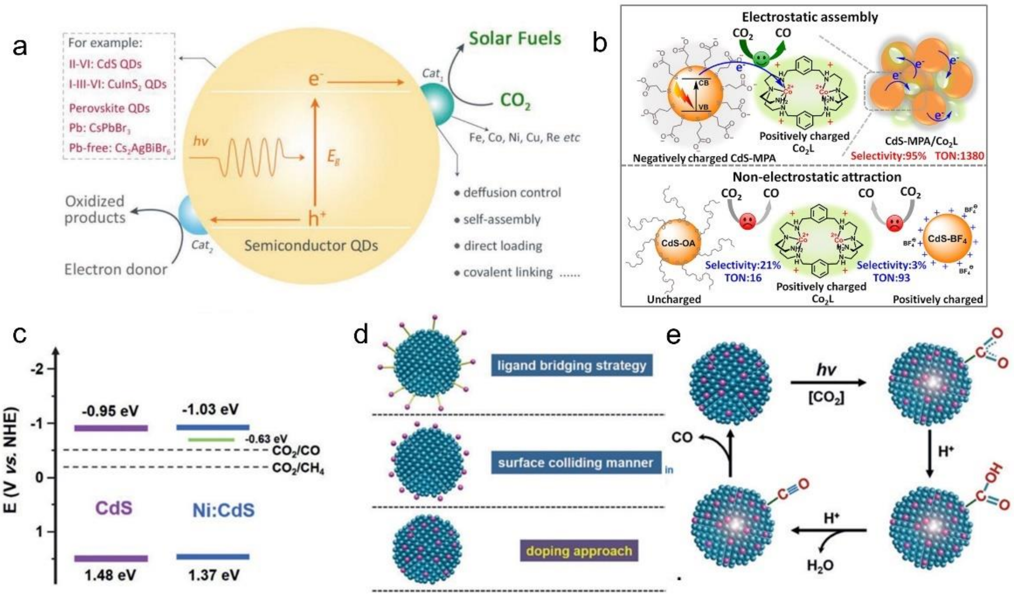

Figure 1.10 (a) Scheme of a typical photocatalytic system using QDs as light absorbers for CO_2 reduction. [93] (b) Illustration of cadmium sulfide nanocrystal with linked different functional group and mechanism of their photoconversion of carbon dioxide. [91] (c) Band structure diagrams for cadmium sulfide quantum dots and nickel doped cadmium sulfide quantum dots as well as the carbon dioxide reduction potentials at pH=7. (d) Schematic illustration of the three different configurations obtained by combining QDs with metal cations. (e) Proposed mechanism of the photocatalytic carbon dioxide reduction over nickel doped cadmium sulfide quantum dots. [92]

1.5 Thesis motivations and organization

Using green and renewable solar energy as an energy source, semiconductor-based photocatalysts to convert carbon dioxide to carbon monoxide or other valuable carbon-contained fuels is regarded a hopeful approach to reach the carbon balance and solve the energy crisis. Compared to other widely investigated photocatalysts, such as metal oxides, carbon-based materials, and so on, metal sulfide photocatalysts have numerous advantages, including narrow band gaps, suitable band edges, and abundant active sites.

However, metal sulfides still suffer from several drawbacks, which limit their further application. The optimization of photocatalysts can be approached from three aspects of the photocatalytic reaction process: 1) photoabsorption, 2) charge separation and transportation to surface, and 3) surface catalytic reduction and oxidation. The detailed approaches include broadening the visible absorption range by reducing the band gap, reducing the electron-hole recombination rate by modulating electronic structures, increasing the surface reaction rate by constructing active sites.

In order to solve these problems, this thesis mainly focuses on modifying metal sulfides towards highly efficient and sustainable CO_2 reduction. To achieve this target, two strategies, defect engineering and energy band engineering, have been considered to improve their photocatalytic performance. First, a series of Cd-In-S solid solution photocatalysts with multi Cd to In ratios are designed, and the enhanced charge carrier separation ability is achieved. Then, the Cd-free non-stoichiometric Ag-In-S quantum dots are designed and investigated as novel photocatalysts for CO_2 reduction. Finally, the Cd vacancies are constructed on CdS_xSe_{1-x} quantum dots, and both reaction efficiency and light absorption ability are enhanced. This dissertation is divided into 5 chapters. A summary of the remaining 4 chapters is described below:

Chapter 2 Selective conversion of CO_2 to CO under visible light by modulating Cd to In ratio: A case study of Cd-In-S colloidal catalysts

Ternary metal sulfides $CdIn_2S_4$ is considered promising candidates for photocatalytic carbon dioxide reduction because of its low cost, high stability, and tunable band structure. Previous works have mainly investigated $CdIn_2S_4$-based heterojunction for photocatalytic CO_2 reduction, while there is less work focused on $CdIn_2S_4$ itself, which limits the mechanism study over $CdIn_2S_4$. Moreover, elemental ratio modification as a fundamental method can be considered to unravel the innate influence between elemental ratio and photocatalytic carbon dioxide reduction performance. In this chapter, the Cd-In-S (CIS) colloidal nanocrystals with different Cd to In ratio were constructed as efficient visible light-responsive photocatalysts for the conversion of CO_2 to CO. It is expected that the different Cd to In ratios can result in different electronic structures influencing the photocatalytic performance. By combining with the DFT calculation, the relationship between the photocatalytic performance and elemental ratio can be unraveled.

Chapter 3 Nanoscale Ag-In-S quantum dots towards efficient photocatalytic CO_2 reduction with Ag/In molar ratio dependent activity and selectivity

Recent research has indicated that the size of photocatalysts usually influences photocatalytic carbon dioxide reduction performance. By controlling the size of the photocatalyst, both specific surface area as well as photoinduced carriers migration distance can be efficiently modified to optimize the photocatalytic carbon dioxide reduction performance. Semiconductor quantum dots (QDs) are a class of materials whose radii are less than the Bohr radius and show unique photoluminescence properties. The construction of ultra-small QDs has become a promising strategy for efficient photocatalytic CO_2 reduction. However, the elements Cd and Pb, which are mostly used in quantum dots, are toxic. It’s necessary to construct Cd or Pb free quantum dots as effective photocatalyst for carbon dioxide reduction. In this chapter, Non-stoichiometric Ag-In-S quantum dots (QDs) have been developed as a promising photocatalyst for the efficient and durable visible-light-driven reduction of CO_2 to syngas under mild condition. It is expected that the novel QDs with suitable elemental ratios could show excellent performance in photocatalytic CO_2 reduction. In addition, the origin of the enhanced performance can be revealed by both experimental and theoretical investigation.

Chapter 4 Construction of surface vacancies on colloid CdS_xSe_{1-x} quantum dots for efficient photocatalytic CO_2 reduction

To achieve highly efficient photocatalytic carbon dioxide reduction under mild reaction condition, the construction of more surface-active sites is widely regarded as a common method to modify the photocatalyst. For instance, the construction of vacancies on the surface of the catalyst can usually influence the optical properties and charge carrier separation ability. Moreover, many works have reported that surface vacancies can act as active sites for photocatalytic reactions. In this chapter, a simple acid etching method is carried out to construct the surface vacancies on colloidal CdS_xSe_{1-x} quantum dots. It is expected that the surface vacancies can be successfully generated by this method, and the generation of the surface vacancies could improve the photocatalytic carbon dioxide reduction performance. Moreover, I expect to reveal the in-depth mechanism that surface vacancies can enhance photocatalytic CO_2 reduction performance.

Chapter 5 General conclusions and future prospects

This chapter concludes with a summary of the main findings and presents an overall conclusion. Furthermore, potential areas for future research are identified. This thesis presents a systematic study on the elemental ratio modification of metal sulfides and their surface defect construction for efficient photocatalytic carbon dioxide reduction. By adjusting the proportion of metal elements in the ternary metal sulfide, the electronic structure of the catalyst can be effectively tuned, which is an efficient way to optimize photocatalytic performance. The construction of more reactive sites on the catalyst surface by surface etching can directly affect surface catalysis. The findings in this thesis deepen the understanding of metal sulfide photocatalysts for CO_2 reduction.

Reference

[1] H. Lin, S. Luo, H. Zhang, J. Ye, Toward solar-driven carbon recycling, Joule, 6 (2022) 294-314.

[2] K. Maeda, Metal-Complex/Semiconductor Hybrid Photocatalysts and Photoelectrodes for CO2 Reduction Driven by Visible Light, Adv Mater, 31 (2019) e1808205.

[3] W. Tu, Y. Zhou, Z. Zou, Photocatalytic conversion of CO2 into renewable hydrocarbon fuels: state-of-the-art accomplishment, challenges, and prospects, Adv Mater, 26 (2014) 4607-4626.

[4] H. Tong, S. Ouyang, Y. Bi, N. Umezawa, M. Oshikiri, J. Ye, Nano-photocatalytic materials: possibilities and challenges, Adv Mater, 24 (2012) 229-251.

[5] S. Patial, R. Kumar, P. Raizada, P. Singh, Q. Van Le, E. Lichtfouse, D. Le Tri Nguyen, V.H. Nguyen, Boosting light-driven CO2 reduction into solar fuels: Mainstream avenues for engineering ZnO-based photocatalysts, Environ Res, 197 (2021) 111134.

[6] T. Torimoto, T. Kameyama, S. Kuwabata, Photofunctional Materials Fabricated with Chalcopyrite-Type Semiconductor Nanoparticles Composed of AgInS2 and Its Solid Solutions, J Phys Chem Lett, 5 (2014) 336-347.

[7] J. Ran, M. Jaroniec, S.Z. Qiao, Cocatalysts in Semiconductor-based Photocatalytic CO2 Reduction: Achievements, Challenges, and Opportunities, Adv Mater, 30 (2018).

[8] M. Aresta, A. Dibenedetto, Utilisation of CO2 as a chemical feedstock: opportunities and challenges, Dalton Trans, (2007) 2975-2992.

[9] S. Saeidi, N.A.S. Amin, M.R. Rahimpour, Hydrogenation of CO2 to value-added products—A review and potential future developments, Journal of CO2 Utilization, 5 (2014) 66-81.

[10] X. Chang, T. Wang, J. Gong, CO2 photo-reduction: insights into CO2 activation and reaction on surfaces of photocatalysts, Energy Environ. Sci., 9 (2016) 2177-2196.

[11] L. Liu, S. Wang, H. Huang, Y. Zhang, T. Ma, Surface sites engineering on semiconductors to boost photocatalytic CO2 reduction, Nano Energy, 75 (2020).

[12] C.D. Windle, R.N. Perutz, Advances in molecular photocatalytic and electrocatalytic CO2 reduction, Coordination Chemistry Reviews, 256 (2012) 2562-2570.

[13] Z. Sun, H. Wang, Z. Wu, L. Wang, g-C3N4 based composite photocatalysts for photocatalytic CO2 reduction, Catal. Today, 300 (2018) 160-172.

[14] M. Anpo, H. Yamashita, Y. Ichihashi, S. Ehara, Photocatalytic reduction of CO2 with H2O on various titanium oxide catalysts, J. Electroanal. Chem., 396 (1995) 21-26.

[15] A.J. MORRIS, G.J. MEYER, E. FUJITA, Molecular Approaches to the Photocatalytic Reduction of Carbon Dioxide for Solar Fuels, Acc. Chem. Res., 42 (2009) 1983-1994.

[16] S. Xie, Q. Zhang, G. Liu, Y. Wang, Photocatalytic and photoelectrocatalytic reduction of CO2 using heterogeneous catalysts with controlled nanostructures, Chem Commun (Camb), 52 (2016) 35-59.

[17] M. Madi, M. Tahir, S. Tasleem, Advances in structural modification of perovskite semiconductors for visible light assisted photocatalytic CO2 reduction to renewable solar fuels: A review, Journal of Environmental Chemical Engineering, 9 (2021).

[18] X. Jiao, K. Zheng, Z. Hu, Y. Sun, Y. Xie, Broad-Spectral-Response Photocatalysts for CO2 Reduction, ACS Cent Sci, 6 (2020) 653-660.

[19] Y.Z. Cheng, X. Ding, B.H. Han, Porous Organic Polymers for Photocatalytic Carbon Dioxide Reduction, ChemPhotoChem, 5 (2021) 406-417.

[20] H.H. Mohamed, D.W. Bahnemann, The role of electron transfer in photocatalysis: Fact and fictions, Appl. Catal., B Environ, 128 (2012) 91-104.

[21] S.N. Habisreutinger, L. Schmidt-Mende, J.K. Stolarczyk, Photocatalytic reduction of CO2 on TiO2 and other semiconductors, Angew Chem Int Ed Engl, 52 (2013) 7372-7408.

[22] P. Liu, X. Peng, Y.-L. Men, Y.-X. Pan, Recent progresses on improving CO2 adsorption and proton production for enhancing efficiency of photocatalytic CO2 reduction by H2O, Green Chemical Engineering, 1 (2020) 33-39.

[23] W. Zhang, A.R. Mohamed, W.J. Ong, Z-Scheme Photocatalytic Systems for Carbon Dioxide Reduction: Where Are We Now?, Angew Chem Int Ed Engl, 59 (2020) 22894-22915.

[24] M. Marszewski, S. Cao, J. Yu, M. Jaroniec, Semiconductor-based photocatalytic CO2 conversion, Materials Horizons, 2 (2015) 261-278.

[25] X. Liu, S. Inagaki, J. Gong, Heterogeneous Molecular Systems for Photocatalytic CO2 Reduction with Water Oxidation, Angew Chem Int Ed Engl, 55 (2016) 14924-14950.

[26] A. FUJISHIMA, K. HONDA, Electrochemical Photolysis of Water at a Semiconductor Electrode, Nature, 238 (1972) 37–38.

[27] X. Meng, S. Ouyang, T. Kako, P. Li, Q. Yu, T. Wang, J. Ye, Photocatalytic CO2 conversion over alkali modified TiO2 without loading noble metal cocatalyst, Chem Commun (Camb), 50 (2014) 11517-11519.

[28] Y. Liu, S. Zhou, J. Li, Y. Wang, G. Jiang, Z. Zhao, B. Liu, X. Gong, A. Duan, J. Liu, Y. Wei, L. Zhang, Photocatalytic reduction of CO 2 with water vapor on surface La-modified TiO 2 nanoparticles with enhanced CH 4 selectivity, Appl. Catal., B Environ, 168-169 (2015) 125-131.

[29] J.A. Oliveira, A.E. Nogueira, M.C.P. Gonçalves, E.C. Paris, C. Ribeiro, G.Y. Poirier, T.R. Giraldi, Photoactivity of N-doped ZnO nanoparticles in oxidative and reductive reactions, Applied Surface Science, 433 (2018) 879-886.

[30] X. Wang, K. Maeda, A. Thomas, K. Takanabe, G. Xin, J.M. Carlsson, K. Domen, M. Antonietti, A metal-free polymeric photocatalyst for hydrogen production from water under visible light, Nat Mater, 8 (2009) 76-80.

[31] J.-y. Tang, W.-g. Zhou, R.-t. Guo, C.-y. Huang, W.-g. Pan, Enhancement of photocatalytic performance in CO2 reduction over Mg/g-C3N4 catalysts under visible light irradiation, Catal. Commun., 107 (2018) 92-95.

[32] W. Tu, Y. Xu, J. Wang, B. Zhang, T. Zhou, S. Yin, S. Wu, C. Li, Y. Huang, Y. Zhou, Z. Zou, J. Robertson, M. Kraft, R. Xu, Investigating the Role of Tunable Nitrogen Vacancies in Graphitic Carbon Nitride Nanosheets for Efficient Visible-Light-Driven H2 Evolution and CO2 Reduction, ACS Sustainable Chem. Eng., 5 (2017) 7260-7268.

[33] N. Sun, Y. Zhu, M. Li, J. Zhang, J. Qin, Y. Li, C. Wang, Thermal coupled photocatalysis over Pt/g-C3N4 for selectively reducing CO2 to CH4 via cooperation of

the electronic metal–support interaction effect and the oxidation state of Pt, Appl. Catal., B Environ, 298 (2021).

[34] X. Feng, Y. Pi, Y. Song, C. Brzezinski, Z. Xu, Z. Li, W. Lin, Metal–Organic Frameworks Significantly Enhance Photocatalytic Hydrogen Evolution and CO2 Reduction with Earth-Abundant Copper Photosensitizers, Journal of the American Chemical Society, 142 (2020) 690-695.

[35] H. Zhang, J. Wei, J. Dong, G. Liu, L. Shi, P. An, G. Zhao, J. Kong, X. Wang, X. Meng, J. Zhang, J. Ye, Efficient Visible-Light-Driven Carbon Dioxide Reduction by a Single-Atom Implanted Metal-Organic Framework, Angew Chem Int Ed Engl, 55 (2016) 14310-14314.

[36] D. Li, M. Kassymova, X. Cai, S.-Q. Zang, H.-L. Jiang, Photocatalytic CO2 reduction over metal-organic framework-based materials, Coordination Chemistry Reviews, 412 (2020).

[37] J. Wang, S. Lin, N. Tian, T. Ma, Y. Zhang, H. Huang, Nanostructured Metal Sulfides: Classification, Modification Strategy, and Solar-Driven CO 2 Reduction Application, Advanced Functional Materials, 31 (2020).

[38] P. Zhang, S. Wang, B.Y. Guan, X.W. Lou, Fabrication of CdS hierarchical multi-cavity hollow particles for efficient visible light CO2 reduction, Energy Environ. Sci., 12 (2019) 164-168.

[39] J. Low, B. Dai, T. Tong, C. Jiang, J. Yu, In Situ Irradiated X-Ray Photoelectron Spectroscopy Investigation on a Direct Z-Scheme TiO2 /CdS Composite Film Photocatalyst, Adv Mater, 31 (2019) e1802981.

[40] X. Meng, Q. Yu, G. Liu, L. Shi, G. Zhao, H. Liu, P. Li, K. Chang, T. Kako, J. Ye, Efficient photocatalytic CO 2 reduction in all-inorganic aqueous environment: Cooperation between reaction medium and Cd(II) modified colloidal ZnS, Nano Energy, 34 (2017) 524-532.

[41] H. Pang, X. Meng, P. Li, K. Chang, W. Zhou, X. Wang, X. Zhang, W. Jevasuwan, N. Fukata, D. Wang, J. Ye, Cation Vacancy-Initiated CO2 Photoreduction over ZnS for Efficient Formate Production, ACS Energy Let., 4 (2019) 1387-1393.

[42] E.A. Kozlova, M.N. Lyulyukin, D.V. Markovskaya, D.S. Selishchev, S.V. Cherepanova, D.V. Kozlov, Synthesis of Cd1-xZnxS photocatalysts for gas-phase CO2 reduction under visible light, Photochem Photobiol Sci, 18 (2019) 871-877.

[43] X. Jiao, Z. Chen, X. Li, Y. Sun, S. Gao, W. Yan, C. Wang, Q. Zhang, Y. Lin, Y. Luo, Y. Xie, Defect-Mediated Electron-Hole Separation in One-Unit-Cell ZnIn2S4 Layers for Boosted Solar-Driven CO2 Reduction, J Am Chem Soc, 139 (2017) 7586-7594.

[44] Y. Wu, H. Wang, W. Tu, S. Wu, J.W. Chew, Effects of composition faults in ternary metal chalcogenides (Zn In2S3+, x = 1–5) layered crystals for visible-light-driven catalytic hydrogen generation and carbon dioxide reduction, Appl. Catal., B Environ, 256 (2019).

[45] S. Wang, B.Y. Guan, Y. Lu, X.W.D. Lou, Formation of Hierarchical In2S3-CdIn2S4 Heterostructured Nanotubes for Efficient and Stable Visible Light CO2 Reduction, J Am Chem Soc, 139 (2017) 17305-17308.

[46] G. Zhang, Z. Wang, T. He, J. Wu, J. Zhang, J. Wu, Rationally design and in-situ fabrication of ultrasmall pomegranate-like CdIn2S4/ZnIn2S4 Z-scheme heterojunction with abundant vacancies for improving CO2 reduction and water splitting, Chemical Engineering Journal, 442 (2022).

[47] F. Xu, J. Zhang, B. Zhu, J. Yu, J. Xu, CuInS2 sensitized TiO2 hybrid nanofibers for improved photocatalytic CO2 reduction, Appl. Catal., B Environ, 230 (2018) 194-202.

[48] K. Kim, A. Razzaq, S. Sorcar, Y. Park, C.A. Grimes, S.-I. In, Hybrid mesoporous Cu2ZnSnS4 (CZTS)–TiO2 photocatalyst for efficient photocatalytic conversion of CO2 into CH4 under solar irradiation, RSC Advances, 6 (2016) 38964-38971.

[49] A. Raza, H. Shen, A.A. Haidry, L. Sun, R. Liu, S. Cui, Studies of Z-scheme WO3-TiO2/Cu2ZnSnS4 ternary nanocomposite with enhanced CO2 photoreduction under visible light irradiation, Journal of CO2 Utilization, 37 (2020) 260-271.

[50] S. HARRIS, R.R.CHIANELL, Catalysis by Transition Metal Sulfides: A Theoretical and Experimental Study of the Relation between the Synergic Systems and the Binary Transition Metal Sulfides, J. Catal., 98 (1986) 17-31.

[51] D.G. Moon, S. Rehan, D.H. Yeon, S.M. Lee, S.J. Park, S. Ahn, Y.S. Cho, A review on binary metal sulfide heterojunction solar cells, Sol. Energy Mater. Sol. Cells, 200 (2019).

[52] K. Zhang, L. Guo, Metal sulphide semiconductors for photocatalytic hydrogen production, Catalysis Science & Technology, 3 (2013).

[53] Q. Li, X. Li, S. Wageh, A.A. Al-Ghamdi, J. Yu, CdS/Graphene Nanocomposite Photocatalysts, Advanced Energy Materials, 5 (2015).

[54] L. Cheng, Q. Xiang, Y. Liao, H. Zhang, CdS-Based photocatalysts, Energy Environ. Sci., 11 (2018) 1362-1391.

[55] Y. Meng, G. Liu, G. Zuo, X. Meng, T. Wang, J. Ye, A review on ZnS-based photocatalysts for CO2 reduction in all-inorganic aqueous medium, Nanoscale, 14 (2022) 14455-14465.

[56] Z. Ye, L. Kong, F. Chen, Z. Chen, Y. Lin, C. Liu, A comparative study of photocatalytic activity of ZnS photocatalyst for degradation of various dyes, Optik, 164 (2018) 345-354.

[57] G.-J. Lee, J.J. Wu, Recent developments in ZnS photocatalysts from synthesis to photocatalytic applications — A review, Powder Technol., 318 (2017) 8-22.

[58] C.-Y. Yeh, Z.W. Lu, S. Froyen, A. Zunger, Zinc-blende–wurtzite polytypism in semiconductors, Physical Review B, 46 (1992) 10086-10097.

[59] H.H. Hiroaki Fujiwara, Kei Murakoshi, Yuji Wada, and Shozo Yanagida*, Surface Characteristics of ZnS Nanocrystallites Relating to Their Photocatalysis for CO2 Reduction, Langmuir, 14 (1998) 5154-5159.

[60] G. Fu, J.-M. Lee, Ternary metal sulfides for electrocatalytic energy conversion, J. Mater. Chem. A, 7 (2019) 9386-9405.

[61] J.C. Sarker, G. Hogarth, Dithiocarbamate Complexes as Single Source Precursors to Nanoscale Binary, Ternary and Quaternary Metal Sulfides, Chem. Rev., 121 (2021) 6057-6123.

[62] S.S. Brown, A.J. Rondinone, M.D. Pawel, S. Dai, Ternary cadmium sulphide selenide quantum dots as new scintillation materials, Materials Technology, 23 (2013) 94-99.

[63] B. Debnath, S. Dhingra, C.M. Nagaraja, Recent Developments in the Design of CdxZn1−xS-Based Photocatalysts for Sustainable Production of Hydrogen, Solar RRL, 5 (2021).

[64] J. Wang, S. Sun, R. Zhou, Y. Li, Z. He, H. Ding, D. Chen, W. Ao, A review: Synthesis, modification and photocatalytic applications of ZnIn2S4, Journal of Materials Science & Technology, 78 (2021) 1-19.

[65] Y. Kumar, R. Kumar, P. Raizada, A.A.P. Khan, Q.V. Le, P. Singh, V.-H. Nguyen, Novel Z-Scheme ZnIn2S4-based photocatalysts for solar-driven environmental and energy applications: Progress and perspectives, Journal of Materials Science & Technology, 87 (2021) 234-257.

[66] R. Yang, L. Mei, Y. Fan, Q. Zhang, R. Zhu, R. Amal, Z. Yin, Z. Zeng, ZnIn2 S4 - Based Photocatalysts for Energy and Environmental Applications, Small Methods, 5 (2021) e2100887.

[67] S. Shen, P. Guo, L. Zhao, Y. Du, L. Guo, Insights into photoluminescence property and photocatalytic activity of cubic and rhombohedral ZnIn2S4, J. Solid State Chem., 184 (2011) 2250-2256.

[68] S. Peng, S.G. Mhaisalkar, S. Ramakrishna, Solution synthesis of CdIn2S4 nanocrystals and their photoelectrical application, Mater. Lett., 79 (2012) 216-218.

[69] M. Dan, A. Prakash, Q. Cai, J. Xiang, Y. Ye, Y. Li, S. Yu, Y. Lin, Y. Zhou, Energy-Band-Controlling Strategy to Construct Novel CdxIn1-xS Solid Solution for Durable Visible Light Photocatalytic Hydrogen Sulfide Splitting, Solar RRL, 3 (2019).

[70] Y.J. Zhang, H.M. Tang, S.-P. Gao, Density Functional Theory Study of ZnIn2S4 and CdIn2S4 Polymorphs Using Full-Potential Linearized Augmented Plane Wave Method and Modified Becke–Johnson Potential, physica status solidi (b), 257 (2019).

[71] Y.-X. Tan, Z.-M. Chai, B.-H. Wang, S. Tian, X.-X. Deng, Z.-J. Bai, L. Chen, S. Shen, J.-K. Guo, M.-Q. Cai, C.-T. Au, S.-F. Yin, Boosted Photocatalytic Oxidation of Toluene into Benzaldehyde on CdIn2S4-CdS: Synergetic Effect of Compact Heterojunction and S-Vacancy, ACS Catalysis, 11 (2021) 2492-2503.

[72] J.P. Sawant, S.F. Shaikh, R.B. Kale, H.M. Pathan, Chemical Bath Deposition of CuInS2 Thin Films and Synthesis of CuInS2 Nanocrystals: A Review, Engineered Science, (2020).

[73] R. Klenk, J. Klaer, R. Scheer, M.C. Lux-Steiner, I. Luck, N. Meyer, U. Rühle, Solar cells based on CuInS2—an overview, Thin Solid Films, 480-481 (2005) 509-514.

[74] J. Kolny-Olesiak, H. Weller, Synthesis and application of colloidal CuInS2 semiconductor nanocrystals, ACS Appl Mater Interfaces, 5 (2013) 12221-12237.

[75] J. Wang, N. Yu, Y. Zhang, Y. Zhu, L. Fu, P. Zhang, L. Gao, Y. Wu, Synthesis and performance of Cu2ZnSnS4 semiconductor as photocathode for solar water splitting, Journal of Alloys and Compounds, 688 (2016) 923-932.

[76] Y. Kong, Y. Li, Y. Zhang, W. Lin, Unveiling the Selectivity of CO2 Reduction on Cu2ZnSnS4: The Effect of Exposed Termination, The Journal of Physical Chemistry C, 125 (2021) 24967-24973.

[77] S. Chen, X.G. Gong, A. Walsh, S.-H. Wei, Defect physics of the kesterite thin-film solar cell absorber Cu2ZnSnS4, Appl. Phys. Lett., 96 (2010).

[78] S. Wang, X. Han, Y. Zhang, N. Tian, T. Ma, H. Huang, Inside-and-Out Semiconductor Engineering for CO2 Photoreduction: From Recent Advances to New Trends, Small Structures, 2 (2020).

[79] S.N. Talapaneni, G. Singh, I.Y. Kim, K. AlBahily, A.H. Al-Muhtaseb, A.S. Karakoti, E. Tavakkoli, A. Vinu, Nanostructured Carbon Nitrides for CO2 Capture and Conversion, Adv Mater, 32 (2020) e1904635.

[80] S. Wang, B.Y. Guan, X.W.D. Lou, Construction of ZnIn2S4-In2O3 Hierarchical Tubular Heterostructures for Efficient CO2 Photoreduction, J Am Chem Soc, 140 (2018) 5037-5040.

[81] N. Wang, S. Cheong, D.E. Yoon, P. Lu, H. Lee, Y.K. Lee, Y.S. Park, D.C. Lee, Efficient, Selective CO2 Photoreduction Enabled by Facet-Resolved Redox-Active Sites on Colloidal CdS Nanosheets, J Am Chem Soc, 144 (2022) 16974-16983.

[82] G. Zhang, X. Zhu, D. Chen, N. Li, Q. Xu, H. Li, J. He, H. Xu, J. Lu, Hierarchical Z-scheme g-C3N4/Au/ZnIn2S4 photocatalyst for highly enhanced visible-light photocatalytic nitric oxide removal and carbon dioxide conversion, Environmental Science: Nano, 7 (2020) 676-687.

[83] X. Ren, L. Shi, Y. Li, S. Song, Q. Wang, S. Luo, L. Ren, H. Zhang, Y. Izumi, X. Peng, D. Philo, F. Ichihara, J. Ye, Single Cobalt Atom Anchored Black Phosphorous Nanosheets as an Effective Cocatalyst Promotes Photocatalysis, ChemCatChem, 12 (2020) 3870-3879.

[84] M. Jiang, Y. Gao, Z. Wang, Z. Ding, Photocatalytic CO 2 reduction promoted by a CuCo 2 O 4 cocatalyst with homogeneous and heterogeneous light harvesters, Appl. Catal., B Environ, 198 (2016) 180-188.

[85] G. Yang, D. Chen, H. Ding, J. Feng, J.Z. Zhang, Y. Zhu, S. Hamid, D.W. Bahnemann, Well-designed 3D ZnIn2S4 nanosheets/TiO2 nanobelts as direct Z-scheme photocatalysts for CO2 photoreduction into renewable hydrocarbon fuel with high efficiency, Appl. Catal., B Environ, 219 (2017) 611-618.

[86] L. Huang, B. Li, B. Su, Z. Xiong, C. Zhang, Y. Hou, Z. Ding, S. Wang, Fabrication of hierarchical Co3O4@CdIn2S4 p–n heterojunction photocatalysts for improved CO2 reduction with visible light, J. Mater. Chem. A, 8 (2020) 7177-7183.

[87] H. Pang, X. Meng, H. Song, W. Zhou, G. Yang, H. Zhang, Y. Izumi, T. Takei, W. Jewasuwan, N. Fukata, J. Ye, Probing the role of nickel dopant in aqueous colloidal ZnS nanocrystals for efficient solar-driven CO2 reduction, Appl. Catal., B Environ, 244 (2019) 1013-1020.

[88] I. Shown, S. Samireddi, Y.-C. Chang, R. Putikam, P.-H. Chang, A. Sabbah, F.-Y. Fu, W.-F. Chen, C.-I. Wu, T.-Y. Yu, P.-W. Chung, M.C. Lin, L.-C. Chen, K.-H. Chen, Carbon-doped SnS2 nanostructure as a high-efficiency solar fuel catalyst under visible light, Nature Communications, 9 (2018).

[89] J. Wang, T. Bo, B. Shao, Y. Zhang, L. Jia, X. Tan, W. Zhou, T. Yu, Effect of S vacancy in Cu3SnS4 on high selectivity and activity of photocatalytic CO2 reduction, Appl. Catal., B Environ, 297 (2021).

[90] Y.-F. Li, Z.-P. Liu, Particle Size, Shape and Activity for Photocatalysis on Titania Anatase Nanoparticles in Aqueous Surroundings, Journal of the American Chemical Society, 133 (2011) 15743-15752.

[91] Q.-Q. Bi, J.-W. Wang, J.-X. Lv, J. Wang, W. Zhang, T.-B. Lu, Selective Photocatalytic CO2 Reduction in Water by Electrostatic Assembly of CdS Nanocrystals with a Dinuclear Cobalt Catalyst, ACS Catalysis, 8 (2018) 11815-11821.

[92] J. Wang, T. Xia, L. Wang, X. Zheng, Z. Qi, C. Gao, J. Zhu, Z. Li, H. Xu, Y. Xiong, Enabling Visible-Light-Driven Selective CO2 Reduction by Doping Quantum Dots: Trapping Electrons and Suppressing H2 Evolution, Angew Chem Int Ed Engl, 57 (2018) 16447-16451.

[93] H.L. Wu, X.B. Li, C.H. Tung, L.Z. Wu, Semiconductor Quantum Dots: An Emerging Candidate for CO2 Photoreduction, Adv Mater, 31 (2019) e1900709.

Chapter 2 Selective conversion of CO_2 to CO under visible light by modulating Cd to In ratio: A case study of Cd-In-S colloidal catalysts

2.1 Introduction

During the past decades, photocatalytic CO_2 reduction has been regarded as a green chemistry and appealing approach for the conversion of CO_2 into value-added chemical feedstocks (such as CO, CH_3OH, and C_{2+} products), sustainable carbonaceous fuel production, and carbon neutrality.[1-10] However, photocatalytic CO_2 reduction in water is an uphill reaction that requires high energy input due to the chemical inertness of CO_2 molecules, resulting in an unsatisfactory solar-to-fuel efficiency for practical application.[11] The design and construction of a photocatalyst that targets a long carrier lifetime, wide light-harvesting region, and abundant catalytic active sites are highly desirable for achieving efficient photocatalytic CO_2 reduction.[12-18]

Benefitting from the suitable electronic structures, metal sulfide-based photocatalysts with excellent light harvesting and charge transfer ability have been widely studied for visible-light-driven CO_2 conversion.[19-22] In order to further improve the catalytic performance, introducing hetero-atoms into conventional metal sulfides to form bimetallic sulfides, such as $ZnIn_2S_4$, $CuInS_2$, $AgInS_2$, has been considered to be effective due to suitable band gap and excellent photostability.[23-30] In addition, engineering the stoichiometric ratio of metal cations within the bimetallic sulfides has been regarded as a feasible and effective method for further enhancing photocatalytic performance.[31-34] Chang et al. reported a nonstoichiometric Cu-In-S as a catalytic photocathode.[27] In their work, the band structures of Cu-In-S nanocrystals could be easily adjusted by tuning the molar ratio of Cu to In, and good photon-harvesting ability as well as electrocatalytic activity can be realized. Very recently, our group reported the construction of non-stoichiometric Ag-In-S quantum dots for photocatalytic CO_2 conversion to CO. Mechanistic investigations indicated that by changing the Ag/In ratio, both the electronic structures and optoelectronic characteristics can be modulated, which synergistically tailoring the photocatalytic performance. Among other bimetallic sulfides, cadmium indium sulfide ($CdIn_2S_4$) has shown great potential for applications in optoelectronic and photocatalytic fields due to its low cost, tunable band gap (2.0-2.4 eV), a good electronic conductivity.[35] Inspired by the previously mentioned works, we expect that changing Cd to In molar ratio in cadmium indium sulfide (Cd-In-S) colloidal system would be an efficient and compelling strategy for further enhancing the catalytic performance.

In this study, we demonstrated a facile and low-cost method to prepare Cd-In-S colloidal nanocrystal (CIS), which enabled a feasible tuning of the Cd to In ratio by simply controlling the amount of Cd precursors. Accordingly, the optimized CIS sample (3-CIS), with the assistance of $Co(bpy)_3^{2+}$ as the cocatalyst, demonstrated an efficient CO production rate of 22.9 μmol h^{-1} and selectivity up to 80%. The mechanistic investigations reveal the critical contributions of Cd to In molar ratio to modulate the electronic structures and charge carrier dynamics of the CIS colloidal system. In particular, the changing of Cd to In ratio could regulate the conduction band positions of CIS, as verified by the DFT calculations, which have a strong relationship to the light absorption ability, photo-induced electrons reduction ability, and charge transfer behavior of the catalyst. This work provides the fundamentals of tuning Cd to In molar ratio in colloidal CIS nanocrystals and an in-depth understanding of manipulating the electronic structure to improve the catalytic activity of bimetallic sulfide-based materials.

2.2 Experimental section

2.2.1 Materials preparation

In a typical synthesis process, a certain amount (0.07 mL, 0.175 mL, 0.35 mL, and 0.525 mL) of 1.0 M $CdCl_2$ aqueous solution and 2 mL of 1.0 M mercaptoacetic acid solution were added to 8 mL of water under magnetic stirring. The resulting suspension became transparent after the addition of 1.0 mL of 5.0 M NH_4OH solution. Then, 0.7 mL of 1.0 M $InCl_3$ aqueous solution, which contains 0.2 M HNO_3 was added to the as-mentioned transparent solution. Meanwhile, 0.4 mL of 1.0 M Na_2S solution was added under continuous stirring, and the resulting solution was kept at 96 °C for 1h in the oil bath. After that, the solution was transferred to other bottles and cooled down to room temperature, followed by adding 50 mL IPA into the solution to form precipitate. Finally, the precipitate was washed several times by IPA and dried in a vacuum oven at 70 °C overnight. The final products were named 1-CIS, 2-CIS, 3-CIS, and 4-CIS, respectively, according to the molar ratios of Cd to In during the fabrication process. Pure CdS and In_2S_3 samples were prepared by the same method without adding $InCl_3$ aqueous solution and $CdCl_2$ aqueous solution, respectively.

2.2.2 Material characterization

The X-ray diffraction (XRD) patterns were recorded by powder XRD on the X-ray diffractometer (X'pert powder, PANalytical B.V.). Transmission electron microscopy (TEM) and high-resolution transmission electron microscopy (HRTEM) images of samples were measured from the TEM machine (JEM-2100F, JEOL). UV-Vis absorption spectra were obtained by Ultraviolet-visible spectroscopy (UV-2600, Shimadzu). The decay time spectra were obtained on the Hamamatsu instrument (C5680, Hamamatsu), and the wavelength of excitation light is 400 nm. The chemical states of the prepared samples were recorded on X-ray photoelectron spectroscopy (XPS, Escalab 250 Xi, Thermo Scientific). The inductively coupled plasma-optical emission spectrometry (ICP-OES) data were obtained on ICP-OES instrument (Agilent5800, Agilent). The Mott-Schottky tests were conducted in the dark at 1000 Hz on an electrochemical station (ALS/CH model 650A) using the CIS samples photoanode as the working electrode in a typical three-electrode cell with 50 ml of 0.5 M Na_2SO_4 solution as electrolyte.

2.2.3 Photoelectrochemical measurement

The photocatalytic CO_2 reduction reaction tests were carried out in a liquid-solid reaction in an about 120 mL quartz reactor under mild conditions. Typically, 20 mg of catalyst,10 mL of water, 25 mL of DMF, 20 mg of 2,2'-Bipyridyl, 1 μmol Co^{2+} dissolved in DMF solution, and 7 mL of TEOA were dispersed in a beaker and was sonicated for 30 minutes to obtain a well-dispersed solution. The well-dispersed reaction solution was transferred to the quartz reactor and connected to a glass-closed reaction system, and then evacuated for 15 minutes. After that, the closed system was filled with approximately 101 kPa of pure CO_2 gas. The visible light irradiation was provided by a 300 W xenon lamp with a UV cut-off filter (L40 filter, $\lambda > 400$ nm), and the cooling water filter was set between the light and the reactor to keep the reaction solution at room temperature. Gas chromatography (GC-8A, Shimadzu) and (GC-14B, Shimadzu) was used to detect and analyze the amounts of H_2 and CO gas products.

The selectivity of CO is calculated based on the following equation:

$$Selectivity\ of\ CO\ (\%) = \frac{amount\ of\ generated\ CO}{amount\ of\ generated\ CO\ and\ H_2} \times 100\%$$

In order to trace the carbon source of products, the isotope labeling experiment was executed under the same reaction conditions as described above, except using $^{13}CO_2$ as reactant. The gas chromatography-mass spectrometry (GC-MS) (JEOL-GCMS, JMS-K9, 6890N Network GC) were used to detect and analyze the product.

The apparent quantum yield (AQY) measurement was conducted by same light source (the 300 W xenon lamp) equipped with monochromatic light band-pass filters (MIF-W, Optical Coatings Japan Co.). The number of incident photons were measured by using the radiant power energy meter (Ushio Spectroradiometer, USR-40). The AQY of CO evolution was calculated by the following equation:

$$\begin{aligned} AQY(\%) &= \frac{number\ of\ reacted\ electrons}{number\ of\ incident\ photons} \times 100\% \\ &= \frac{number\ of\ generated\ CO\ molecules \times 2}{number\ of\ incident\ photons} \times 100\% \end{aligned}$$

2.2.4 Computational details

Density functional theory (DFT) calculations have been performed using the pwscf code of the QUANTUM ESPRESSO package based on the DFT and plane-wave basis set. The Perdew-Burke-Ernzerhof (PBE) functional of generalized gradient approximation (GGA) was used for exchange-correlation potential. The Projector augmented wave (PAW) method has been employed with the energy cutoff of 50 Ry and charge density cutoff of 500 Ry for geometry structure relaxation. Gaussian smearing with a smearing width of 0.005 Ry was used to speed up the convergence. The DFT-D method of Grimme as a necessary tool is employed for van der Waals (vdW) dispersion correction. The *k*-point sampling of the Brillouin zone was constructed using Monkhorst and Pack mesh scheme. For different models, we used different k-point sampling as follows: 3×3×3 k-point for bulk model relaxation and 5×5×5 k-point for bulk model electronic structure; 3×3×1 for surface absorption relaxation. The convergence limit of energy for the computation is set to 10^{-6} Ry. The models we used for calculations are all based on stoichiometry. The $CdIn_5S_8$ and $Cd_2In_4S_8$ with In_2S_3 crystal structures were used to represent 1-CIS and 2-CIS, while the model $Cd_6In_2S_8$ and Cd_7InS_8 with CdS structure were used to represent 3-CIS and 4-CIS.

2.3 Results and discussion

The fabrication procedure of Cd-In-S (CIS) colloids that is using facile colloidal synthesis method was illustrated in Figure 2.1. The formation mechanism of CIS included the self-decomposition with the ion exchange process. When mercaptoacetic acid solution was added to the $CdCl_2$ solution, ion exchange led to the formation of Cd-mercaptoacetate intermediate. During oil bath treatment, both Cd-mercaptoacetate and the residual $InCl_3$ decomposed to release Cd^{2+}, In^{3+}, and S^{2-}, generating Cd-In-S phases to form CIS samples. The samples were named 1-CIS to 4-CIS, with the order of increasing Cd precursor contents in the synthesis process. Figure 2.3a showed XRD patterns of the as-synthesized CIS. For comparison, pristine In_2S_3 and CdS samples were also synthesized, and their characteristic peaks were in agreement with those of β-In_2S_3 (ICSD No.202353) and cubic CdS (ICSD No.81925), respectively. The characteristic peaks of CIS gradually shifted to lower diffraction angle with the increasing Cd contents, which could be attributed to the larger ionic radius of Cd^{2+} (0.95 Å) than that of In^{3+} (0.80 Å).[18,] [36] No diffraction peaks related to other phase was observed, indicating the formation of CIS solid solution. Further adding excessive amount of Cd during the fabrication process with a Cd/In molar ratio 0.84/0.13 (5-CIS) and 0.88/0.09 (6-CIS) resulted in the diffraction patterns of cubic CdS (ICSD No.81925) which were similar to those of 3-CIS and 4-CIS (Figure 2.2). Compared to the β-In_2S_3 crystal structure, the formation of cubic CdS crystalline structure was found to be more favorable during the whole crystallization process. In order to further determine the crystal structure and explore structural changes, an XRD Rietveld refinement was performed on the CIS samples using the TOPAS 3.0 program. The detailed crystallographic data are shown in Table 2.1.

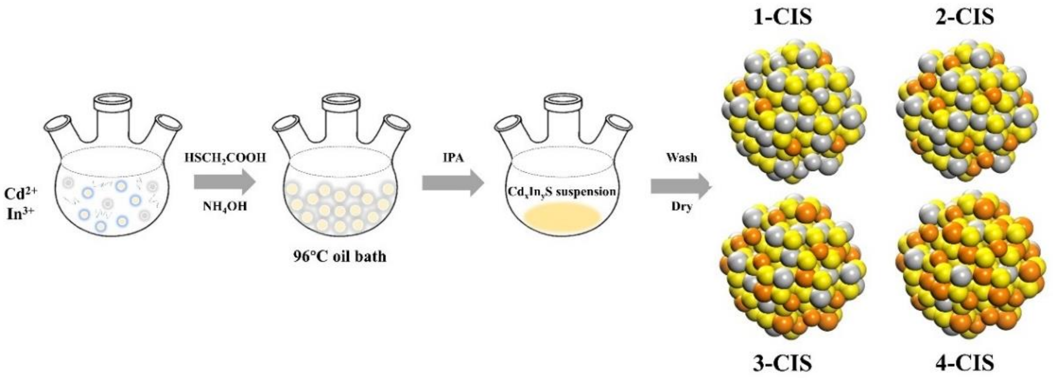

Figure 2.1 Schematic illustration of the fabrication procedure of Cd-In-S (CIS) colloids.

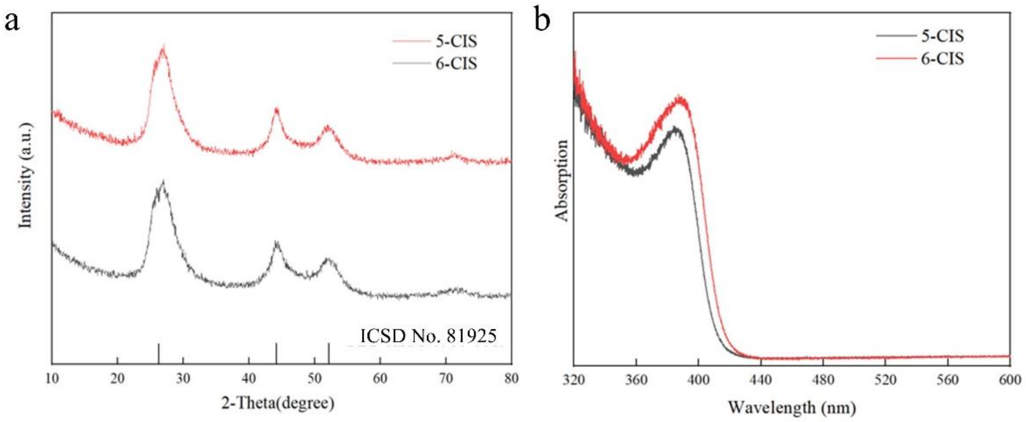

Figure 2.2 (a) XRD patterns and (b) UV-Vis absorption spectra of 5-CIS and 6-CIS.

Table 2.1 The atomic ratio of the as-prepared CIS samples measured by ICP-OES and SEM-EDS.

	1-CIS	2-CIS	3-CIS	4-CIS
ICP-OES (Cd:In)	0.26:1	0.70:1	1.55:1	3.79:1
EDS (Cd:In:S)	0.23:1:1.73	0.65:1:2.08	1.37:1:2.51	4.56:1:5.19

The ICP-OES was used to investigate the chemical composition of as-prepared CIS samples (Table 2.1). The atomic ratios of Cd to In in CIS samples were changed when increasing the amounts of $CdCl_2$ (1-CIS (0.26:1), 2-CIS (0.70:1), 3-CIS (1.55:1), 4-CIS (3.71:1)), respectively, which was in consistent with the result of the energy dispersive X-ray spectroscopy (EDS) (Table 2.2). From Table 2.1, we could observe that the (Cd+In)/S ratios of 1-CIS and 2-CIS were below 0.8, and their stoichiometric ratios were in good agreement with previously reported single crystal solid solution of $Cd_{3x}In_{2-2x}S_3$ formed by the substitution of In by Cd.[37, 38] In addition, it is noteworthy that the (Cd+In)/S ratios of 3-CIS to 6-CIS were close to 1, which is consistent with the stoichiometric ratio of CdS. The EDS result, in accordance with XRD measurement, indicates that further increasing Cd contents into CIS solid solution could induce a preferable crystallization following the structure of CdS. Based on these results, we proposed that as Cd increased in the precursor content, Cd atoms could enter the cubic structure of In_2S_3 to form substitutional In_2S_3 solid solution (1-CIS and 2-CIS). Moreover, due to the solubility limit induced by different valence states of Cd and In, the feature of

CdS crystalline structure became more evident in 3-CIS to 6-CIS samples after excessive amount of Cd was introduced, forming In substituted CdS solid solution.

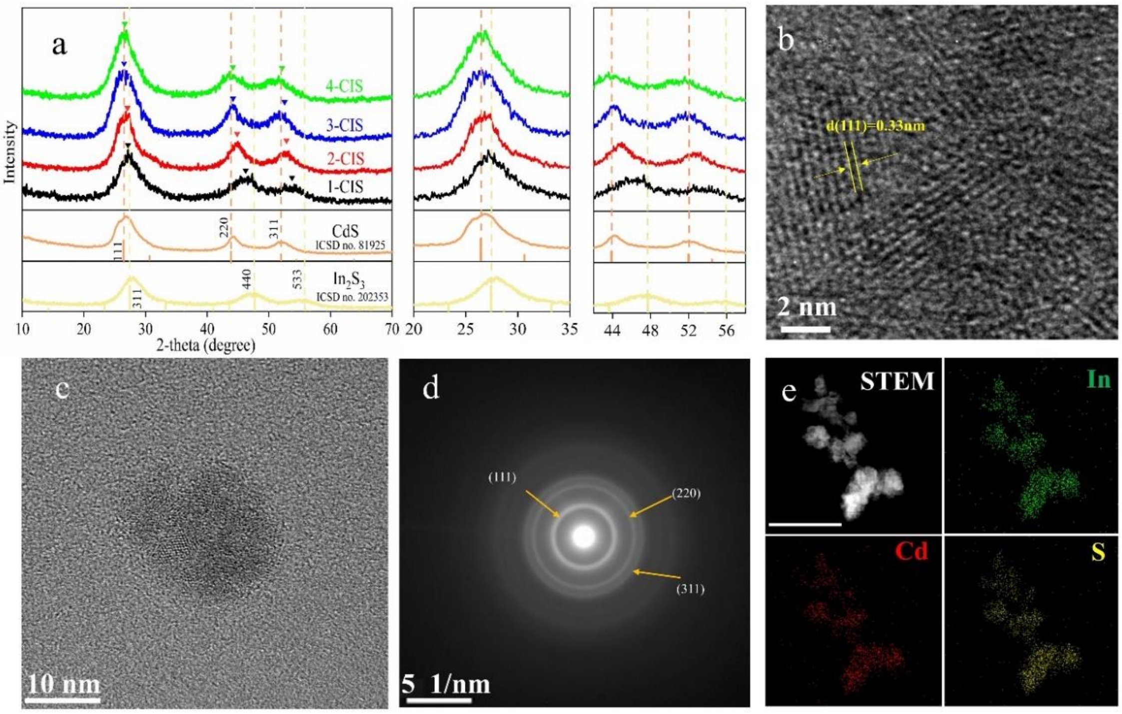

Figure 2.3 (a) XRD pattern of each CIS samples as well as CdS and In_2S_3; (b-c) HRTEM images of the 3-CIS samples; (d) selected area electron diffraction patterns and (e) EDS mapping images (Scale bar = 200 nm).

Table 2.2 Summarized chemical composition and crystalline structures of each CIS samples as well as pure In_2S_3 and CdS.

CIS sample	Atomic percentage (at%)			Composition	Lattice parameter (Å)	Crystal structure
	Cd	In	S		a = b = c	
In_2S_3	0	39.8	60.2	In_2S_3	10.770(3)	β-In_2S_3
1-CIS	7.8	33.8	58.4	$Cd_{0.13}In_{0.58}S$	11.195(8)	β-In_2S_3
2-CIS	17.4	26.8	55.8	$Cd_{0.31}In_{0.48}S$	11.285(3)	β-In_2S_3
3-CIS	28.1	20.5	51.4	$Cd_{0.55}In_{0.40}S$	5.793(3)	Cubic CdS
4-CIS	42.4	9.3	48.3	$Cd_{0.88}In_{0.19}S$	5.801(7)	Cubic CdS
5-CIS	42.5	6.7	50.8	$Cd_{0.84}In_{0.13}S$	5.804(6)	Cubic CdS
6-CIS	44.7	4.7	50.6	$Cd_{0.88}In_{0.09}S$	5.819(1)	Cubic CdS
CdS	49.6	0	50.4	CdS	5.830(5)	Cubic CdS

In order to further investigate the morphology and structures of the resulting samples, TEM and HRTEM images of the CIS samples were demonstrated in Figure 2.3b-d and Figure 2.4. A clear lattice fringe of 0.33 nm could be observed which could be attributed to the (111) facet of Cd-In-S phase (cubic CdS structure) (Figure 2.3b). The diameter of single CIS solid solution nanoparticle was estimated to be 15 nm (Figure 2.3c). The selected area electron diffraction (SAED) was shown in Figure 2.3d, and the radius of the most distinguished diffraction ring was 0.33 nm, corresponding to (111) crystal plane of the cubic CdS. The radius of second and third diffraction rings were 0.20 nm and 0.17 nm, respectively, which could be assigned to (220) and (311) crystal planes. The EDS mapping (Figure 2e) displayed a homogeneous distribution of Cd, In, and S elements in whole sample, which is the typical feature of solid solution.

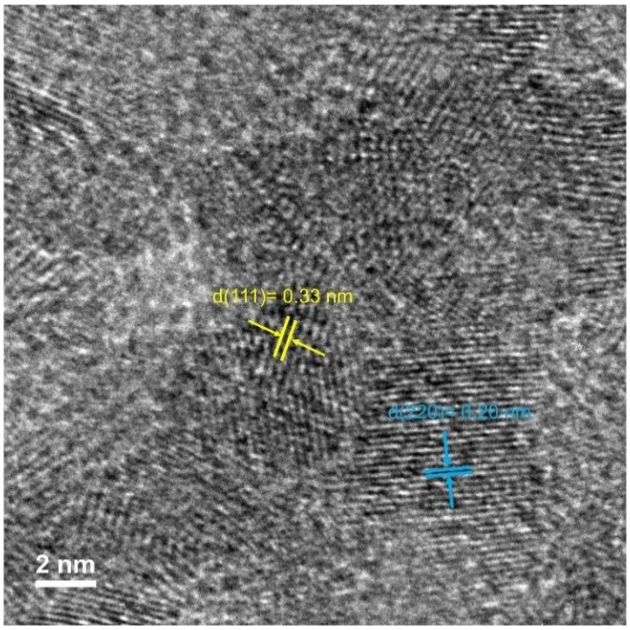

Figure 2.4 HRTEM image of 3-CIS.

XPS was utilized to investigate the surface electronic states of each element. Figure 2.5 shows the XPS survey spectra of the 3-CIS sample. Cd 3d spectra of 3-CIS sample exhibited two peaks with binding energies centered at 405.6 eV and 412.3 eV, corresponding to Cd $3d_{5/2}$ peak and Cd $3d_{3/2}$ peak, respectively. The peaks of In $3d_{5/2}$ and In $3d_{3/2}$ were located at 444.7 eV and 452.3 eV, respectively. The S 2p spectrum could be divided into two peaks centered at 161.7 eV and 163.2 eV, corresponding to the binding energy of S $2p_{3/2}$ and S $2p_{1/2,}$ which indicated the -2 valence state of S in the resulting sample.[33] In order to investigate the interaction between Cd and In in sample 1-CIS to 4-CIS, the Cd 3d and In 3d spectra of each sample were compared in Figure 2.6. With the increasing amount of Cd source during fabrication process, the Cd 3d peaks shifted to higher binding energy, gradually closing to pristine CdS, whereas the In 3d gradually shifted to lower binding energy compared to pristine In_2S_3. These results suggested that an increased Cd valance and decreased In valence were achieved with the addition of Cd atoms during fabrication process. We proposed that such an interaction between Cd and In might play critical role during the crystallization process of CIS nanocrystals, and thus endowing dramatic difference in the internal electronic structures.

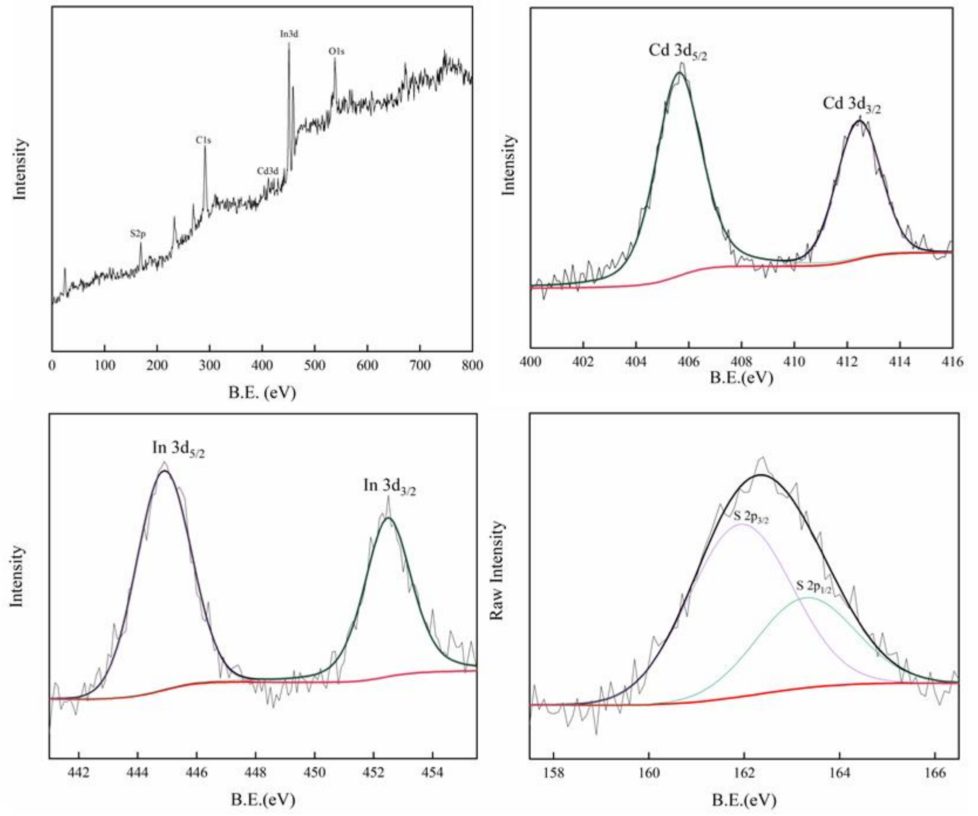

Figure 2.5 X-ray photoelectron spectra of the as-synthesized 3-CIS sample.

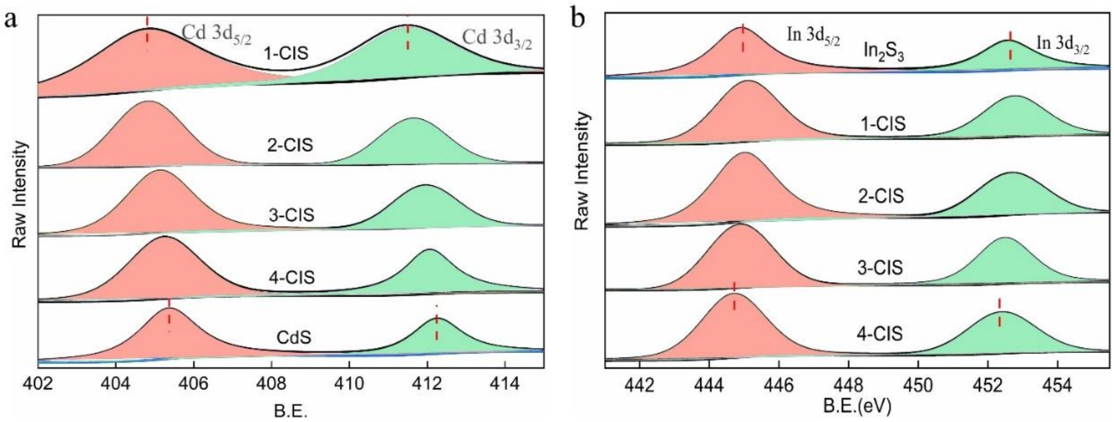

Figure 2.6 X-ray photoelectron spectra of Cd 3d spectra and In 3d spectra of the as-synthesized CIS samples as well as pristine CdS (a) and In_2S_3 (b) samples.

In order to demonstrate the advantage of as-prepared CIS catalysts, visible-light-driven CO_2 reduction was carried out in pure DMF solution. There are two reasons why DMF was employed as the solvent: (1) DMF has good CO_2 solubilization capacity, and (2) the strong coordination of DMF on the surface Cd inhibiting the adsorption and reduction of protons.[39] During all measurements, CO and H_2 were detected as the main products. Figure 2.7 showed that after 6 h of visible light irradiation, 3-CIS exhibited the best catalytic performance among all the catalysts with a CO production of 42 μmol and H_2 production of 64 μmol. The optimized photocatalytic CO_2 reduction analysis was carried out in a water/DMF mixed solution, and the photocatalytic activities were shown in Figure 2.8a. The previous report has demonstrated that water can act as both electron donor and acceptor, and the close contact between water, TEOA, and photocatalyst would facilitate for the photocatalytic CO_2 reduction. The 3-CIS sample showed a superior photocatalytic CO_2 reduction ability for the production of CO (22.9 μmol h^{-1}) as the main product with a selectivity of up to 80%. The stability test of the CIS samples for photocatalytic CO_2 reduction was carried out, and the 3-CIS sample can keep 92.1% of the original activity without adding $Co(bpy)_3^{2+}$ or TEOA to the system after 4 times tests (Figure 2.8b), which indicates a good stability.[29, 40, 41]

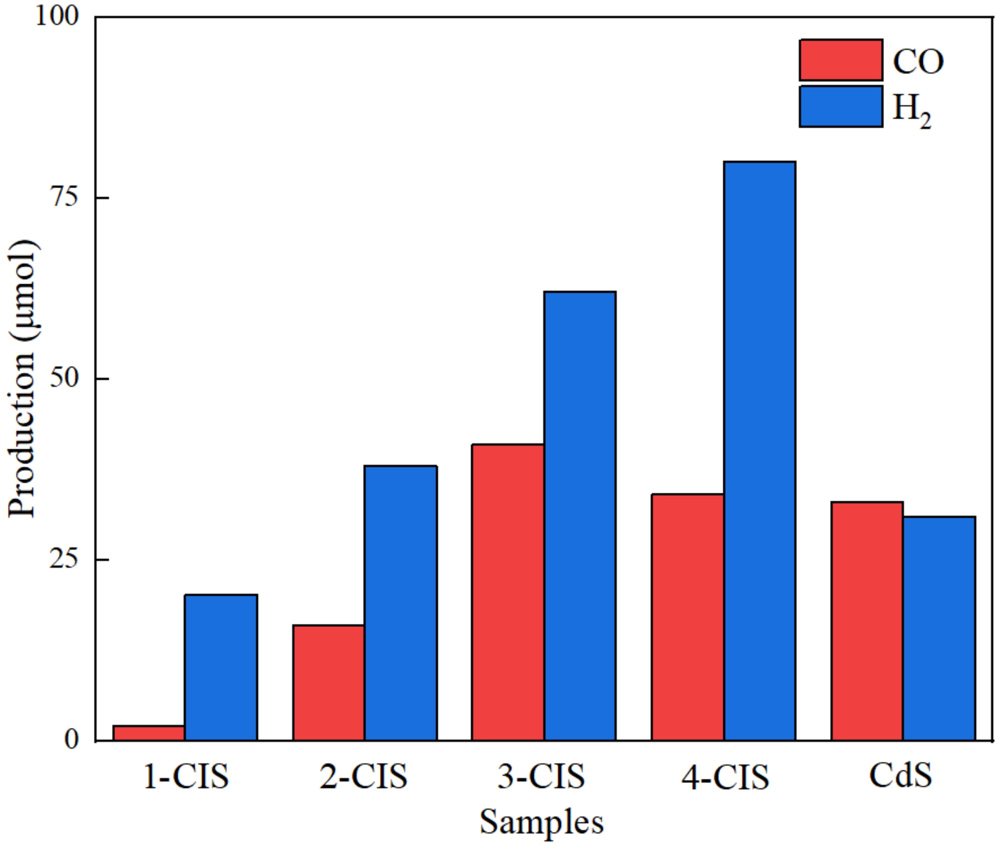

Figure 2.7 Photocatalytic CO_2 reduction activity in DMF solution.

Control experiments were carried out in water/DMF solution using 3-CIS as photocatalyst (Figure 2.8c). The results showed that no CO was produced during the reaction without the existence of gaseous CO_2 reactant and/or TEOA, indicating a critical role of CO_2 and TEOA during photocatalytic CO_2 reduction. Moreover, a small amount of CO and H_2 were produced even without adding cocatalysts of $Co(bpy)_3^{2+}$, further illustrating a good catalytic capacity of CIS for CO_2 photoreduction. The catalytic performance using different cocatalyst ($Co(bpy)_3^{2+}$ or $Ni(bpy)_3^{2+}$) was also compared, and the results showed a much lower CO production rate and lower selectivity when using $Ni(bpy)_3^{2+}$ as cocatalyst (Figure 2.8d), which might be attributed to their redox potentials. [42-44] The carbon source of produced CO was further verified using $^{13}CO_2$ isotopic labeling experiment. As shown in Figure 2.8e, ^{13}CO was detected as the product for CO_2 photoreduction, excluding the carbon source from TEOA, DMF, or other carbon-contained components. Apparent quantum yield (AQY) was used to determine the actual efficiency of photocatalytic CO_2 reduction over 3-CIS sample (Figure 2.8f), and an AQY of 1.75% was achieved at the wavelength of 400 nm, which is comparable to the representative literatures using metal sulfide as photocatalysts in liquid solution as shown in Table 2.3.[29, 40, 41]

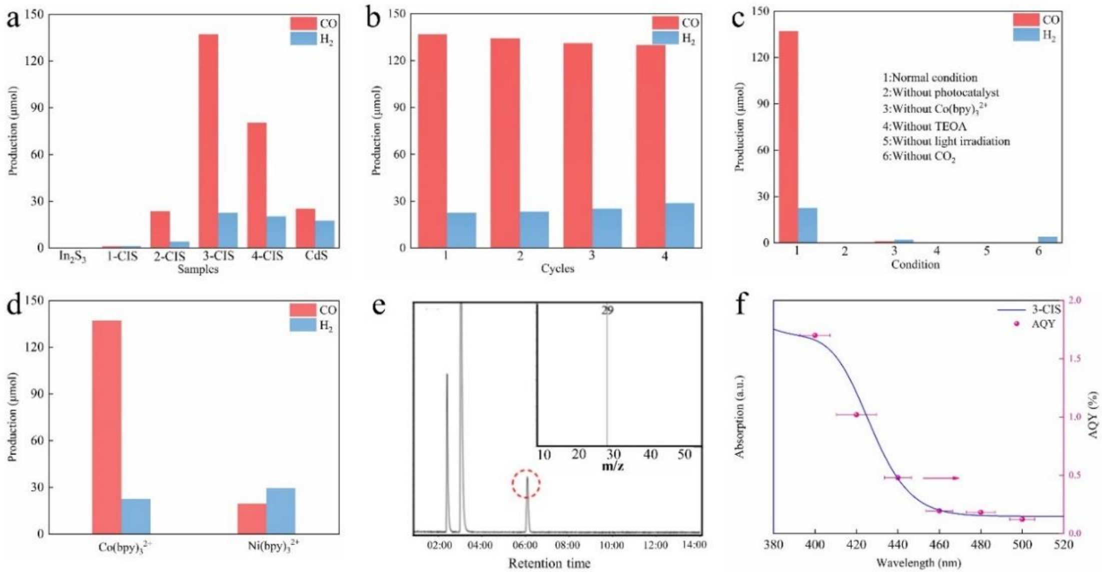

Figure 2.8 (a) Photocatalytic CO_2 reduction activity of CIS samples and CdS sample; (b) the stability test of 3-CIS; (c) control experiments of 3-CIS; (d) photocatalytic CO_2 reduction activity of 3-CIS sample with $Co(bpy)_3^{2+}$ and $Ni(bpy)_3^{2+}$ as cocatalyst; (e) GC-MS of CO obtained from photocatalytic reduction of $^{13}CO_2$ over 3-CIS and (f) UV-vis absorption spectrum and wavelength-dependent AQY of 3-CIS.

To unravel the electronic structures and optical absorption properties of the materials, UV-Vis spectra of each CIS samples in water were measured (Figure 2.9a). With the introduction of Cd, the light absorption region of each sample was gradually extended, and the bandgaps of 1-CIS to 4-CIS samples were calculated to be 2.88, 2.81, 2.75, and 2.64 eV, respectively, according to the Kubelka-Munk equation. Photoluminescence (PL) emission spectra was employed to analyze the charge separation rate of each sample (Figure 2.9b). During the measurement, the samples were excited by the light with a wavelength of 360 nm, and broad emission bands centered at about 560-610 nm were detected, which could be attributed to the large Stroke shift caused by defects and vacancies.[36, 45] The 3-CIS showed a lowest PL intensity among all the CIS samples, indicating the lowest charge carrier recombination which is beneficial to photocatalytic reaction. Furthermore, time-resolved transient photoluminescence decay (PL decay) spectra were employed to investigate the charge carrier dynamics. As shown in Figure 2.9c, the 3-CIS also showed the longest lifetime ($\tau = 1.78$ ns) of the photo-induced charge carriers, which is in accordance with the PL measurement. According to Du's report, the lifetime of the charge carriers is highly correlated with structural defects, which could trap photogenerated electrons and prolong the charge carrier lifetime.[46] As we mentioned before, there is a solubility limit due to the different valence states of Cd and In. This difference in valence could induce incomplete coordination of Cd and In with S, resulting in a large number of structural defects. During the continuous structural change of Cd-In-S from In_2S_3 to CdS phase, the structural defects showed a trend of increasing and then decreasing. The result is in accordance with the tendency of PL decay measurement (Figure 2.9c), endowed the optimal 3-CIS the best charge carrier kinetics among all the samples. In addition, the PL characterization in the aqueous solution containing 3-CIS and $Co(bpy)_3^{2+}$ cocatalyst was executed (Figure 2.9d). The PL intensity obviously decreased after adding $Co(bpy)_3^{2+}$, indicating an enhanced charge carrier separation ability which could be a key factor for improving reaction activity.

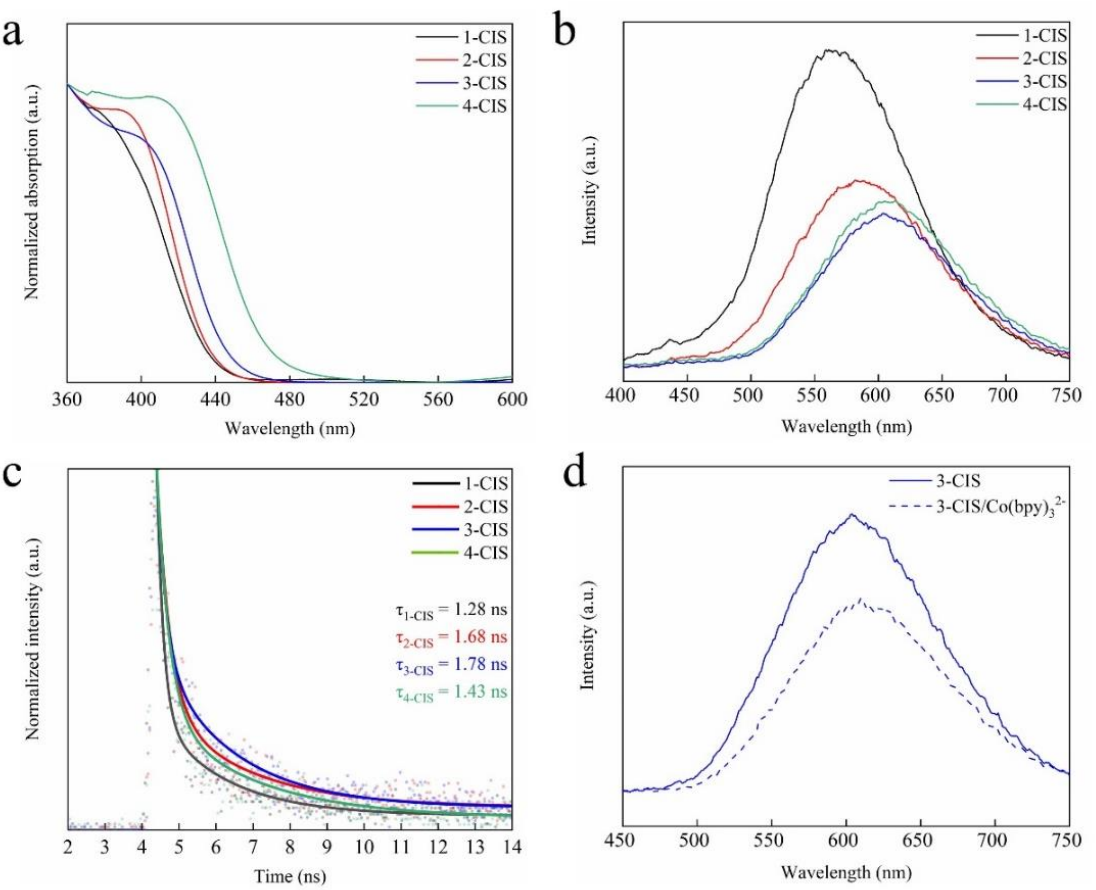

Figure 2.9 (a) UV-vis spectra (b) PL spectra and (c) time-resolved transient photoluminescence decay traces spectra of CIS samples in water; (d) PL spectra of 3-CIS and 3-CIS combining with Co(bpy)$_3^{2+}$.

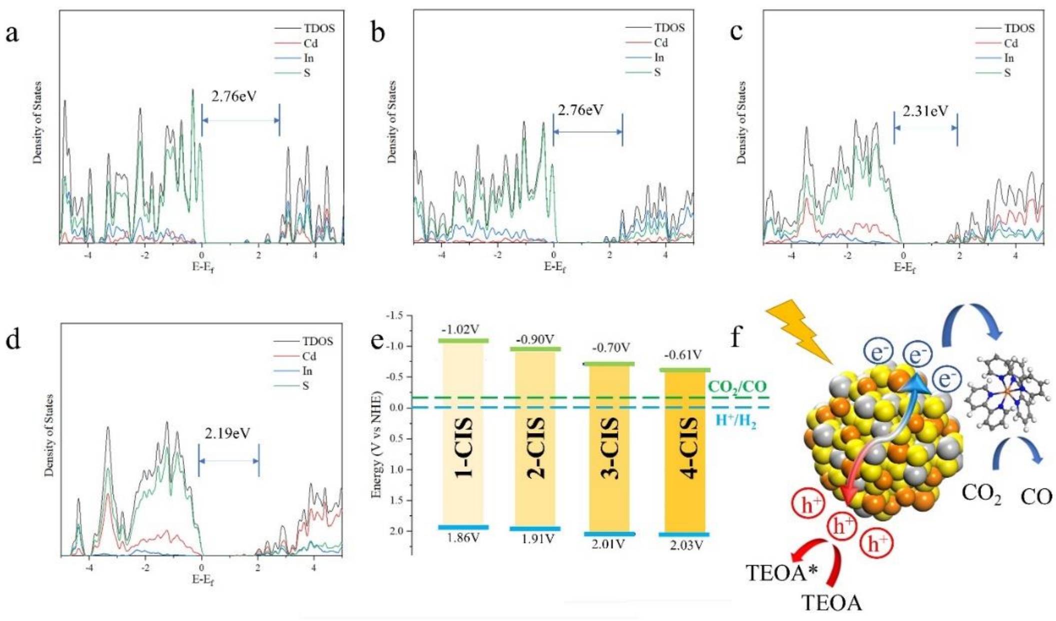

Figure 2.10 (a-d) Simulated density of states of 1-CIS to 4-CIS; (e) band edges of CIS samples; (f) proposed mechanism diagram.

The photocatalytic performance depends on not only the separation rate of charge carriers but also the reduction potential of electrons. To further illustrate how the Cd to In ratio could modulate the electronic structure of CIS semiconductor, density functional theory (DFT) based theoretical studies were carried. Figure 2.10a-d showed the density of states of each CIS (The calculated models were shown in Figure 2.11). The simulated band gaps of CIS samples showed a decreasing trend with the increasing Cd contends, which was in consistent with the trend of UV-Vis measurement. The valence band edges of CIS samples were mainly composed by S states, whereas the conduction band edges were mainly affected by Cd, In and S states together. These results suggested that the electronic structure of CIS samples was mainly influenced by the conduction band position which controlled by the Cd to In ratio. Since the potential energy of Cd 3d was much lower than that of In 5s, increasing Cd to In ratio would lead to lower conduction band edge and narrower band gap which meant a stronger light absorption ability. To further identify the band gap structure, Mott-Schottky test was utilized to estimate the Fermi level position of each CIS samples. As shown in Figure 2.12, the flatting band (FB) potentials of 1-CIS, 2-CIS, 3-CIS, and 4-CIS were estimated to be -1.02, -0.90, -0.70, and -0.61 V to NHE, respectively, which could be regarded as the conduction band (CB) edge of each CIS sample (a typical feature of n-type semiconductor). Accordingly, the band positions of each CIS sample were estimated as shown in Figure 2.10e. All CB positions of CIS were more negative than the potential of H^+/H_2 and CO_2/CO, suggesting that all the CIS photocatalysts were capable to initiate H_2 evolution and CO_2 reduction reactions. The electronic structures of CIS were dramatically affected by the molar ratio of Cd to In. Increasing the molar ratio of Cd to In induced a positive position of CB, which would narrower the band gap but reduce the reduction potential of the photo-induced electrons of CIS, thereby competitively affecting the photocatalytic performance.

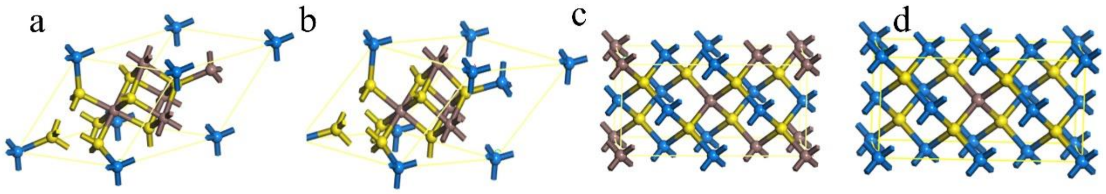

Figure 2.11 Models of (a) 1-CIS, (b) 2-CIS, (c) 3-CIS, (d) 4-CIS

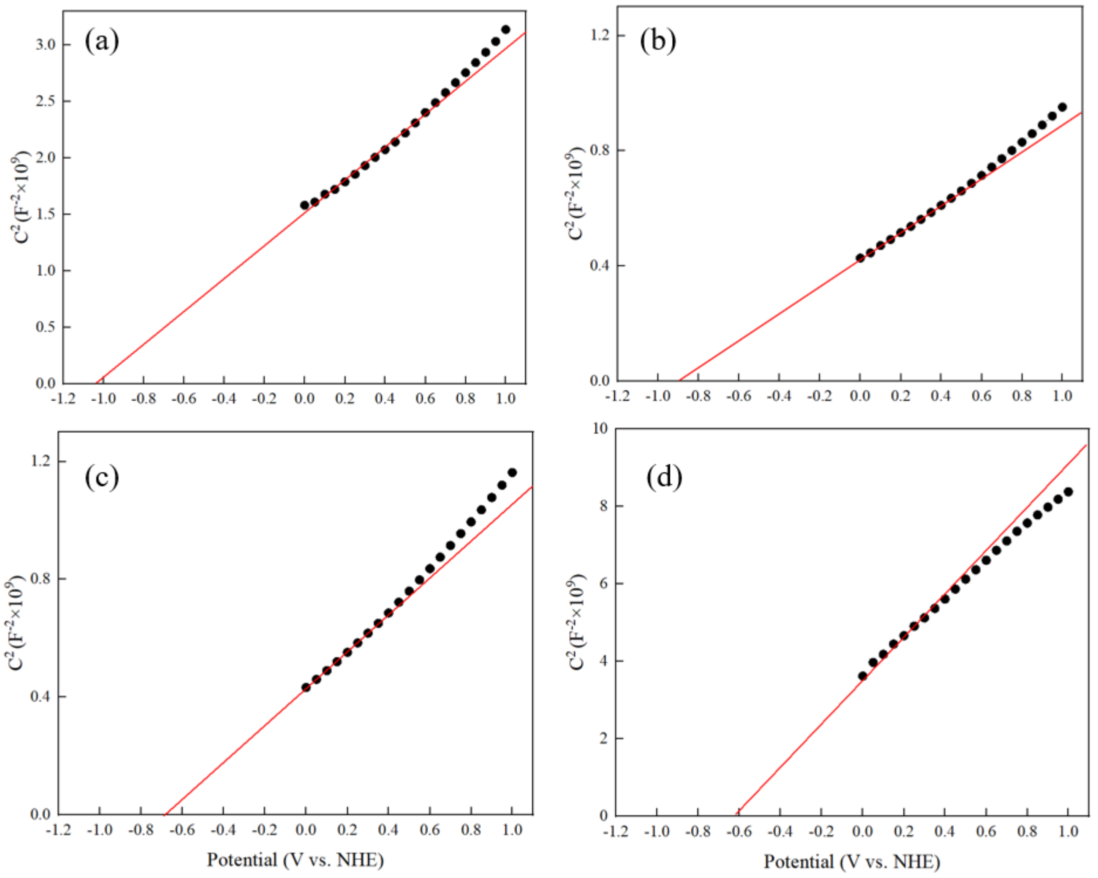

Figure 2.12 Mott-Schottky plots of (a) 1-CIS, (b) 2-CIS, (c) 3-CIS, and (d) 4-CIS.

In addition to the electronic structure of the catalysts, the interaction between CIS light absorber and cocatalyst could also play critical role in affecting the photocatalytic performance. Previous studies indicated that the photogenerated electrons can transfer from semiconductor photocatalyst to $Co(bpy)_3^{2+}$ active site and participate in the CO_2 reduction reaction. [47] The detailed reaction process can be described as follows: 1) photo-induced electrons transferred from photocatalyst to $Co^{II}(bpy)_3^{2+}$, producing $Co^{I}(bpy)_3^{+}$; 2) $Co^{I}(bpy)_3^{+}$ reacted with CO_2 to generate the intermediate $[Co^{I}(bpy)_3(CO_2)]^{+}$; 3) the reduced Co^{I} of $[Co^{I}(bpy)_3(CO_2)]^{+}$ delivered electron to CO_2 for the corresponding reducing reaction; 4) Co^{I} transferred back to Co^{II} to complete the reaction. The activity test and the PL intensity have demonstrated that the combination between CIS and $Co(bpy)_3^{2+}$ successfully enhanced charge carrier separation ability and reaction activity, illustrating that $Co(bpy)_3^{2+}$ could serve as the electron transfer channel, pumping the photo-induced electrons from CIS to CO_2 for initiating the surface reaction. Such an electron transfer process was dramatically affected by the conduction band edge of CIS samples, and more specifically, a negative band edge could facilitate the charge transfer from CIS to $Co(bpy)_3^{2+}$. The increasing the Cd to In ratio, the conduction band edge of CIS sample was positively shifted, decreasing charge transfer ability. To confirm the reaction process, the in-situ Fourier-transform infrared spectroscopy (FTIR) investigation was conducted. As shown in Figure 2.13, the broad peaks centered at 1542 cm^{-1} and 1354 cm^{-1} appeared and gradually increased during the photocatalytic CO_2 reduction process which are assigned to carbonate-type species and the adsorbed formate (COOH*) species, respectively.[48] In addition, the broad peaks centered at 3726 cm^{-1} gradually decreased during the photocatalytic CO_2 reduction process which are assigned to CO_2. These peaks indicated that there was a formation of formate intermediate (from CO_2 to COOH*) during the photocatalytic CO_2 reduction process over CIS sample which is consistent with the previously reported mechanism for the conversion of CO_2 to CO. [49]

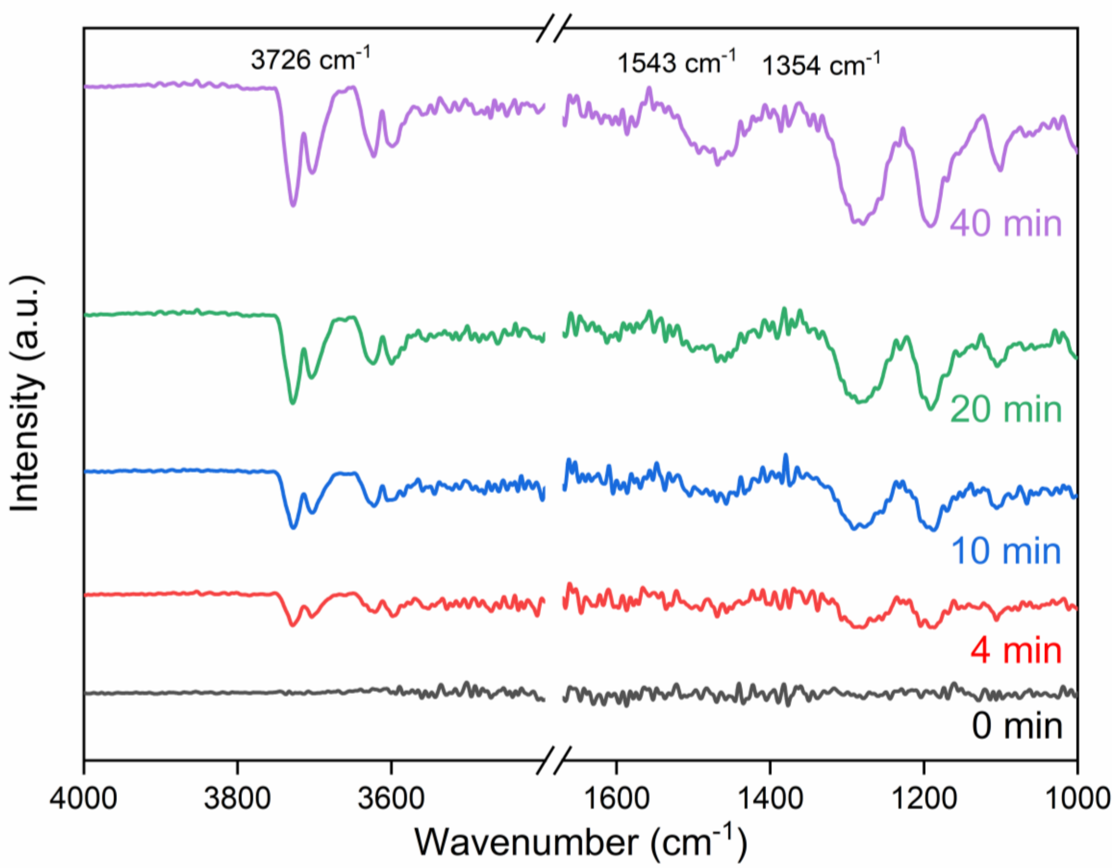

Figure 2.13 In-situ diffuse reflectance infrared Fourier transform spectroscopy for the photocatalytic CO_2 reduction over 3-CIS.

Table 2.3 Comparison of photocatalytic CO and H_2 evolution rates from CO_2 over different photocatalysts.

Photocatalysts	Reaction system	Production	Activity	Reference
Cd-In-S nanocrystal ($Cd_{0.55}In_{0.40}S$)	20 mg catalyst /DMF+TEOA/$Co(bpy)_3^{2+}$	CO H_2	CO 22.9 μmol h^{-1} (1145 μmol g^{-1} h^{-1}) H_2 5.7 μmol h^{-1} (285 μmol g^{-1} h^{-1})	This work
$CdIn_2S_4/ZnIn_2S_4$	10 mg catalyst /MeCN+TEOA+$KHCO_3$/$Co(bpy)_3^{2+}$	CO H_2	CO 1194.5 μmol g^{-1} h^{-1} H_2 475.7 μmol g^{-1} h^{-1}	Chemical Engineering Journal 442 (2022) 136309
$CdIn_2S_4$	20 mg catalyst/methanol	DMM MF	DMM 2968 μmol g^{-1} h^{-1} MF 5258 μmol g^{-1} h^{-1}	Applied Surface Science 288 (2014) 138–142
$Zn_xCd_{1-x}In_2S_4/g-C_3N_4$	50mg/ H_2O TEOA	H_2	H_2 475.7 μmol g^{-1} h^{-1}	Chemical Engineering Journal 378 (2019) 122192
WO_3 QDs/ $CdIn_2S_4$	10 mg catalyst/H_2O	CO CH_4	CO 8.2 μmol g^{-1} h^{-1} CH_4 1.6 μmol g^{-1} h^{-1}	Chemical Engineering Journal 428 (2022) 131218
$In_2O_3-C/CdIn_2S_4$	4 mg catalyst/ MeCN+H_2O+TEOA / $Co(bpy)_3^{2+}$	CO H_2	CO 2432 μmol g^{-1} h^{-1} H_2 793 μmol g^{-1} h^{-1}	ACS Appl. Mater. Interfaces 2022, 14, 20375−20384
$In_2S_3-CdIn_2S_4$	4 mg catalyst/ MeCN+H_2O+TEOA / $Co(bpy)_3^{2+}$	CO H_2	CO 825 μmol g^{-1} h^{-1} H_2 260 μmol g^{-1} h^{-1}	J. Am. Chem. Soc. 2017, 139, 17305−17308
$AgInS_2$ QDs	20 mg catalyst /DMF+TEOA/$Co(bpy)_3^{2+}$	CO H_2	CO 9.2 μmol h^{-1} H_2 3.1 μmol h^{-1}	Journal of Catalysis 401 (2021) 271–278
$CuGaS_2/CdS$	200 mg catalyst/ H_2O+ K_2SO_3+$KHCO_3$	CO H_2	CO 0.15 μmol h^{-1} H_2 34 μmol h^{-1}	Nanoscale 12 (16) 8693-8700
Ni doped CdS quantum dots	H_2O+TEOA	CO H_2	CO 9.5 μmol g^{-1} h^{-1}	Angew. Chem. Int. Ed. 2018, 57, 16447 –16451

From the above theoretical and experimental results, the modulated CO_2 reduction performance upon Cd introduction can be ascribed by three aspects: 1) tailoring the electronic structure, 2) regulating the charge transfer between photocatalyst to $Co(bpy)_3^{2+}$ and 3) modulating the charge carrier lifetime, and all of them were ultimately controlled by the Cd to In ratio of the catalysts. The band gaps of CIS samples were mainly affected by Cd to In ratio, and an increased Cd to In ratio would lead to a narrower band gap which is beneficial for light harvesting. Meanwhile, the position of conduction band edges would be negatively affected by increasing Cd to In ratio, resulting in a decreased charge transfer ability between CIS and $Co(bpy)_3^{2+}$ and reduced reduction potential of electrons, which is unfavorable for photocatalytic CO_2 reduction. In addition, the charge carrier lifetime was also influenced by structural defects which are directly related to Cd to In ratio. The optimized electronic structure, charge transfer behavior and charge carrier lifetime rendered the 3-CIS sample an outstanding catalytic performance towards CO_2 reduction.

2.4 Conclusions

In this study, Cd-In-S colloids samples with different Cd to In ratio was constructed for high-efficient visible-light-driven CO_2 reduction. The CO production rate of 22.9 $\mu mol \cdot h^{-1}$ was achieved at the optimized condition when using $Co(bpy)_3^{2+}$ as cocatalyst. Furthermore, an AQY up to 1.75% was reached at wavelength of 400 nm. The mechanistic investigation revealed that by the introduction of Cd, both the electronic structure of Cd-In-S solid solution and the charge transfer behavior between Cd-In-S and cocatalysts can be modulated, which synergistically determine the overall catalytic performance. The findings in this work offer a unique insight into the construction and modulation strategy of bimetallic sulfide-based photocatalysts towards CO_2 reduction.

References

[1] H. Tong, S. Ouyang, Y. Bi, N. Umezawa, M. Oshikiri, J. Ye, Nano-photocatalytic materials: possibilities and challenges, Adv Mater, 24 (2012) 229-251.

[2] H. Lin, S. Luo, H. Zhang, J. Ye, Toward solar-driven carbon recycling, Joule, 6 (2022) 294-314.

[3] S. Gao, Y. Lin, X. Jiao, Y. Sun, Q. Luo, W. Zhang, D. Li, J. Yang, Y. Xie, Partially oxidized atomic cobalt layers for carbon dioxide electroreduction to liquid fuel, Nature, 529 (2016) 68-71.

[4] C. Cometto, R. Kuriki, L. Chen, K. Maeda, T.C. Lau, O. Ishitani, M. Robert, A Carbon Nitride/Fe Quaterpyridine Catalytic System for Photostimulated CO_2-to-CO Conversion with Visible Light, J Am Chem Soc, 140 (2018) 7437-7440.

[5] A. Manzi, T. Simon, C. Sonnleitner, M. Doblinger, R. Wyrwich, O. Stern, J.K. Stolarczyk, J. Feldmann, Light-induced cation exchange for copper sulfide based CO_2 reduction, J Am Chem Soc, 137 (2015) 14007-14010.

[6] D.J. Boston, C. Xu, D.W. Armstrong, F.M. MacDonnell, Photochemical reduction of carbon dioxide to methanol and formate in a homogeneous system with pyridinium catalysts, J Am Chem Soc, 135 (2013) 16252-16255.

[7] S. Neatu, J.A. Macia-Agullo, P. Concepcion, H. Garcia, Gold-copper nanoalloys supported on TiO_2 as photocatalysts for CO_2 reduction by water, J Am Chem Soc, 136 (2014) 15969-15976.

[8] W. Tu, Y. Zhou, Z. Zou, Photocatalytic conversion of CO_2 into renewable hydrocarbon fuels: state-of-the-art accomplishment, challenges, and prospects, Adv Mater, 26 (2014) 4607-4626.

[9] H.Q. Xu, J. Hu, D. Wang, Z. Li, Q. Zhang, Y. Luo, S.H. Yu, H.L. Jiang, Visible-Light Photoreduction of CO_2 in a Metal-Organic Framework: Boosting Electron-Hole Separation via Electron Trap States, J Am Chem Soc, 137 (2015) 13440-13443.

[10] L. Wang, X. Zhang, L. Yang, C. Wang, H. Wang, Photocatalytic reduction of CO_2coupled with selective alcohol oxidation under ambient conditions, Catal. Sci. Technol., 5 (2015) 4800-4805.

[11] X. Chang, T. Wang, J. Gong, CO_2 photo-reduction: insights into CO_2 activation and reaction on surfaces of photocatalysts, Energy Environ. Sci., 9 (2016) 2177-2196.

[12] X. Ren, F. Liu, Q. Wang, H. Song, S. Luo, S. Li, G. Yang, B. Deng, Z. Huang, X.-S. Wang, L. Shi, J. Ye, Engineering interfacial charge transfer channel for efficient photocatalytic H_2 evolution: The interplay of CoP_x and Ca^{2+} dopant, Appl. Catal., B Environ, 303 (2022) 120887.

[13] X. Meng, S. Ouyang, T. Kako, P. Li, Q. Yu, T. Wang, J. Ye, Photocatalytic CO_2 conversion over alkali modified TiO_2 without loading noble metal cocatalyst, Chem Commun (Camb), 50 (2014) 11517-11519.

[14] X. Meng, Q. Yu, G. Liu, L. Shi, G. Zhao, H. Liu, P. Li, K. Chang, T. Kako, J. Ye, Efficient photocatalytic CO_2 reduction in all-inorganic aqueous environment: Cooperation between reaction medium and Cd(II) modified colloidal ZnS, Nano Energy, 34 (2017) 524-532.

[15] S. Wang, X. Hai, X. Ding, S. Jin, Y. Xiang, P. Wang, B. Jiang, F. Ichihara, M. Oshikiri, X. Meng, Y. Li, W. Matsuda, J. Ma, S. Seki, X. Wang, H. Huang, Y. Wada, H. Chen, J. Ye, Intermolecular cascaded pi-conjugation channels for electron delivery powering CO_2 photoreduction, Nat Commun, 11 (2020) 1-9.

[16] Y. Li, S. Wang, X.S. Wang, Y. He, Q. Wang, Y. Li, M. Li, G. Yang, J. Yi, H. Lin, D. Huang, L. Li, H. Chen, J. Ye, Facile Top-Down Strategy for Direct Metal Atomization and Coordination Achieving a High Turnover Number in CO_2 Photoreduction, J Am Chem Soc, 142 (2020) 19259-19267.

[17] B. Deng, H. Song, K. Peng, Q. Li, J. Ye, Metal-organic framework-derived Ga-Cu/CeO_2 catalyst for highly efficient photothermal catalytic CO2 reduction, Appl. Catal., B Environ, 298 (2021) 120519.

[18] H. Huang, H. Song, J. Kou, C. Lu, J. Ye, Atomic-level insights into surface engineering of semiconductors for photocatalytic CO_2 reduction, J. Energy Chem., 67 (2022) 309-341.

[19] H. Pang, X. Meng, P. Li, K. Chang, W. Zhou, X. Wang, X. Zhang, W. Jevasuwan, N. Fukata, D. Wang, J. Ye, Cation Vacancy-Initiated CO_2 Photoreduction over ZnS for Efficient Formate Production, ACS Energy Lett., 4 (2019) 1387-1393.

[20] H. Pang, X. Meng, H. Song, W. Zhou, G. Yang, H. Zhang, Y. Izumi, T. Takei, W. Jewasuwan, N. Fukata, J. Ye, Probing the role of nickel dopant in aqueous colloidal ZnS nanocrystals for efficient solar-driven CO_2 reduction, Appl. Catal., B Environ, 244 (2019) 1013-1020.

[21] X. Meng, G. Zuo, P. Zong, H. Pang, J. Ren, X. Zeng, S. Liu, Y. Shen, W. Zhou, J. Ye, A rapidly room-temperature-synthesized Cd/ZnS:Cu nanocrystal photocatalyst for highly efficient solar-light-powered CO_2 reduction, Appl. Catal., B Environ, 237 (2018) 68-73.

[22] X. Zhang, D. Kim, L.Y.S. Lee, Copper-Doped ZnS with Internal Phase Junctions for Highly Selective CO Production from CO_2 Photoreduction, ACS Appl. Energy Mater., 4 (2021) 2586-2592.

[23] A. Raja, N. Son, M. Swaminathan, M. Kang, Facile synthesis of sphere-like structured $ZnIn_2S_4$-rGO-$CuInS_2$ ternary heterojunction catalyst for efficient visible-active photocatalytic hydrogen evolution, J Colloid Interface Sci, 602 (2021) 669-679.

[24] P. Li, X. Jia, J. Zhang, J. Li, J. Zhang, L. Wang, J. Wang, Q. Zhou, W. Wei, X. Zhao, S. Wang, H. Sun, The roles of gold and silver nanoparticles on $ZnIn_2S_4$/silver (gold)/tetra(4-carboxyphenyl)porphyrin iron(III) chloride hybrids in carbon dioxide photoreduction, J Colloid Interface Sci, 628 (2022) 831-839.

[25] M. Yu, X. Lv, A. Mahmoud Idris, S. Li, J. Lin, H. Lin, J. Wang, Z. Li, Up conversion nanoparticles coupled with hierarchical $ZnIn_2S_4$ nanorods as a near-infrared responsive photocatalyst for photocatalytic CO_2 reduction, J Colloid Interface Sci, 612 (2022) 782-791.

[26] X. Jiao, Z. Chen, X. Li, Y. Sun, S. Gao, W. Yan, C. Wang, Q. Zhang, Y. Lin, Y. Luo, Y. Xie, Defect-Mediated Electron-Hole Separation in One-Unit-Cell $ZnIn_2S_4$ Layers for Boosted Solar-Driven CO_2 Reduction, J Am Chem Soc, 139 (2017) 7586-7594.

[27] J.Y. Chang, S.C. Chang, S.H. Tzing, C.H. Li, Development of nonstoichiometric $CuInS_2$ as a light-harvesting photoanode and catalytic photocathode in a sensitized solar cell, ACS Appl Mater Interfaces, 6 (2014) 22272-22281.

[28] L. Shi, X. Ren, Z. Zhang, Q. Wang, Y. Li, J. Ye, Non-stoichiometric Ag-In-S quantum dots for efficient photocatalytic CO_2 reduction: Ag/In molar ratio dependent activity and selectivity, J. Catal., 401 (2021) 271-278.

[29] S. Wu, H. Pang, W. Zhou, B. Yang, X. Meng, X. Qiu, G. Chen, L. Zhang, S. Wang, X. Liu, R. Ma, J. Ye, N. Zhang, Stabilizing $CuGaS_2$ by crystalline CdS through an interfacial Z-scheme charge transfer for enhanced photocatalytic CO_2 reduction under visible light, Nanoscale, 12 (2020) 8693-8700.

[30] G. Fu, J.-M. Lee, Ternary metal sulfides for electrocatalytic energy conversion, J. Mater. Chem. A, 7 (2019) 9386-9405.

[31] K. Das, S.K. Panda, S. Gorai, P. Mishra, S. Chaudhuri, Effect of Cu/In molar ratio on the microstructural and optical properties of microcrystalline $CuInS_2$ prepared by solvothermal route, Mater. Res. Bull., 43 (2008) 2742-2750.

[32] B. Huang, R. Xu, L. Zhang, Y. Yuan, C. Lu, Y. Cui, J. Zhang, Effect of Cu/In ratio and shell thickness on the photo-stability of $CuInS_2/ZnS$ nanocrystals, J. Mater. Chem. C, 5 (2017) 12151-12156.

[33] X. Li, X. Yan, N. Zhao, J. Zhao, B. Lu, X. Zhang, X. Zhang, H. Yu, Facile synthesis of ternary $CdIn_2S_4/In(OH)_3/Zn_2GeO_4$ nanocomposite with enhanced visible-light photocatalytic H_2 evolution, J. Photochem. Photobiol., A, 360 (2018) 298-305.

[34] Y.-C. Chen, H.-H. Chang, Y.-K. Hsu, Synthesis of $CuInS_2$ Quantum Dots/In_2S_3/ZnO Nanowire Arrays with High Photoelectrochemical Activity, ACS Sustain. Chem. Eng., 6 (2018) 10861-10868.

[35] S. Peng, S.G. Mhaisalkar, S. Ramakrishna, Solution synthesis of $CdIn_2S_4$ nanocrystals and their photoelectrical application, Mater. Lett., 79 (2012) 216-218.

[36] J. Feng, H. Zhu, X. Wang, X. Yang, Composition-dependent fluorescence emission of ternary Cd-In-S alloyed quantum dots, Chem Commun (Camb), 48 (2012) 5452-5454.

[37] I.A. Damaskin, Physhkin, S. L., Radautsan, S. I., & Tazlavan, V. E., Some luminescence properties of the $(CdS)_{3x}$–$(In_2S_3)_{1-x}$ system, Phys. Status Solidi A, 6 (1971) 425-429.

[38] S.I. Radautsan, Syrbu, N. N., Tezlevan, V. E., Sherban, K. F., & Strumban, E. E., Optical and photoelectrical properties and band structure of single crystals of solid solutions of the system $(CdS)_{3x}$–$(In_2S_3)_{1-x}$, Phys. Status Solidi A, 15 (1973) 295-302.

[39] H.H. Hiroaki Fujiwara, Kei Murakoshi, Yuji Wada, and Shozo Yanagida*, Effect of Surface Structures on Photocatalytic CO_2 Reduction Using Quantized CdS Nanocrystallites, J. Phys. Chem. B, 101 (1997) 8270-8278.

[40] P. Zhang, S. Wang, B.Y. Guan, X.W. Lou, Fabrication of CdS hierarchical multi-cavity hollow particles for efficient visible light CO_2 reduction, Energy Environ. Sci., 12 (2019) 164-168.

[41] Z. Zhu, X. Li, Y. Qu, F. Zhou, Z. Wang, W. Wang, C. Zhao, H. Wang, L. Li, Y. Yao, Q. Zhang, Y. Wu, A hierarchical heterostructure of CdS QDs confined on 3D $ZnIn_2S_4$ with boosted charge transfer for photocatalytic CO_2 reduction, Nano Res., 14 (2020) 81-90.

[42] A.J. Morris, G.J. Meyer, E. Fujita, Molecular approaches to the photocatalytic reduction of carbon dioxide for solar fuels, Acc. Chem. Res., 42 (2009) 983-1994.

[43] J. Lin, B. Qin, Z. Fang, Nickel Bipyridine (Ni(bpy)$_3$Cl$_2$) Complex Used as Molecular Catalyst for Photocatalytic CO$_2$ Reduction, Catal. Lett., 149 (2018) 25-33.

[44] D.-C. Liu, D.-C. Zhong, T.-B. Lu, Non-noble metal-based molecular complexes for CO$_2$ reduction: From the ligand design perspective, EnergyChem, 2 (2020) 100034.

[45] S.H. You, K.J. Hong, T.S. Jeong, C.J. Youn, J.S. Park, B.J. Lee, J.W. Jeong, Point defect study from low photoluminescence of the CdIn$_2$S$_4$ films grown by hot wall epitaxy method, J. Cryst. Growth, 271 (2004) 391-397.

[46] J. Du, S. Ma, H. Liu, H. Fu, L. Li, Z. Li, Y. Li, J. Zhou, Uncovering the mechanism of novel AgInS$_2$ nanosheets/TiO$_2$ nanobelts composites for photocatalytic remediation of combined pollution, Appl. Catal., B Environ, 259 (2019).

[47] J. Lin, Y. Hou, Y. Zheng, X. Wang, Integration of [(Co(bpy)$_3$]$^{2+}$ electron mediator with heterogeneous photocatalysts for CO$_2$ conversion, Chem Asian J, 9 (2014) 2468-2474.

[48] B. Han, X. Ou, Z. Deng, Y. Song, C. Tian, H. Deng, Y.J. Xu, Z. Lin, Nickel Metal-Organic Framework Monolayers for Photoreduction of Diluted CO$_2$: Metal-Node-Dependent Activity and Selectivity, Angew Chem Int Ed Engl, 57 (2018) 16811-16815.

[49] Y. Liu, S. Chen, X. Quan, H. Yu, Efficient Electrochemical Reduction of Carbon Dioxide to Acetate on Nitrogen-Doped Nanodiamond, J Am Chem Soc, 137 (2015) 11631-11636.

Chapter 3 Nanoscale Ag-In-S quantum dots towards efficient photocatalytic CO_2 reduction with Ag/In molar ratio dependent activity and selectivity

3.1 Introduction

Syngas (synthesis gas, $CO + H_2$) has been proven to be a valuable and versatile fuel because it can be not only directly utilized in internal combustion engines but also converted into liquid hydrocarbon fuels through the Fischer–Tropsch processes.[1] Currently, syngas is predominantly produced by the thermocatalytic and electrocatalytic strategies, which require massive energy input and harsh reaction conditions.[2] The production of syngas with low energy input is a great challenge in the sustainable chemical industry. Photocatalytic CO_2 reduction to CO accompanies with H_2 evolution utilizing the solar energy as sole energy input under mild conditions represents an ideal strategy for syngas production.[3, 4] During the past decades, tremendous efforts have been devoted to design highly active, cheap and robust materials to achieve efficient photocatalytic CO_2 reduction to produce syngas. Several homogeneous photosensitizers, containing precious metals such as Re, Ru and Ir or earth-abundant metals such as Cu are capable of photoreducing CO_2 to syngas.[5-7] These photosensitizers, however, commonly suffer from the high cost and complex synthetic process, as well as the severe photo-corrosion and difficult recycling for long-term use, which significantly limit their large scale practical applications.[5] The heterogeneous inorganic semiconductors including metal oxides (TiO_2, $SrTiO_3$, $BaLa_4Ti_4O_{15}$, etc.) and metal sulfides (CdS, $CdIn_2S_4$, etc.) have been recently intensively investigated as alternatives to homogeneous photosensitizers for photocatalytic reducing CO_2 to syngas.[8-12] Nevertheless, their photocatalytic performances are still far from satisfactory, largely because of the sluggish kinetics of separation and transfer of photogenerated charge carriers, especially over bulk semiconductors. Discovering novel photocatalysts that can efficiently convert CO_2 to syngas is highly desirable but is a big challenge.

Semiconductor quantum dots (QDs) are emerging as attractive materials for solar energy conversion applications, for example photocatalytic CO_2 reduction.[13] Compared with bulk photocatalysts, QDs exhibit unique characteristics such as high surface area-to-volume ratios, abundant surface active sites and short charge-transfer lengths, which enable them great potentials for CO_2 adsorption and activation.[13] Besides, the abundant functional groups located on the surfaces of QDs can facilitate the chemisorption of molecular cocatalysts to form quasi-static complexes that enable the ultrafast charge transfer, which could provide long lifetime of electrons for promoting the kinetics of multi-electron and multi-proton involved CO_2 reduction.[14] Up to now, various QDs including CdS, CdSe, PbS, $CuInS_2$, $CH_3NH_3PbI_3$ and $CsPbBr_3$ have demonstrated their intrinsic advantages in photocatalytic CO_2 reduction.[15-20] However, most of the reported QDs photocatalysts contain Cd or Pb heavy-metal elements, and their practical applications are greatly hindered due to their high toxicity and their instability to photon and air.[13] Thus, it is urgent to explore new kinds of Cd and Pb free QDs photocatalysts for efficient, selective and stable CO_2 photoreduction to produce syngas.

Herein, we report for the first time that non-stoichiometric Ag-In-S QDs can be used as highly active and stable photocatalysts for visible-light-driven photocatalytic syngas production from CO_2 reduction in the presence of $Co(bpy)_3^{2+}$ (bpy = 2′2-bipyridine, abbreviated to CoBPY) as a molecular cocatalyst. The CoBPY has been demonstrated as an effective cocatalyst that not only promotes the conversion of CO_2 to CO reaction but also improves the photo-stability of Ag-In-S QDs. The experimental results show that the photocatalytic activity and selectivity are strongly dependent on the Ag to In molar ratios in Ag-In-S QDs, with the Ag to In molar ratio of 0.154:1 exhibiting the highest CO production rate of 9.20 μmol h^{-1} and H_2 production rate of 3.13 μmol h^{-1}, corresponding to the highest CO selectivity of 74.6%, outperforming most of the reported QDs based photocatalysts. The mechanism investigation reveals that increasing the Ag to In molar ratios in Ag-In-S QDs results in the enhancement of the charge carriers lifetime, improved light absorption ability and decreased reduction potential of electrons, which play competitive roles in the photocatalytic CO_2 reduction reaction, therefore the optimized activity is obtained when the Ag to In molar ratio in Ag-In-S QDs is 0.154:1.

3.2 Experimental section

3.2.1 Materials preparation

Preparation of QDs

The Ag-In-S QDs were synthesized according to the reported literature with a slight modification.[21] In the typical synthesis of 2Ag-In-S QDs, 0.1 M $AgNO_3$ (1.0 ml), 1.0

M mercaptoacetic acid (2.0 ml) and 5.0 M NH_4OH (0.2 ml) were added one by one into 8 ml of H_2O, and a yellowish solution was formed under stirring and ambient conditions. After quickly dropping 0.45 ml of 5.0 M NH_4OH, the yellowish solution becomes transparent. Then, 0.7 ml of 1.0 M $InCl_3$ containing 0.2 M HNO_3 was added. After that, 1.0 ml of 1.0 M fresh Na_2S solution was added. After stirring for 5 min, the above solution was transferred to oil bath at 90 ^{o}C for 30 min. After cooled to room temperature, 40 ml of 2-propanol was added into the solution for the QDs precipitation. The QDs precipitation was achieved by high-speed centrifugation and washing with 2-propanol for several times. The QDs powder was achieved by drying in vacuum oven under 50 ^{o}C overnight. The In_2S_3 QDs, 1Ag-In-S QDs, and 3Ag-In-S QDs were obtained in a same procedure except that 0 ml of $AgNO_3$, 0.6 ml of $AgNO_3$ and 1.5 ml of $AgNO_3$ were added, respectively.

3.2.2 Photocatalytic syngas production from CO_2 reduction

The photocatalytic CO_2 reduction of QDs was conducted in a liquid-solid reaction system at ambient conditions. In a typical procedure, 2′2-bipyridine (20 mg) and $CoCl_2$ (1 μmol) were mixed with 35 ml of DMF in a quartz reactor. The solution was then stirred for 10 min. After that, 20 mg of Ag-In-S QDs powder was added in above DMF solution, which was stirred and sonicated for 5 min to achieve a well-dispersed solution, and then 7 ml of TEOA solution was dropped and the mixture was further stirred for 5 min. The quartz reactor was set to the air-closed photocatalytic reaction system. After removing the air by evacuation for 15 min, the photocatalytic system was injected with 1 bar pure CO_2 gas. The photocatalytic reaction proceeds by applying a 300 W Xe lamp combined with a UV cutoff filter ($\lambda > 400$ nm), and the light intensity is measured to be 254.7 mW/cm^2. During the photocatalytic reaction, a cooling water filter was set between the reactor and lamp to remove the heat effect. The CO was measured by gas chromatography (GC-14B, Shimadzu Co., Japan) and the H_2 was measured by gas chromatography (GC-8A, Shimadzu Co., Japan).

The selectivity of CO is calculated based on the following equation:

$$Selectivity\ of\ CO\ (\%) = \frac{amount\ of\ generated\ CO}{amount\ of\ generated\ CO\ and\ H_2} \times 100\%$$

The procedure for the isotope-labeled experiment were the same as described above expect that $^{13}CO_2$ was used as reactant instead of $^{12}CO_2$, and the produced gas was measured and analyzed by GC-mass (JEOL-GCQMS, JMS-K9 and 6890N Network GC system, Agilent Technologies). We conducted the cycling experiment as described below. The photocatalytic system after one cycle was evacuated to remove the gas completely, and then 1 bar pure CO_2 gas was injected for the next photocatalytic reaction test.

3.2.3 Characterization

The crystal structures of QDs were analyzed by XRD patterns on X'Pert PRO diffractometer (PANalytical). The optical properties of QDs were analyzed by UV-vis spectrum on SHIMADZU UV-2600. The HRTEM images and EDX of QDs were measured by a transmission electron microscope (TEM, 2100F, JEOL Co., Japan). The elemental analysis and chemical states of Ag-In-S QDs were recorded by X-ray photoelectron spectroscopy (XPS, VG-ESCA Mark II). The PL decay lifetime data were obtained from Hamamatsu instrument (Hamamatsu C5680, Japan), and the excitation wavelength is set at 400 nm. The ICP-AES measurements were performed on Agilent 7900 ICP-MS. The Mott-Schottky tests were conducted in the dark at 1000 Hz on an electrochemical station (ALS/CH model 650A, Japan) using the Ag-In-S QDs photoanode as the working electrode in a typical three-electrode cell with 50 ml of 0.5 M Na_2SO_4 solution as electrolyte.

3.2.3 Computational details

Our DFT calculations were carried out through using PWSCF code from the Quantum ESPRESSO program package. The generalized gradient approximation (GGA) in the scheme of Perdew, Burke and Ernzerrof (PBE) were applied for exchange and correlation potential. We relaxed all the geometry structures with the energy converged less than 1×10-6 Ry. We applied the cutoff energy of 45 Ry for the real-space integration grid. In addition, the Brillouin zone was sampled by 3×3×3 and 5×5×5 k-points grid for optimization and density of states, respectively. We also used the DFT-D2 method for the van der Waals correction.

3.3 Results and discussion

3.3.1 Characterization of Ag-In-S QDs

The In_2S_3 QDs and Ag-In-S QDs with different Ag to In molar ratio were prepared based on a modified literature procedure.[21] Three Ag-In-S QDs samples (named as 1Ag-In-S, 2Ag-In-S and 3Ag-In-S) were prepared and their Ag to In molar ratios were recorded by the Inductively Coupled Plasma Atomic Emission Spectroscopy (ICP-AES), which were 0.094:1, 0.154:1 and 0.216:1, respectively. The Ag to In molar ratios in Ag-In-S QDs are much lower than the stoichiometric ratio of Ag to In (1:1) in $AgInS_2$ crystal. The In_2S_3 QDs is in white color, while the Ag-In-S QDs display from yellow to dark red color as the Ag to In molar ratio increases (**Figure 3.1a**). The prepared QDs can be well dispersed in DMF solution with obvious Tyndall effect (**Figure 3.1a**). Consistent with these color variation results, the ultraviolet-visible (UV-vis) diffuse reflectance spectrum in **Figure 3.1b** shows that the light absorption ability improves with the increase of Ag to In molar ratio. The bandgaps are calculated according to the Kubelka–Munk function, which are obtained by extrapolating the tangent to the x-axis. As shown in **Figure 3.2**, the bandgaps of QDs show a gradual narrowing from 3.37 eV of In_2S_3 to 2.44 eV of 3Ag-In-S. Such trend is consistent with the theoretical prediction that increasing the Ag/In molar ratio in Ag-In-S structure leads to the decreased bandgap (**Figure 3.1c and d**).

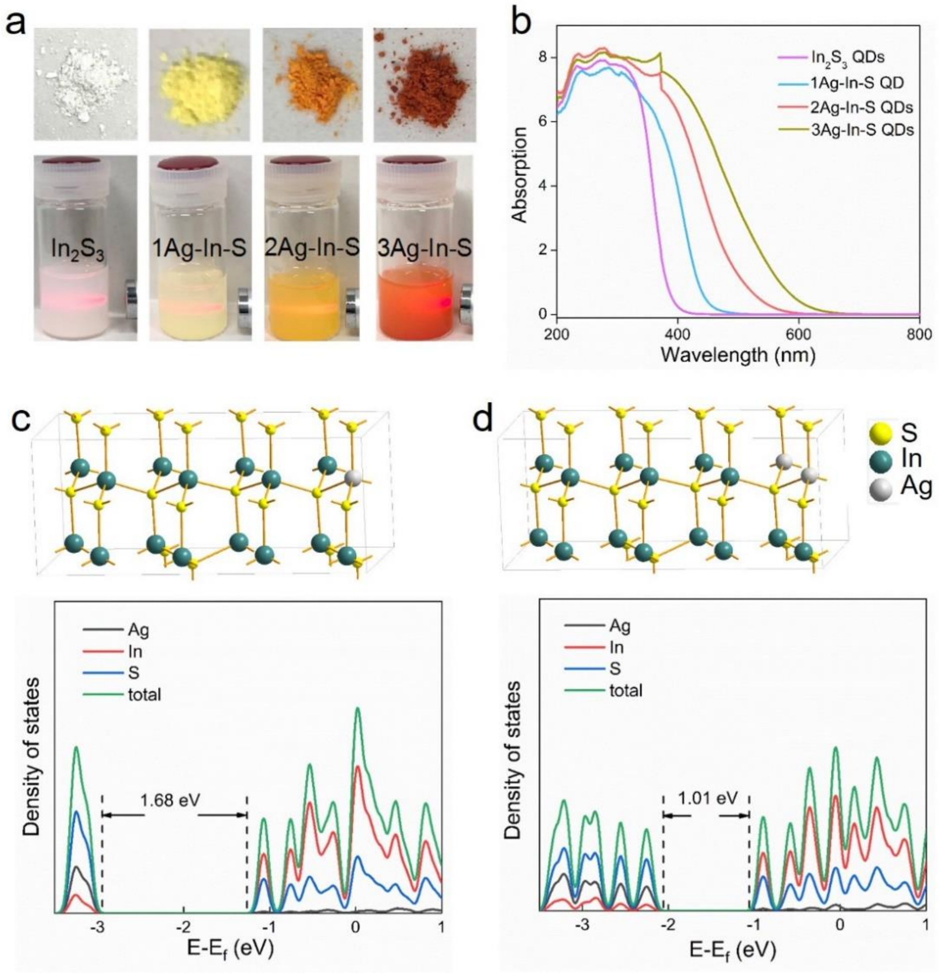

Figure **3.1** (a) Photographs of In_2S_3 QDs and Ag-In-S QDs powder and their Tyndall effect dispersed in DMF; (b) UV-vis absorption spectra of In_2S_3 QDs and Ag-In-S QDs;

Simulation of (c) $AgIn_{15}S_{16}$ and (d) $Ag_2In_{14}S_{16}$ structures and the corresponding calculated density of states.

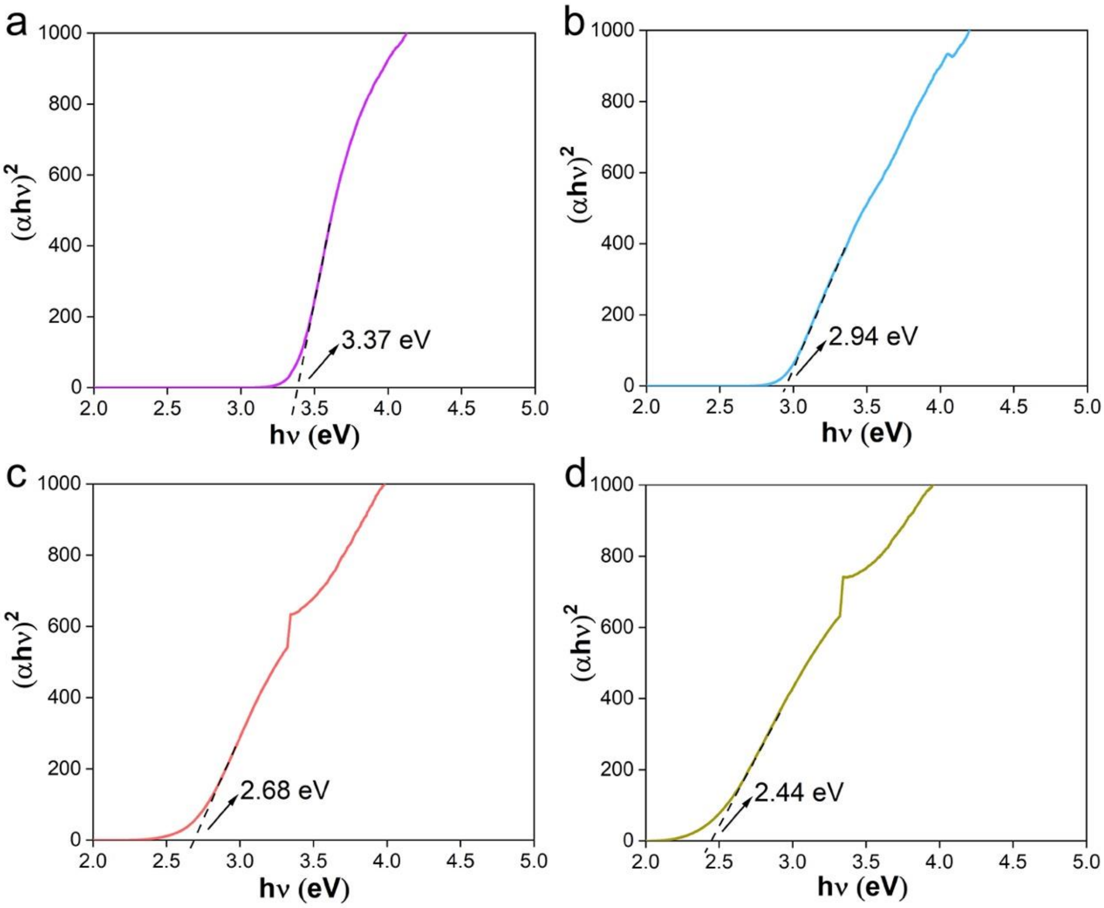

Figure 3.2 Bandgap calculation results of (a) In_2S_3 QDs, (b) 1Ag-In-S, (c) 2Ag-In-S and (d) 3Ag-In-S.

The high-resolution transmission electron microscopy (HRTEM) image of 2Ag-In-S is shown in **Figure 3.3a**, whose particle size is dispersed in the range of 2.7 ~ 4.3 nm. The lattice fringe with interplaner spacing of 0.33 nm can be observed, typical for the (112) facet of tetragonal $AgInS_2$ phase.[22] The corresponding size distribution of 2Ag-In-S is shown in **Figure 3.3b**, which reveals that the average diameter of 2Ag-In-S is 3.56 nm. The energy dispersive X-ray spectroscopy (EDX) of 2Ag-In-S is shown in **Figure 3.4**, which confirms the existence of S, In and Ag elements. The HRTEM images of 1Ag-In-S and 3Ag-In-S, and their corresponding size distributions are shown in **Figure 3.5.** The average diameters of 1Ag-In-S and 3Ag-In-S are 3.66 and 3.54 nm, respectively, which indicates that changing the molar ratio of Ag to In will not significantly change the particle size of the Ag-In-S QDs. **Figure 3.3c** shows the X-ray powder diffraction (XRD) patterns of the In_2S_3 QDs and Ag-In-S QDs. In_2S_3 QDs display two strongly broadened peaks located at 28.1^{o} and 48.5^{o}, which are typical for the (019) and (221) planes of In_2S_3 crystal (ICSD no. 640360), respectively.[21] Ag-In-S QDs exhibit three peaks with 2Θ positions at 27.4, 46.1 and 53.4, ascribed to the (112), (024) and (132) planes, respectively, of the tetragonal $AgInS_2$ crystal (ICSD no. 605413).[21, 22] The chemical states of Ag-In-S QDs are revealed by X-ray photoelectron spectroscopy (XPS). As shown in **Figure 3.3d**, the high-resolution XPS spectrum of Ag 3d reveals a doublet at 373.7 eV and 367.7 eV with the splitting of 6 eV, which is typical for Ag^+.[21] Also, the In 3d spectrum shows two peaks at 452.4 eV and 444.8 eV with the splitting of 7.6 eV, which is typical for In^{3+} (**Figure 3.3e**).[21] The binding energy range of S 2p exhibits two peaks located at 162.7 eV and 161.2 eV, corresponding to S^{2-} (**Figure 3.3f**).[22]

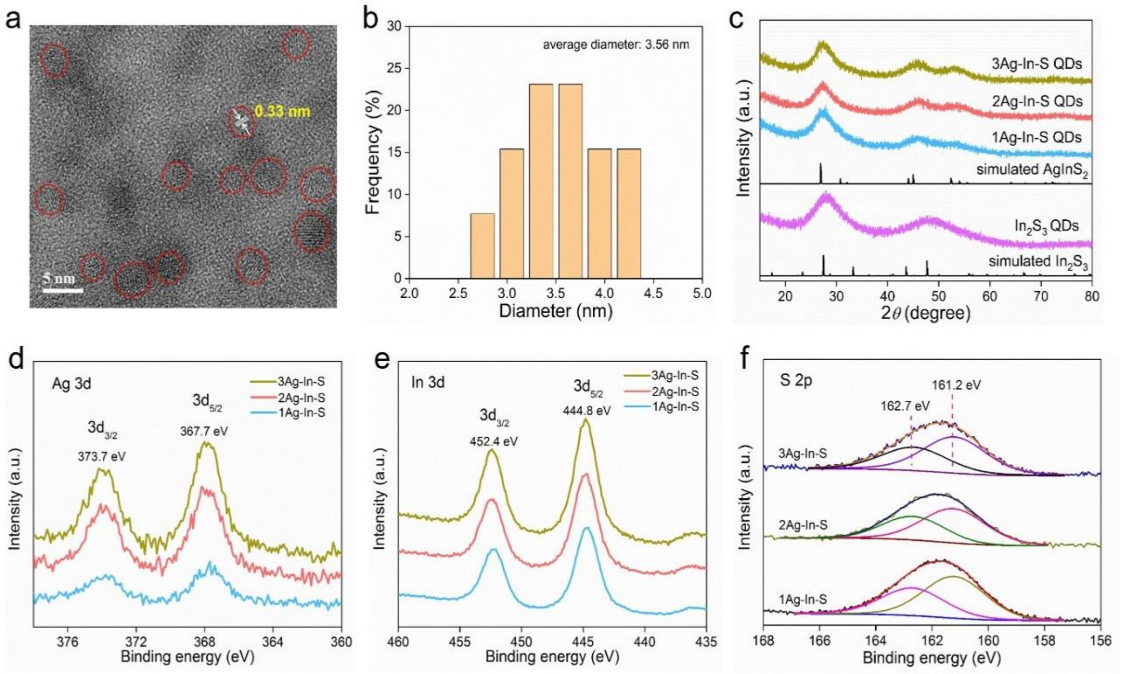

Figure 3.3 (a) HRTEM image of 2Ag-In-S QDs; (b) Size distribution of 2Ag-In-S QDs evaluated from the HRTEM image; (c) XRD patterns of In_2S_3 QDs and Ag-In-S QDs; XPS spectra of (d) Ag 3d, (e) In 3d and (f) S 2p for Ag-In-S QDs.

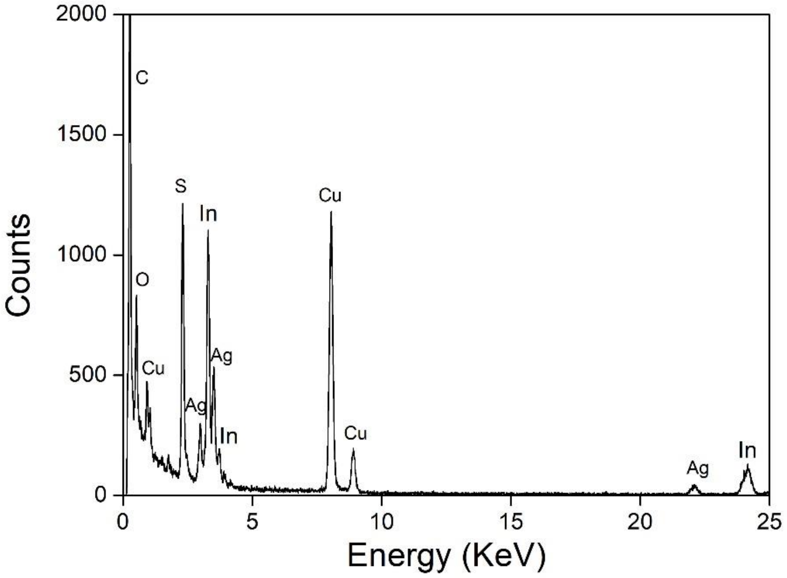

Figure 3.4 EDX of 2Ag-In-S QDs. The C and Cu elements come from the TEM substrate.

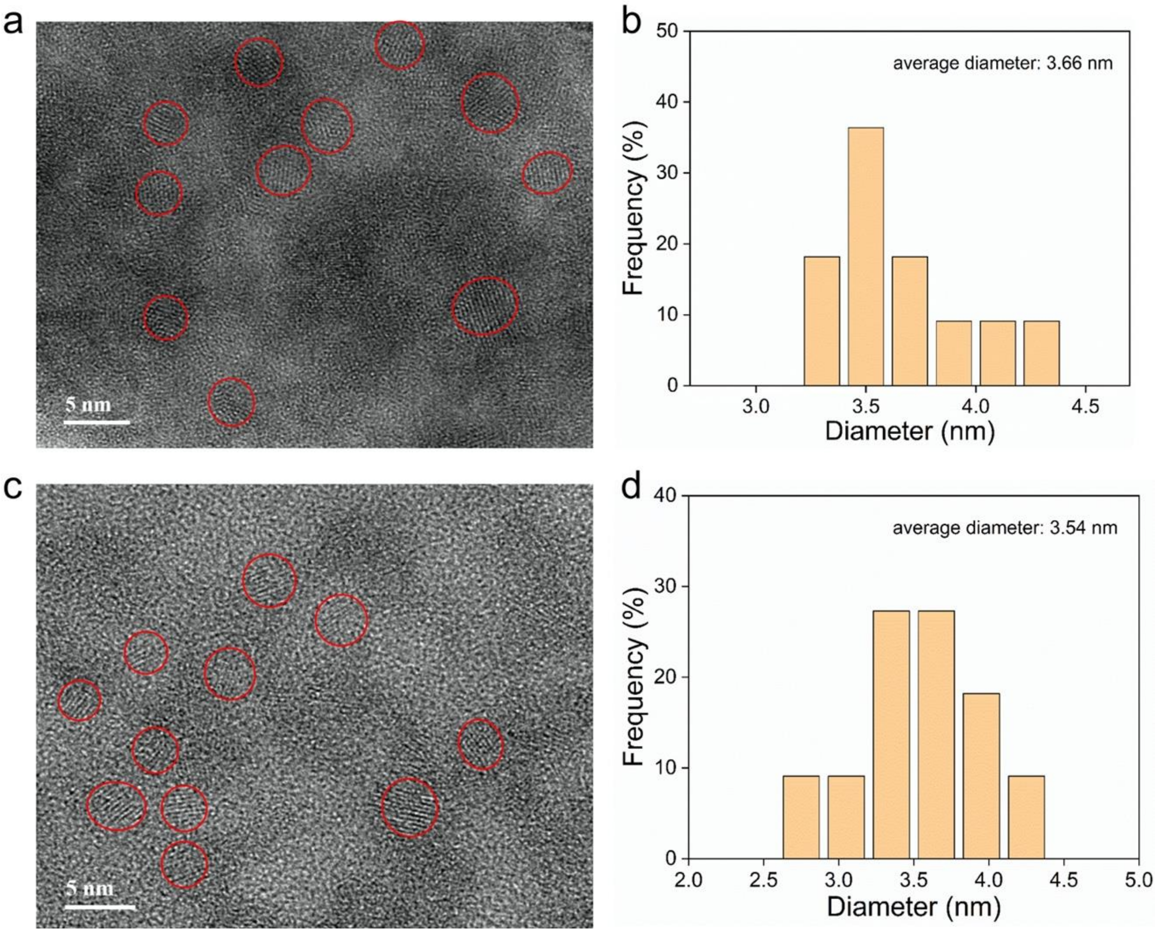

Figure 3.5 HRTEM image of (a) 1Ag-In-S and (b) its corresponding size distribution. HRTEM image of (c) 3Ag-In-S and (d) its corresponding size distribution.

3.3.2 Evaluation of photocatalytic performances

The photocatalytic syngas production reactions of the prepared QDs were carried out in the presence of sacrificial reagent triethanolamine (TEOA) and cocatalyst CoBPY in dimethylformamide (DMF) solvent under visible light irradiation and mild conditions (ambient temperature and 1 bar CO_2). **Figure 3.6** shows the setup of the experiment for photocatalytic reactions. Only the products CO and H_2 were detected in this photocatalytic system, consistent with the previous reported works that were conducted in the liquid-solid photocatalytic reaction systems with TEOA sacrificial agent, CO_2 reactant and CoBPY cocatalyst.[23-27] The photocatalytic reactions were repeated for three times and average gas evolution rates and error bars were shown in **Figure 3.7a** and **3.7b**. **Figure 3.7a** shows the photocatalytic syngas production performances over different samples. The In_2S_3 QDs only produce trace amount of gas products under visible light, mainly due to its limited visible light absorption ability (**Figure 3.1b**). Once the Ag-In-S QDs are employed, the photocatalytic performances are gradually improved (**Figure 3.7a**). It clearly shows that both the activity and the selectivity of photocatalytic syngas production over the Ag-In-S QDs are dependent on the Ag to In molar ratios, with the trend displaying a volcano-shaped curve. In particular, the syngas evolution rate and the selectivity of CO increase with the increasing of Ag to In molar ratios, and the 2Ag-In-S sample displays the highest CO production rate of 9.20 μmol h^{-1} and H_2 production rate of 3.13 μmol h^{-1}, corresponding to the highest CO selectivity of 74.61%, while further increasing the Ag to In molar ratio results in the decreasing of syngas evolution rate and selectivity. The reason for this trend will be discussed later. The photocatalytic CO_2 reduction performnace of 2Ag-In-S QDs is much higher than the $AgInS_2$ particles, demonstrating the superiority of non-stoichiometric Ag-In-S QDs for photocatalytic reaction (**Figure 3.8**).

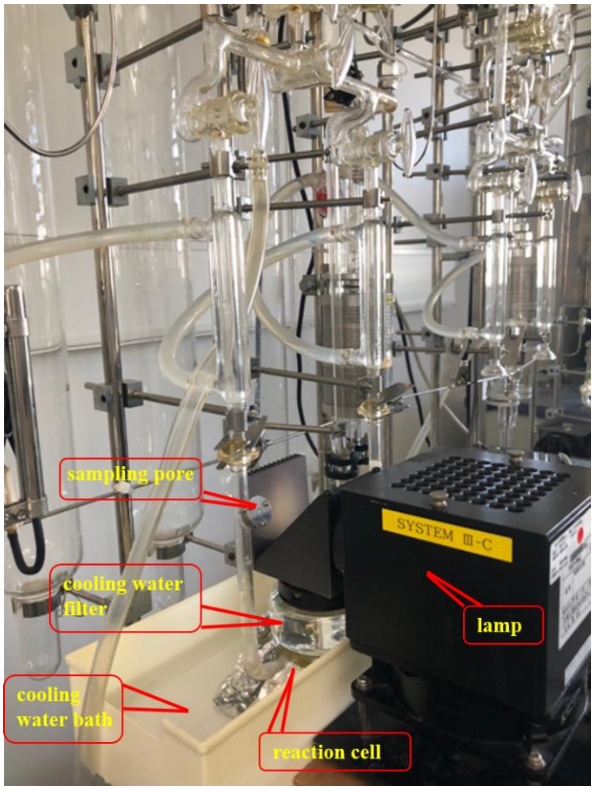

Figure 3.6 The experimental setup for photocatalytic CO_2 reduction.

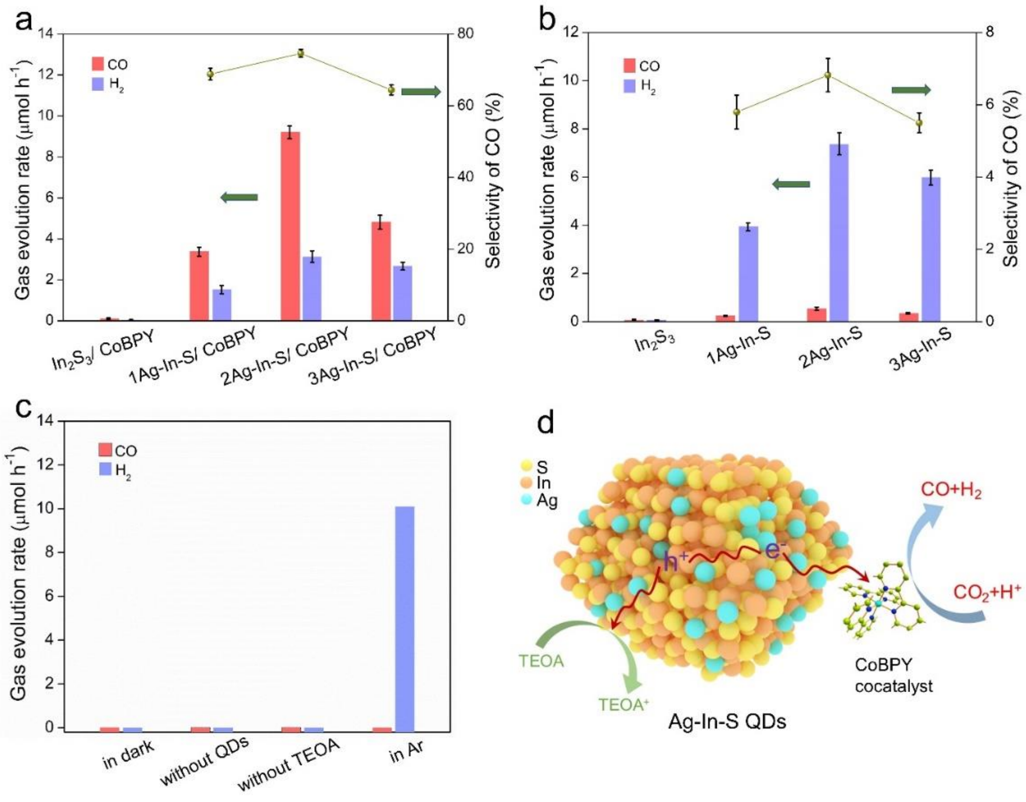

Figure 3.7 (a) Photocatalytic syngas production rates and the selectivity of CO over different QDs in the presence and (b) in the absence of CoBPY cocatalyst; (c)

Photocatalytic syngas production rates over 2Ag-In-S QDs under different conditions; (d) Schematic illustration of photocatalytic CO_2 reduction process over Ag-In-S/ CoBPY system.

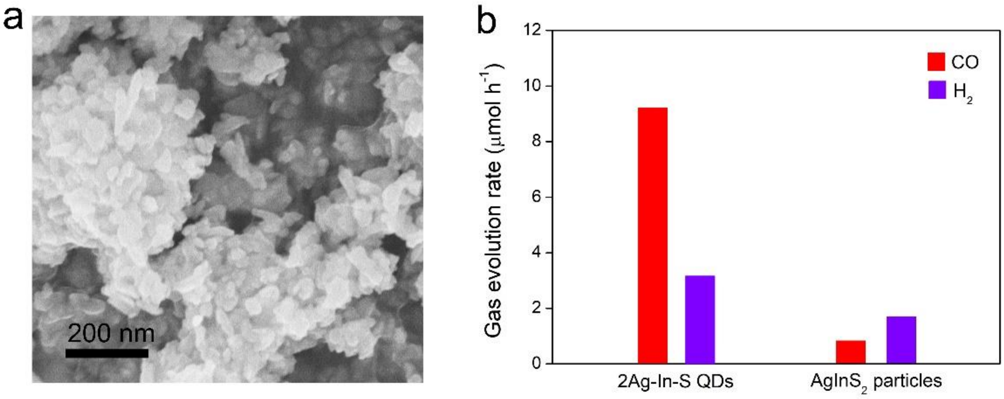

Figure 3.8 (a) SEM image of $AgInS_2$ particles; (b) photocatalytic CO_2 reduction performance comparison of $AgInS_2$ particles and 2Ag-In-S QDs, the photocatalytic reactions were conducted in the presence of CoBPY cocatalyst.

When the photocatalytic reactions were performed in the absence of CoBPY, the CO evolution rates and the selectivities of CO were greatly decreased (**Figure 3.7b**), revealing the significant role of CoBPY as cocatalyst to facilitate the photocatalytic reduction of CO_2 to CO. This phenomenon is highly consistent with previous works in which CoBPY has been demonstrated as an effective cocatalyst in photocatalytic CO_2 reduction reactions.[11, 23-27] The photocatalytic performances were further evaluated under different reaction conditions over 2Ag-In-S/ CoBPY system. No products are generated in the absence of visible light or 2Ag-In-S QDs, indicating the CO is generated *via* a visible-light-driven photocatalytic process over 2Ag-In-S QDs (**Figure 3.7c**, column 1, 2). Moreover, the photocatalytic reaction is also evaluated without TEOA, and no products are detected, suggesting that the TEOA behaves as both the proton source and electron donor (**Figure 3.7c**, column 3). When CO_2 is replaced by Ar, only H_2 evolution is observed, revealing the generated CO originates from CO_2 (**Figure 3.7c**, column 4). On the basis of the above results and previous reported photocatalyst/ CoBPY systems,[27, 28] a tentative reaction mechanism for photocatalytic CO_2 reduction over Ag-In-S/ CoBPY has been proposed, as schematically illustrated in **Figure 3.7d**. Upon visible light irradiation, the electron-hole pairs are generated in Ag-In-S QDs, and the electrons can be transferred to CoBPY cocatalyst to facilitate the CO_2 activation and conversion, and the remained holes are consumed by TEOA. AgInS2 particles were prepared as the control sample, which were obtained according to the reported article (Catalysts 2020, 10, 857). Briefly, 20 ml of 4 mmol AgNO3 was mixed with 20 ml of 4 mmol InCl3, then 20 ml of 8 mmol L-cysteine was slowly added to the mixture. After that the ammonia solution was added to adjust the final pH value of 7. After stirring for 30 min, the obtained slurry was then transferred into Teflon-lined stainless steel autoclave and heated at 160 ^{o}C for 24 h. The AgInS2 particles were finally obtained by centrifugation, washing and drying. The SEM characterization in Figure 3.8a shows the morphology of AgInS2 has the irregular shape with particle size of dozens of nanometers. The photocatalytic CO2 reduction performance of AgInS2 has been evaluated, which is much lower than the Ag-In-S QDs sample, demonstrating the superiority of non-stoichiometric Ag-In-S QDs for photocatalytic reaction.

The time-dependent yield of products over Ag-In-S QDs in the presence of CoBPY cocatalyst are illustrated in **Figure 3.8**, which shows that the generation of CO and H_2 increases almost linearly with reaction time, indicating the high stability of Ag-In-S QDs in photocatalytic CO_2 reduction reactions. To further evaluate the stability, the 2Ag-In-S QDs photocatalyst is repeatedly used to run the photocatalytic CO_2 reduction reaction for four cycles. As displayed in **Figure 3.9a**, no evident deactivation of CO and H_2 evolution rates are found during four cycles test, revealing the high stability of 2Ag-In-S QDs. The wavelength-dependent apparent quantum efficiency (AQE) of syngas production was measured to investigate whether or not the reaction proceeds photocatalytically. The UV-vis absorption spectrum of the 2Ag-In-S sample together with the AQE of syngas production at the different incident light wavelengths are exhibited in **Figure 3.9b**. It indicates that the AQE decreases with the increasing of incident wavelength, with the trend in good agreement with that of the optical absorption spectrum of 2Ag-In-S sample in the visible light region, demonstrating that the syngas production originates from the photocatalytic reaction. Noting that the measured AQE at the monochromatic light of 400 nm reaches as high as 3.65%. The obtained photocatalytic syngas production performance over 2Ag-In-S QDs exceeds that of some reported photocatalysts (**Table 3.1**).[17, 29-35] The effects of the solvent on the photocatalytic syngas production activity were tested. As shown in **Figure 3.9c**, the highest syngas evolution rate is achieved in the aprotic

DMF solvent, mainly due to its excellent solubility of CO_2 gas.[23] However, the photocatalytic activity is significantly inhibited by using H_2O as solvent, largely due to the fact that H_2O possesses a weak chemical affinity toward CO_2 molecules.[23] The evidence of the carbon source of the CO product was provided by $^{13}CO_2$ isotopic experiment. The measurement and analysis of the generated CO was carried out in gas chromatogram (GC) and mass spectra (MS). As exhibited in **Figure 3.9d**, the CO product appears at the peak of the retention time of 6.1 min, while other two signals at the retention time before CO are demonstrated to be O_2 and N_2, originating from the air leaking during the sampling process.[36] The analysis of the CO peak in MS reveals the m/z= 29, ascribed to the ^{13}CO. In contrast, when $^{12}CO_2$ is used in the photocatalytic system, only ^{12}CO is produced (**Figure 3.10**). These results definitely demonstrate that the CO originates from the photocatalytic reduction of CO_2.

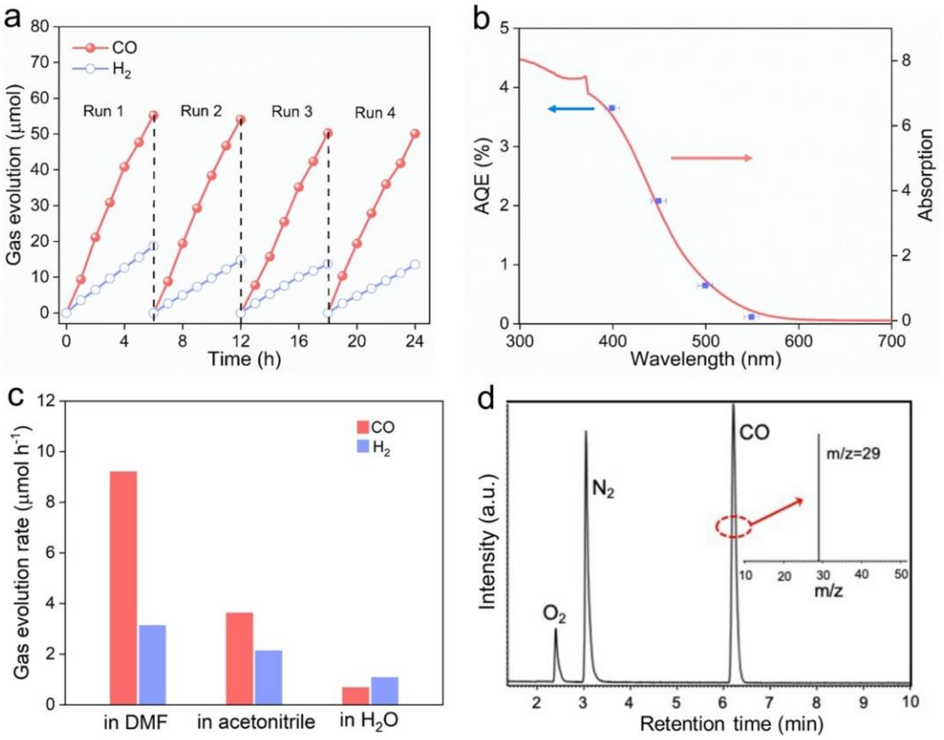

Figure 3.9 (a) Time-dependent and stability test of syngas production over 2Ag-In-S QDs in the presence of CoBPY as cocatalyst; (b) UV-vis absorption spectrum and wavelength-dependent AQE of 2Ag-In-S QDs; (c) Photocatalytic syngas production rates over 2Ag-In-S/ CoBPY in different reaction solution; (d) GC-MS of CO obtained from photocatalytic reduction of $^{13}CO_2$ over 2Ag-In-S QDs.

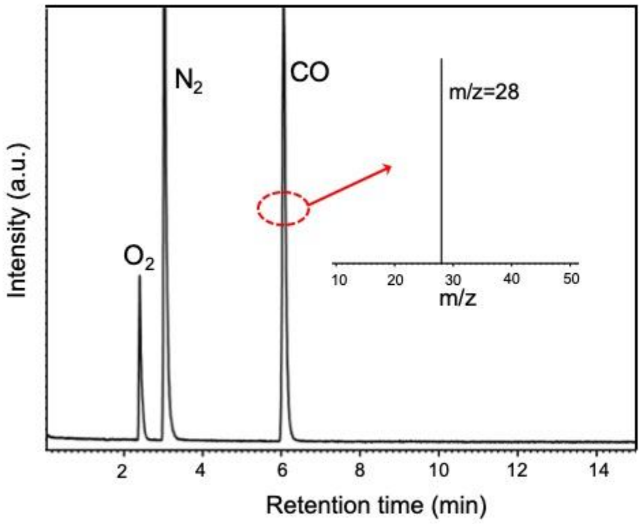

Figure 3.10 GC-MS of CO obtained from photocatalytic reduction of $^{12}CO_2$ over 2Ag-In-S QDs.

Table 3.1 Comparison of photocatalytic CO and H_2 evolution rates from CO_2 over different photocatalysts.

Photocatalysts/ cocatalyst	photocatalytic activity	references
Ag-In-S QDs/ $Co(bpy)_3^{2+}$	CO evolution rate: 9.20 μmol h^{-1} H_2 evolution rate: 3.13 μmol h^{-1}	This work
$g\text{-}C_3N_4$–$CsPbBr_3$ QDs	CO evolution rate: 1.19 μmol h^{-1}	Angew. Chem. Int. Ed. 2018, 57, 13570 –13574
CdS QDs/ $[Ni(terpyS)_2]^{2+}$	CO evolution rate: 0.415 μmol h^{-1} H_2 evolution rate: 0.312 μmol h^{-1}	J. Am. Chem. Soc. 2017, 139, 7217−7223
ZnSe QDs/ NiCycP	CO evolution rate: ca. 0.25 μmol h^{-1} H_2 evolution rate: ca. 0.55 μmol h^{-1}	Chem. Sci. 2018, 9, 2501–2509
CdSe QDs	CO evolution rate: 1.81 μmol h^{-1} H_2 evolution rate: 0.10 μmol h^{-1}	ChemSusChem. 2019, 12, 4617 –4622
CdS QDs/ Co_2L	CO evolution rate: 0.288 μmol h^{-1} H_2 evolution rate: 0.007 μmol h^{-1} CH_4 evolution rate: 0.008 μmol h^{-1}	ACS Catal. 2018, 8, 11815–11821
$CsPbBr_3$ QDs/ GO	CO evolution rate: 0.02 μmol h^{-1} H_2 evolution rate: trace CH_4 evolution rate: 0.01 μmol h^{-1}	J. Am. Chem. Soc. 2017, 139, 5660−5663
In_2S_3−$CdIn_2S_4$/ $Co(bpy)_3^{2+}$	CO evolution rate: 3.3 μmol h^{-1} H_2 evolution rate: 1.04 μmol h^{-1}	J. Am. Chem. Soc. 2017, 139, 17305−17308
Helical $g\text{-}C_3N_4$/ $Co(bpy)_3^{2+}$	CO evolution rate: 8.9 μmol h^{-1} H_2 evolution rate: 0.3 μmol h^{-1}	Angew. Chem. 2014, 126, 12120 –12124

In this work, the introduction of CoBPY cocatalyst into the system not only improves the photocatalytic CO evolution performance, suppresses the H_2 evolution, but also enhances the stability of Ag-In-S QDs. The colors of the reaction solutions turn dark after photocatalytic reaction in the absence of CoBPY cocatalyst, while they remain almost unchanged when the CoBPY cocatalyst is introduced (**Figure 3.11**). The change of color results from the structural destruction of Ag-In-S QDs, as revealed by the XRD patterns. As shown in **Figure 3.11**, the crystal structures of the used Ag-In-S QDs in the presence of CoBPY cocatalyst after photocatalytic reactions remain almost unchanged, however, the destruction of crystal structures can be observed in the absence of CoBPY cocatalyst. It clearly demonstrates that the introduction of CoBPY cocatalyst in the reaction solution significantly enhances the stability of Ag-In-S QDs. The Ag^+ in Ag-In-S QDs could be easily reduced to Ag^0 by the photogenerated electrons (**Figure 3.11**). However, when the CoBPY cocatalyst is introduced into the reaction solution, the photogenerated electrons from Ag-In-S QDs will be captured by CoBPY cocatalyst, which protects the Ag^+ of Ag-In-S QDs from reduction.

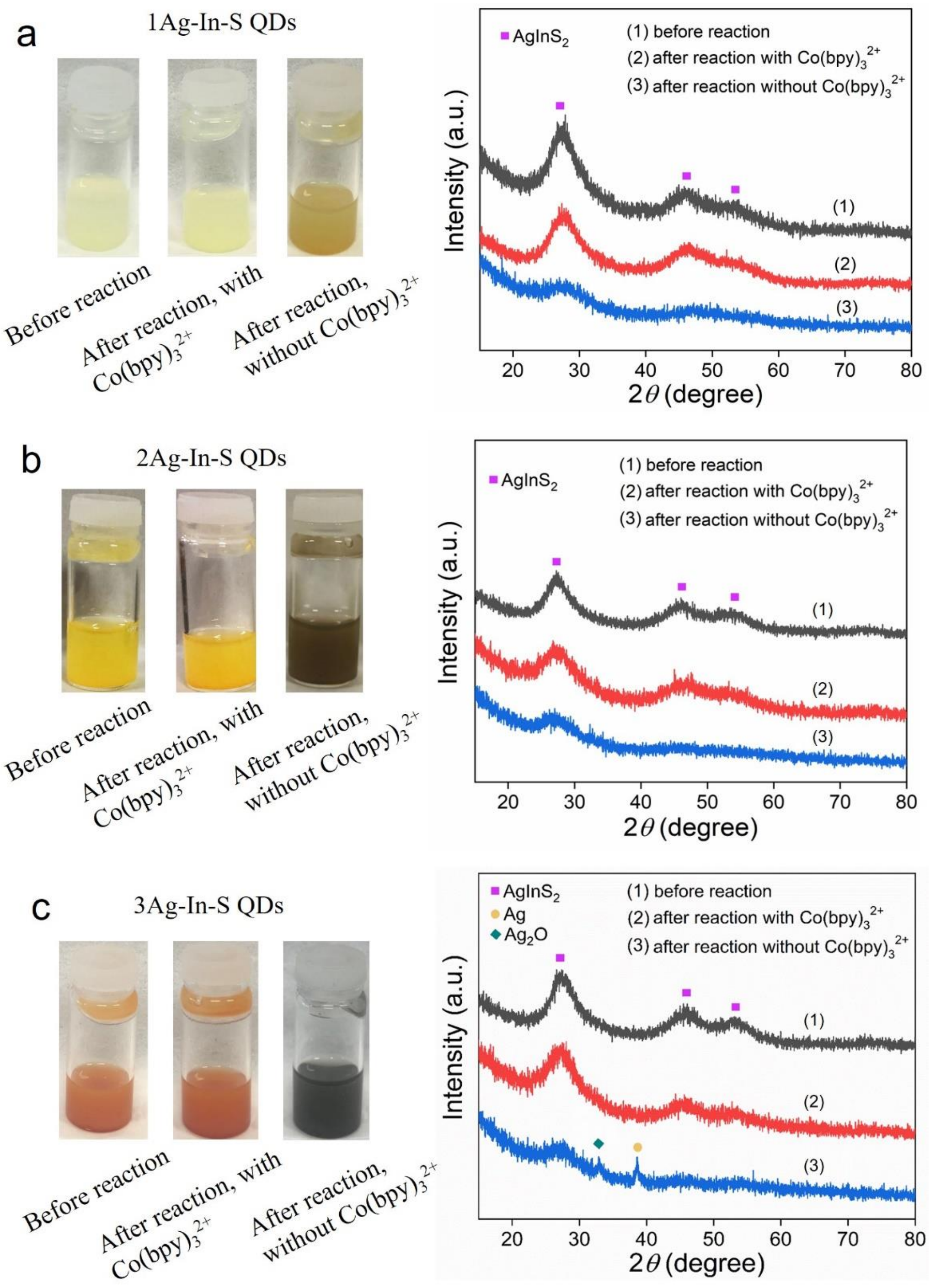

Figure 3.11 Photographs of Ag-In-S QDs dispersed in DMF solution and the XRD patterns of Ag-In-S QDs before and after photocatalytic CO_2 reduction reaction for 6 hours. (a) 1Ag-In-S QDs, (b) 2Ag-In-S QDs, (c) 3Ag-In-S QDs.

3.3.3 Clarification of mechanism

The above results have shown that the activity and selectivity of photocatalytic CO_2 reduction are dependent on the Ag to In molar ratios in Ag-In-S QDs. We are now in the position to reveal the mechanism behind it. Noting that the band positions, light absorption ability and charge carrier lifetime of photocatalysts exert great effect on the photocatalytic efficiency.[37] Increasing the Ag to In molar ratios in Ag-In-S QDs leads to the enhancement of the light absorption ability (**Figure 3.11b**), which certainly contributes to the improvement of photocatalytic performances. The charge carrier dynamics of Ag-In-S QDs was revealed by time-resolved photoluminescence (PL) decay measurements (**Figure 3.12a**). The corresponding lifetime fitted by the bi-exponential functions are shown in **Table 3.2**. An increase of Ag to In molar ratio in Ag-In-S QDs results in a slower of the PL decay dynamics and an increase of the average lifetime (**Figure 3.12a**). Such behavior can be explained by the reason that the structural defects gradually increased with decreasing the Ag to In ratio in non-stoichiometric Ag-In-S QDs, resulting in fast decay of charge carriers.[22] The longer lifetime of charge carriers can improve the probability of their involvement in photoreactions, which contributes to the improvement of photocatalytic syngas production rates.

Table 3.2 Fitting data of time-resolved PL decays over Ag-In-S QDs.

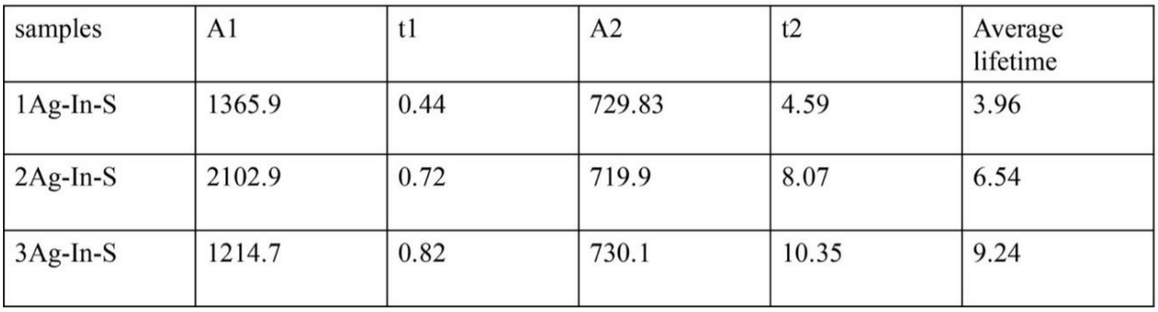

samples	A1	t1	A2	t2	Average lifetime
1Ag-In-S	1365.9	0.44	729.83	4.59	3.96
2Ag-In-S	2102.9	0.72	719.9	8.07	6.54
3Ag-In-S	1214.7	0.82	730.1	10.35	9.24

The photocatalytic performance not only depends on the lifetime of charge carriers, but also depends on the reduction potential of electrons. The band positions of Ag-In-S QDs are estimated by Mott-Schottky test. As shown in **Figure 3.13**, the flat-band (FB) potentials for 1Ag-In-S, 2Ag-In-S and 3Ag-In-S are -0.83 V vs. NHE, -0.66 V vs. NHE and -0.51 V vs. NHE, respectively. In consideration of the small difference between the lowest conduction band (CB) edge and the value of FB potential for *n*-type semiconductor,[38] and in combination with the bandgap results above, the estimated band positions of the Ag-In-S QDs samples are shown in **Figure 3.12b**. The CB positions of all the Ag-In-S QDs can drive the H_2 evolution and CO_2 reduction reactions. It can be seen that the band positions of Ag-In-S QDs are significantly affected by the Ag to In molar ratio, and increasing the Ag to In molar ratio leads to the downshift of CB position. The downshift of CB position could decrease the reduction ability of electrons generated in the Ag-In-S QDs, which exerts negative effect on the photocatalytic performance. Therefore, along with the increasing of Ag to In molar ratios in Ag-In-S QDs, the enhanced light absorption ability, the increased lifetime of photogenerated charge carriers and the decreased reduction ability of electrons play competitive roles in the photocatalytic syngas production reaction, and the optimized syngas evolution rate is achieved over 2Ag-In-S with the Ag to In molar ratio of 0.154:1.

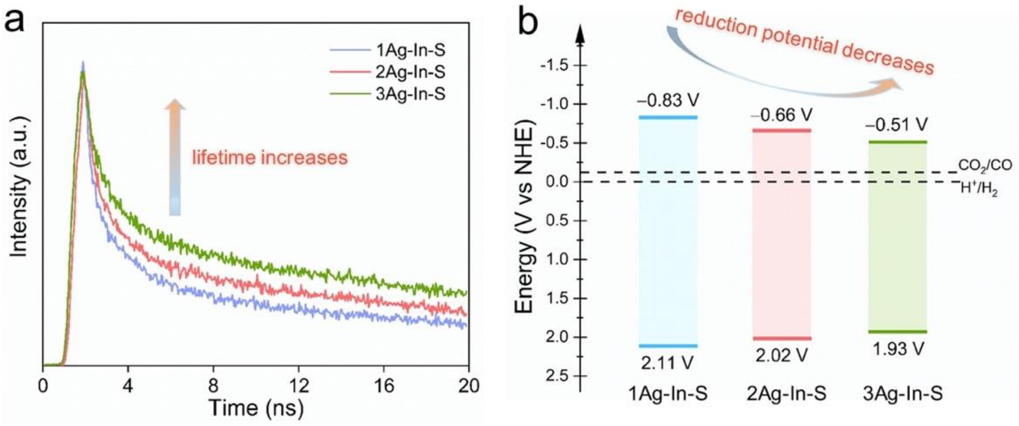

Figure 3.12 (a) Time-resolved PL decay spectra of Ag-In-S QDs; (b) Electronic band structures. of Ag-In-S QDs.

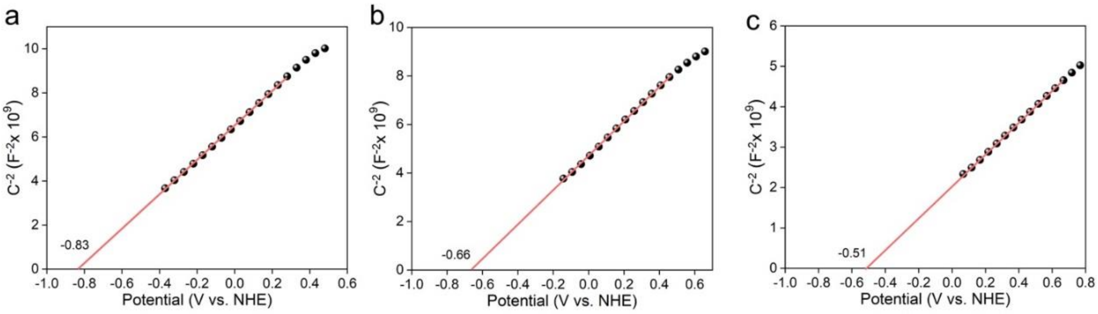

Figure 3.13 Mott-Schottky plots of (a) 1Ag-In-S QDs, (b) 2Ag-In-S QDs and (c) 3Ag-In-S QDs.

The selectivity of photocatalytic CO evolution is also dependent on the Ag to In molar ratios in the Ag-In-S QDs. As shown in **Figure 3.7a**, the 2Ag-In-S sample shows the higher selectivity of CO than the 1Ag-In-S sample, probably due to the fact that the increased lifetime of photogenerated electrons in the 2Ag-In-S sample contributes to the multi-electrons involved reduction of CO_2 to CO. However, when further increasing the Ag to In molar ratio in Ag-In-S, the effect of the reduction potential of electrons becomes the dominant role in the photocatalytic syngas production reaction. Since the redox potential of CO_2/CO is higher than that of H^+/H_2 (**Figure 3.12b**), the H_2 evolution becomes more competitive than CO evolution in the 3Ag-In-S sample when comparing with the 2Ag-In-S sample, and finally resulting in the deceased selectivity of CO.

3.4 Conclusions

In summary, this work provides a strong evidence that non-stoichiometric Ag-In-S QDs can be used as photocatalysts for efficient and stable visible-light-driven photocatalytic syngas production from CO_2 conversion in the presence of CoBPY as a molecular cocatalyst. The introduction of CoBPY into the reaction system not only promotes the conversion of CO_2 to CO reaction but also improves the photo-stability of Ag-In-S QDs. The photocatalytic syngas production rates and the selectivity of CO are strongly dependent on the Ag to In molar ratios in Ag-In-S QDs, and the 2Ag-In-S QDs sample with the Ag to In molar ratio of 0.154:1 exhibits the highest CO production rate of 9.20 μmol h^{-1} and H_2 production rate of 3.13 μmol h^{-1}, which outperform most of the reported QDs based photocatalysts. The mechanism investigation reveals that the increasing of Ag to In molar ratios in Ag-In-S QDs leads to the enhanced light absorption ability, the increased lifetime of photogenerated charge carriers and the decreased reduction potential of electrons, which play competitive roles in the photocatalytic syngas production reaction.

References

[1] H. Zhang, J. Ming, J. Zhao, Q. Gu, C. Xu, Z. Ding, R. Yuan, Z. Zhang, H. Lin, X. Wang, J. Long, High-Rate, Tunable Syngas Production with Artificial Photosynthetic Cells, Angew. Chem. Int. Ed. 58 (2019) 7718-7722.

[2] J. R. Rostrup-Nielsen, Syngas in Perspective, Catal. Today 71 (2002) 243-247.

[3] M. Liu, Y.-F. Mu, S. Yao, S. Guo, X.-W. Guo, Z.-M. Zhang, T.-B. Lu, Photosensitizing Single-Site Metal−Organic Framework Enabling Visible-Light-Driven CO_2 Reduction for Syngas Production, Appl. Catal. B: Environ. 245 (2019) 496-501.

[4] A. Li, T. Wang, X. Chang, Z.-J. Zhao, C. Li, Z. Huang, P. Yang, G. Zhou, J. Gong, Tunable Syngas Production from Photocatalytic CO_2 Reduction with Mitigated Charge Recombination Driven by Spatially Separated Cocatalysts, Chem. Sci. 9 (2018) 5334-5340.

[5] X. Deng, J. Albero, L. Xu, H. Garcia, Z. Li, Construction of a Stable Ru-Re Hybrid System Based on Multifunctional MOF-253 for Efficient Photocatalytic CO_2 Reduction, Inorg. Chem. 57 (2018) 8276-8286.

[6] H. Takeda, Y. Monma, H. Sugiyama, H. Uekusa, O. Ishitani, Development of Visible-Light Driven Cu(I) Complex Photosensitizers for Photocatalytic CO_2 Reduction, Front. Chem. 7 (2019) 418.

[7] Y. Kuramochi, O. Ishitani, Iridium(III) 1-Phenylisoquinoline Complexes as a Photosensitizer for Photocatalytic CO_2 Reduction: A Mixed System with a Re(I) Catalyst and a Supramolecular Photocatalyst, Inorg. Chem. 55 (2016) 5702-5709.

[8] J.-S. Lee, D. I. Won, W. J. Jung, H. J. Son, C. Pac, S. O. Kang, Widely Controllable Syngas Production by a Dye-Sensitized TiO_2 Hybrid System with Re^I and Co^{III} Catalysts under Visible-Light Irradiation, Angew. Chem. Int. Ed. 56 (2017) 976-980.

[9] X. Jiao, K. Zheng, L. Liang, X. Li, Y. Sun, Y. Xie, Fundamentals and Challenges of Ultrathin 2D Photocatalysts in Boosting CO_2 Photoreduction, Chem. Soc. Rev. 49 (2020) 6592-6604.

[10] C. Bie, B. Zhu, F. Xu, L. Zhang, J. Yu, In Situ Grown Monolayer N-Doped Graphene on CdS Hollow Spheres with Seamless Contact for Photocatalytic CO_2 Reduction, Adv. Mater. 31 (2019) 1902868.

[11] S. Wang, B. Y. Guan, X. W. D. Lou, Construction of $ZnIn_2S_4$-In_2O_3 Hierarchical Tubular Heterostructures for Efficient CO_2 Photoreduction, J. Am. Chem. Soc. 140 (2018) 5037-5040.

[12] J. Wang, S. Lin, N. Tian, T. Ma, Y. Zhang, H. Huang, Nanostructured Metal Sulfides: Classification, Modification Strategy, and Solar-Driven CO_2 Reduction Application, Adv. Funct. Mater. 31 (2021) 2008008.

[13] H. L. Wu, X. B. Li, C. H. Tung, L.-Z. Wu, Semiconductor Quantum Dots: An Emerging Candidate for CO_2 Photoreduction, Adv. Mater. 31 (2019) 1900709.

[14] S. Lian, M. S. Kodaimati, D. S. Dolzhnikov, R. Calzada, E. A. Weiss, Powering a CO_2 Reduction Catalyst with Visible Light through Multiple Sub-Picosecond Electron Transfers from a Quantum Dot, J. Am. Chem. Soc. 139 (2017) 8931-8938.

[15] A. Li, T. Wang, C. Li, Z. Huang, Z. Luo, J. Gong, Adjusting the Reduction Potential of Electrons by Quantum Confinement for Selective Photoreduction of CO_2 to Methanol, Angew. Chem. Int. Ed. 58 (2019) 3804-3808.

[16] J. Wang, T. Xia, L. Wang, X. Zheng, Z. Qi, C. Gao, J. Zhu, Z. Li, H. Xu, Y. Xiong, Enabling Visible-Light-Driven Selective CO_2 Reduction by Doping Quantum Dots: Trapping Electrons and Suppressing H_2 Evolution, Angew. Chem. Int. Ed. 57 (2018) 16447-16451.

[17] W. Xia, J. Wu, J. C. Hu, S. Sun, M. D. Li, H. Liu, M. Lan, F. Wang, Highly Efficient Photocatalytic Conversion of CO_2 to CO Catalyzed by Surface-Ligand-Removed and Cd-Rich CdSe Quantum Dots, ChemSusChem, 12 (2019) 4617-4622.

[18] F. Xu, K. Meng, B. Cheng, S. Wang, J. Xu, J. Yu, Unique S-Scheme Heterojunctions in Self-Assembled TiO_2/$CsPbBr_3$ Hybrids for CO_2 Photoreduction, Nat. Commun. 11 (2020) 4613.

[19] L. Y. Wu, Y. F. Mu, X. X. Guo, W. Zhang, Z. M. Zhang, M. Zhang, T. B. Lu, Encapsulating Perovskite Quantum Dots in Iron-Based Metal-Organic Frameworks (MOFs) for Efficient Photocatalytic CO_2 Reduction, Angew. Chem. Int. Ed. 58 (2019) 9491-9495.

[20] Z. Zhu, X. Li, Y. Qu, F. Zhou, Z. Wang, W. Wang, C. Zhao, H. Wang, L. Li, Y. Yao, Q. Zhang, Y. Wu, A Hierarchical Heterostructure of CdS QDs Confined on 3D $ZnIn_2S_4$ with Boosted Charge Transfer for Photocatalytic CO_2 Reduction, Nano Res. 14 (2020) 81-90.

[21] A. Raevskaya, V. Lesnyak, D. Haubold, V. Dzhagan, O. Stroyuk, N. Gaponik, D. R. T. Zahn, A. Eychmüller, A Fine Size Selection of Brightly Luminescent Water-Soluble Ag-In-S and Ag-In-S/ZnS Quantum Dots, J. Phys. Chem. C 121 (2017) 9032-9042.

[22] J. Du, S. Ma, H. Liu, H. Fu, L. Li, Z. Li, Y. Li, J. Zhou, Uncovering the Mechanism of Novel $AgInS_2$ Nanosheets/TiO_2 Nanobelts Composites for Photocatalytic Remediation of Combined Pollution, Appl. Catal. B: Environ. 259 (2019) 118062.

[23] L. Shi, X. Ren, Q. Wang, W. Zhou, J. Ye, Tridecaboron Diphosphide: a New Infrared Light Active Photocatalyst for Efficient CO_2 Photoreduction under Mild Reaction Conditions, J. Mater. Chem. A 9 (2021) 2421-2428.

[24] J. Qin, S. Wang, H. Ren, Y. Hou, X. Wang, Photocatalytic Reduction of CO_2 by Graphitic Carbon Nitride Polymers Derived from Urea and Barbituric Acid, Appl. Catal. B: Environ. 179 (2015) 1-8.

[25] P. Yang, H. Zhuzhang, R. Wang, W. Lin, X. Wang, Carbon Vacancies in a Melon Polymeric Matrix Promote Photocatalytic Carbon Dioxide Conversion, Angew. Chem. Int. Ed. 58 (2019) 1134-1137.

[26] P. Zhang, S. Wang, B. Y. Guan, X. W. Lou, Fabrication of CdS Hierarchical Multi-Cavity Hollow Particles for Efficient Visible Light CO_2 Reduction, Energy Environ. Sci. 12 (2019) 164-168.

[27] S. Wang, X. Wang, Photocatalytic CO_2 Reduction by CdS Promoted with a Zeolitic Imidazolate Framework, Appl. Catal. B: Environ. 162 (2015) 494-500.

[28] S. Wang, X. Hai, X. Ding, S. Jin, Y. Xiang, P. Wang, B. Jiang, F. Ichihara, M. Oshikiri, X. Meng, Y. Li, W. Matsuda, J. Ma, S. Seki, X. Wang, H. Huang, Y. Wada, H. Chen, J. Ye, Intermolecular Cascaded π-Conjugation Channels for Electron Delivery Powering CO_2 Photoreduction, Nat. Commun. 11 (2020) 1149.

[29] M. Ou, W. Tu, S. Yin, W. Xing, S. Wu, H. Wang, S. Wan, Q. Zhong, R. Xu, Amino-Assisted Anchoring of $CsPbBr_3$ Perovskite Quantum Dots on Porous g-C_3N_4 for Enhanced Photocatalytic CO_2 Reduction, Angew. Chem. Int. Ed. 57 (2018) 13570-13574.

[30] M. F. Kuehnel, K. L. Orchard, K. E. Dalle, E. Reisner, Selective Photocatalytic CO_2 Reduction in Water through Anchoring of a Molecular Ni Catalyst on CdS Nanocrystals, J. Am. Chem. Soc. 139 (2017) 7217-7223.

[31] M. F. Kuehnel, C. D. Sahm, G. Neri, J. R. Lee, Katherine L. Orchard, A. J. Cowan, E. Reisner, ZnSe Quantum Dots Modified with a Ni(cyclam) Catalyst for Efficient Visible-Light Driven CO_2 Reduction in Water, Chem. Sci. 9 (2018) 2501-2509.

[32] Q.-Q. Bi, J.-W. Wang, J.-X. Lv, J. Wang, W. Zhang, T.-B. Lu, Selective Photocatalytic CO_2 Reduction in Water by Electrostatic Assembly of CdS Nanocrystals with a Dinuclear Cobalt Catalyst, ACS Catal. 8 (2018) 11815-11821.

[33] Y.-F. Xu, M.-Z. Yang, B.-X. Chen, X.-D. Wang, H.-Y. Chen, D.-B. Kuang, C.-Y. Su, A $CsPbBr_3$ Perovskite Quantum Dot/Graphene Oxide Composite for Photocatalytic CO_2 Reduction, J. Am. Chem. Soc. 139 (2017) 5660-5663.

[34] S. Wang, B. Y. Guan, Y. Lu, X. W. D. Lou, Formation of Hierarchical In_2S_3-$CdIn_2S_4$ Heterostructured Nanotubes for Efficient and Stable Visible Light CO_2 Reduction, J. Am. Chem. Soc. 139 (2017) 17305-17308.

[35] Y. Zheng, L. Lin, X. Ye, F. Guo, X. Wang, Helical Graphitic Carbon Nitrides with Photocatalytic and Optical Activities, Angew. Chem. Int. Ed. 53 (2014) 11926-11930.

[36] L. Shi, P. Wang, Q. Wang, X. Ren, F. Ichihara, W. Zhou, H. Zhang, Y. Izumi, B. Cao, S. Wang, H. Chen, J. Ye, Efficient Photocatalytic CO_2 Reduction Mediated by Transitional Metal Borides: Metal Site-Dependent Activity and Selectivity, J. Mater. Chem. A 8 (2020) 21833-21841.

[37] P. Niu, L. Zhang, G. Liu, H.-M. Cheng, Graphene-Like Carbon Nitride Nanosheets for Improved Photocatalytic Activities, Adv. Funct. Mater. 22 (2012) 4763-4770.

[38] S. Yang, Y. Gong, J. Zhang, L. Zhan, L. Ma, Z. Fang, R. Vajtai, X. Wang, P. M. Ajayan, Exfoliated Graphitic Carbon Nitride Nanosheets as Efficient Catalysts for Hydrogen Evolution Under Visible Light, Adv. Mater. 25 (2013) 2452-2456.

Chapter 4 Construction of surface vacancies on colloid CdS_xSe_{1-x} quantum dots for efficient photocatalytic CO_2 reduction

4.1 Introduction

In recent years, carbon capture and storage have attracted worldwide attention, and various technologies have been used to decrease the concentration of CO_2 in the environment. The photocatalytic reduction of CO_2 into value-added chemicals by solar energy has emerged as a crucial strategy to address the greenhouse effect and energy crisis. [1-8] In the past decades, most investigations are focusing on the design and modification of novel photocatalysts to optimize catalytic reaction kinetics pathway for improving the photocatalytic activity and selectivity. However, CO_2 is a very stable molecular, and thus CO_2 reduction needs high energy to overcome the stable state under normal conditions. Meanwhile, hydrogen evolution reaction as the main competitive reaction also seriously affects the selectivity of CO_2 reduction.[9] Previous investigations indicate the energy barrier of COOH* generation and dissociation are key steps of CO_2 reduction which highly correlated with the surface active sites. Therefore, adaptive strategies are needed to be developed to construct and modify the active sites on catalyst surface for achieving efficient photocatalytic CO_2 reduction.

Reducing the size of photocatalysts could not only increase the surface area to expose more active sites but also reduce the transfer distance of excited electrons to the catalyst surface and inhibit the photogenerated electron-hole recombination. As a result, the photocatalysts with smaller size usually exhibit better performance than those of bulk photocatalysts. In this consideration, semiconductor quantum dots (QDs) whose scales are smaller than the Bohr radius, are regarded as promising photocatalysts for CO_2 reduction due to unique characteristics such as high surface area-to-volume ratios, abundant surface-active sites, and short charge transfer lengths, which enable them great potential for CO_2 adsorption and activation. [10-19] Among various QDs, IIB-VIA (CdS, CdSe, ZnS, and etc.) quantum dots are widely investigated for photocatalytic CO_2 reduction. Sahm et al. reported In-modified ZnSe QDs as photocatalyst for CO_2 reduction. The as-prepared In-modified ZnSe QDs showed up to 2.4 $mmol_{CO}\ g_{ZnSe}^{-1}$ ($TON_{QD} > 370$) after 10 h of visible light irradiation without any transition metal based cocatalyst. As typical IIB-VIA QDs, CdS and CdSe QDs have been investigated as photocatalysts in H_2 generation reactions and showed good performance. However, both of them have obvious drawbacks in the application of photocatalytic CO_2 reduction. For example, CdS quantum dots have relatively good light absorption, but their active sites for CO_2 reduction are limited. As a result, CdS quantum dots are generally used as light absorbers coupling with co-catalysts for CO_2 reduction. CdSe quantum dots, on the other hand, have better catalytic performance in photocatalytic CO_2 reduction, but a fast electron-hole combination rate due to its narrow band gap. [20-25] To address their drawbacks, construction of CdS_xSe_{1-x} solid solution QDs is a promising strategy, because many studies have reported that IIB-VIA solid solutions often exhibit better performance than the original materials. However. there are still few studies on CdS_xSe_{1-x} QDs as photocatalysts for CO_2 reduction, which limits the in-depth understanding of IIB-VIA solid solution QDs for CO_2 reduction. Accordingly, we expect that CdS_xSe_{1-x} QDs could be a promising photocatalyst for CO_2 reduction.

Moreover, the surface defects engineering can be applied for modification of photocatalyst to enhance the photocatalytic performance. [26-30] For example, acid solution etching can endow the catalyst with more defects on the catalyst surface, which can serve as active sites for photocatalytic reaction due to their large number of lone pairs electrons. In addition, surface defects can usually affect the energy barrier of CO_2 reduction pathway, altering the selectivity and activity of photocatalysis. Therefore, creating defects by acid etching on the catalysts surface can often significantly modify their photocatalytic activity. Recently, Pang et al. reported a simple acid solution etching method to artificially construct cation vacancies on the surface of the ZnS photocatalyst. [31] The authors used in situ attenuated total reflection-infrared (ATR-IR) spectroscopy and first-principle calculations to unravel the CO_2 reduction pathways into formate and confirmed that the surface cation vacancies could dramatically decrease the barrier of CO_2 reduction and inhibit the proton adsorption, resulting the highly selective CO_2 reduction. Even though there have been several works about acid etched photocatalysts for CO_2 reduction, the works focus on acid etching QDs photocatalysts are still limited. Inspired by their works, we want to apply the similar acid etching method to CdS_xSe_{1-x} quantum dots to construct surface vacancies defect for efficient photocatalytic CO_2 reduction. It is expected that the photocatalytic CO_2 reduction could be enhanced after such acid etching process.

In this study, CdS_xSe_{1-x} colloid quantum dots have been prepared as an efficient photocatalyst for CO_2 reduction to CO. The Cd-vacancies are introduced to improve reaction activity by an acid-etched method. The atomic ratio tests confirmed that Cd vacancies were generated after acid etching. With the introduction of Cd vacancies by acid etching, both selectivity and photocatalytic CO_2 reduction activity increased. The theoretical calculation unraveled that the Cd vacancies could serve as efficient CO_2 reduction active sites while suppressing the competitive H_2 generation reaction. This work provides a simple and effective modification method to improve the efficiency of quantum dot photocatalytic CO_2 reduction works by a simple and effective surface engineering method.

4.2 Experimental section

4.2.1 Material preparation

Typically, 0.8 mL 1.0 M $CdCl_2$ aqueous solution was added to 6 mL of DI water. Then, 1.8 mL 1.0 M mercaptoacetic acid (MAA) was introduced at intense stirring resulting in the formation of a precipitate dissolving upon the addition of 1.0 mL 5.0 M aqueous NH_4OH. Finally, 0.4 mL aqueous 0.5 M Na_2SeO_3 solution was added at vigorous stirring, and the solutions were heated in a 96 °C oil bath for 45 minutes. After the solution was taken out from the oil bath and cooled down to room temperature, 50 mL IPA was added to the solution to form deposition. The deposition was washed several times by IPA and dried in a vacuum oven at 70 °C the whole night. The CdS quantum dots were synthesized by the same method while replacing Na_2SeO_3 solution by the same amount of Na_2S solution. Acid etching was carried out directly over the following method. 100 mg of the prepared CdS_xSe_{1-x} QD powder was suspended in H_2SO_4/IPA solution with different pH value (pH = 0.5, 1, 1.5). The flasks were positioned at the magnetic stirrer and kept constant stirring over the course of 2 h. After etching, the resulting samples were washed and dried overnight in the vacuum oven at 70 ℃.

4.2.2 Photocatalytic activity test

The photocatalytic CO_2 reduction reaction was carried out in a liquid-solid reaction mode in a 120 mL quartz reactor under ambient conditions. Typically, 20 mg of catalyst, 35 mL of DMF, and 7 mL of TEOA were dispersed in a quartz reactor. The reaction solution was sonicated for 30 minutes to obtain a well-dispersed solution. The reactor was then connected to a glass-closed reaction system and then completely removed the air by evacuation for 15 minutes (no O_2 or N_2 can be detected). After that, the closed system was filled with about 101 kPa of pure CO_2 gas. The visible light source irradiation was a 300 W xenon lamp with a UV cut-off filter (L40 filter, $\lambda > 400$ nm), and a cooling water filter was set between the light and the reactor. Gas chromatography (GC-8A, Shimadzu Co., Japan) and (GC-14B, Shimadzu Co., Japan) were used to detect and analyze the amounts of H_2 and CO gas products. The isotope labeling experiment used $^{13}CO_2$ instead of $^{12}CO_2$, and other conditions remained unchanged. The product was detected and analyzed by gas chromatography–mass spectrometry (GC-MS) (JEOL-GCQMS, JMS-K9, 6890N Network GC). The measurement of apparent quantum yield (AQY) was conducted by applying a 300 W xenon arc lamp with monochromatic light band-pass filters (MIF-W, Optical Coatings Japan Co.). The proton (1H) spectra were recorded to determine the reaction solution composition on a 400 MHz nuclear magnetic resonance (NMR) Spectrometor using deuterated water (D_2O) as solvent and dimethyl sulfoxide (DMSO, Sigma, 99.99%) as internal standard reference. The radiant power energy meter (Ushio Spectroradiometer, USR-40) was applied to measure the number of incident photons. The AQY of CO evolution was calculated by the below equation:

$$AQY(\%) = \frac{number\ of\ reacted\ electrons}{number\ of\ incident\ photons} \times 100\%$$

$$= \frac{number\ of\ generated\ CO\ molecules \times 2}{number\ of\ incident\ photons} \times 100\%$$

The selectivity of CO is calculated based on the below equation:

$$Selectivity\ of\ CO\ (\%) = \frac{amount\ of\ generated\ CO}{amount\ of\ generated\ CO\ and\ H_2} \times 100\%$$

4.2.3 Materials characterizations

The X-ray diffraction (XRD) patterns were recorded by powder XRD on the X-ray diffractometer (X'pert powder, PANalytical B.V.). Transmission electron microscopy (TEM) and high-resolution transmission electron microscopy (HRTEM) images of samples were measured from the TEM machine (JEM-2100F, JEOL). UV-Vis absorption spectra were obtained by Ultraviolet-visible spectroscopy (UV-2600, Shimadzu). The decay time spectra were obtained on the Hamamatsu instrument (C5680, Hamamatsu), and the wavelength of excitation light is 400 nm. The chemical states of the prepared samples were recorded on X-ray photoelectron spectroscopy (XPS, Escalab 250 Xi, Thermo Scientific).

4.2.4 Computational details

Density functional theory (DFT) calculations have been performed using the pwscf code of the QUANTUM ESPRESSO package based on the DFT, and plane-wave basis set.[32, 33] The Perdew-Burke-Ernzerhof (PBE) functional of generalized gradient approximation (GGA) was used for exchange-correlation potential.[34] The Projector augmented wave (PAW) method has been employed with the energy cutoff of 50 Ry and charge density cutoff of 500 Ry for geometry structure relaxation.[35] Gaussian smearing with a smearing width of 0.005 Ry was used to speed up the convergence. The DFT-D method of Grimme as a necessary tool is employed for van der Waals (vdW) dispersion correction.[36] The *k*-point sampling of the Brillouin zone was constructed using Monkhorst and Pack mesh scheme.[37] we used 3×3×3 k-point for model relaxation. The convergence limit of energy for the computation is set to 10^{-6} Ry. The free energy of the adsorbed state is calculated as follows:

$$\Delta G = \Delta E + \Delta E_{ZPE} - T\Delta S$$

, where ΔE is the energy change, and ΔE_{ZPE} is the difference corresponding to the zero point energy between the adsorbed state and the gas phase, S is the entropy and T is the temperature.

4.3 Results and discussion

The fabrication process was illustrated in Figure 4.1. The formation mechanism was demonstrated as follows. When the mercaptoacetic acid solution was added into the $CdCl_2$ solution, the Cd(II)-MA white precipitate would generate. Then, the introduction of ammonium hydroxide would form Cd(II)-NH_3-MA complex which was transparent. After the addition of $NaSeO_3$ solution, the solution was transferred to oil bath at 96 °C. Finally, the SeO_3^{2-} was reduced to Se^{2-} by MA anions with the existence of Cd(II) and the Cd(II)-NH_3-MA complex and reduced Se^{2-} would generated CdS_xSe_{1-x} quantum dots during the oil bath treatment. The Figure 4.2a showed the UV-vis spectrum of original CdS_xSe_{1-x} quantum dots solution with the water as baseline. The spectrum showed obvious exciton absorption peak at about 420 nm which is a typical feature of quantum dots, indicating that our QDs were successfully synthesized. As shown in Figure 4.2b, the

CdS_xSe_{1-x} quantum dots solution was transparent in yellow color. The etched samples were named 0.5 QDs, 1.0 QDs, and 1.5 QDs by the pH value of acid solution.

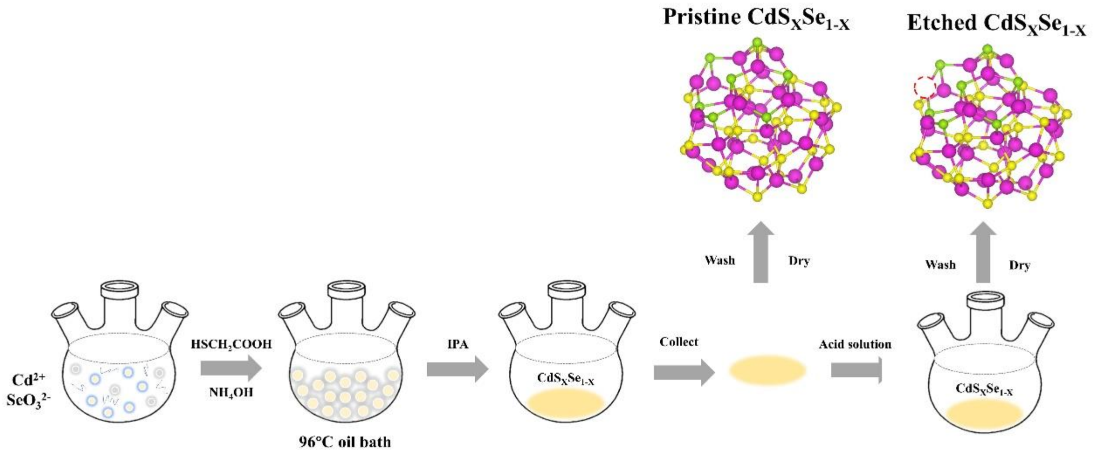

Figure 4.1 Schematic illustration of the fabrication procedure of CdS_xSe_{1-x} QDs and etched CdS_xSe_{1-x} QDs.

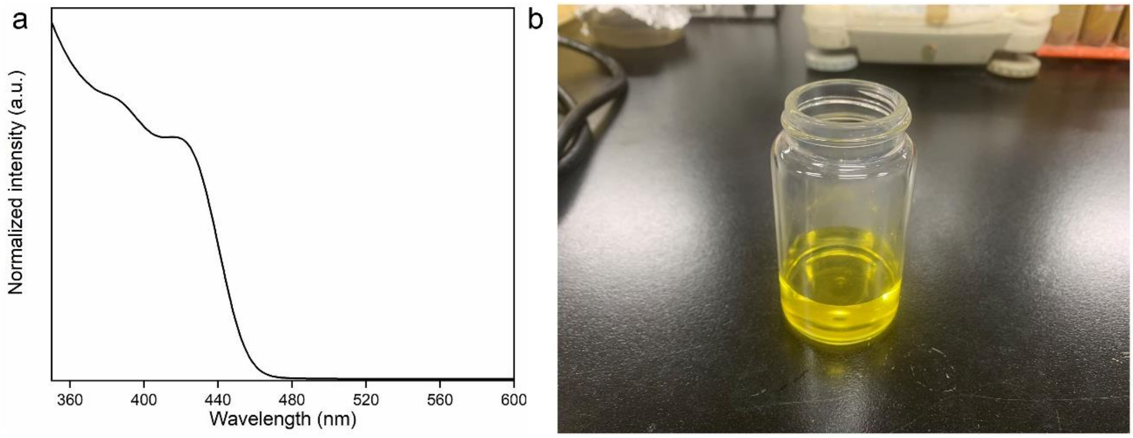

Figure 4.2 (a) UV-vis spectrum and (b) the picture of original CdS_xSe_{1-x} quantum dots solution.

The XRD patterns of each QD sample were shown in Figure 4.3a. The pristine QD sample showed the three characteristic peaks of 25.8°, 41.7°, and 50.2° ascribed to (111), (220) and (311) of a typical cubic sphalerite structure (ICSD No.81925) though the diffraction peaks were broad. [38] The etched samples showed the same peak positions, but slightly weaker characteristic peaks height compared to those of the pristine samples. No other discernable impurity peaks were detected, indicating there was nothing generated during the etching process. The energy dispersive spectrometry (EDS) investigation and X-ray photoelectron spectroscopy (XPS) were used to determine the elemental ratio in pristine QD and etched samples. As shown in Table 4.1, the molar ratio of Cd/(S+Se) was 0.99 in the pristine sample, which was consistent with the stoichiometric ratio. Meanwhile, the molar ratio of Cd/(S+Se) of etched samples exhibited a decreasing trend with the lower pH value of acid solution treatment. The difference in molar ratio between EDS results and XPS results can be attributed to the different detection depth of EDS (ca. 1μm) and XPS (5~10 nm), and the EDS results have more information of the bulk composition while the XPS results have more of the near-surface area. Accordingly, we believed that the removed Cd mainly came from the surface of catalyst, indicating that Cd vacancies generated in the surface of CdS_xSe_{1-x} QDs after acid etching process. For determining the detailed structure of as-prepared QDs, we use the GSAS-II program to make an XRD Rietveld refinement was performed on the pristine QDs sample. The relative information of our samples were shown in Table 4.2, indicating that our as-prepared QDs sample was $CdS_{0.8}Se_{0.2}$ solid solution.

Table 4.1 EDS and XPS analysis of Cd/(S+Se) molar ratio of the pristine CdS_xSe_{1-x} QDs sample and acid etched QDs samples.

Sample	Pristine	1.5 QDs	1.0 QDs	0.5 QDs
EDS	0.99	0.95	0.91	0.88
XPS	0.97	0.91	0.82	0.73

Table 4.2 Atomic percentage and lattice parameters of the pristine CdS_xSe_{1-x} QDs sample and CdS QDs samples.

Samples	Atomic percentage (at%)			Composition	Lattice parameter (Å)	Crystal structure
	Cd	S	Se		a = b = c	
Pristine QDs	49.7	40.0	10.3	$CdS_{0.8}Se_{0.2}$	6.009(7)	Cubic
CdS	49.9	50.1	0	CdS	5.884(6)	Cubic

The morphology of each sample was observed by transmission microscopy (TEM) (Figure 4.3b) The high-resolution TEM (HRTEM) image of the pristine sample showed that the samples gradually crystallize under the electron beam and display distinct lattice stripes, where we observe a planar spacing of 3.40 Å in size. This result was in good agreement with the dense peak located at 25.8° in the X-ray diffraction (XRD) pattern, corresponding to the (111) crystal plane of cubic CdS. The size of the as-synthesized sample varied from 4 nm to 6 nm. The EDS mapping was carried out to confirm the distribution of the composition elements. As shown in Figure 4.3c, the Cd, S and Se elements exhibited a homogenous distribution among the whole sample. According to the above results and the literature reporting this QDs[39], we believed that the as-prepared QDs was colloidal alloy quantum dots.

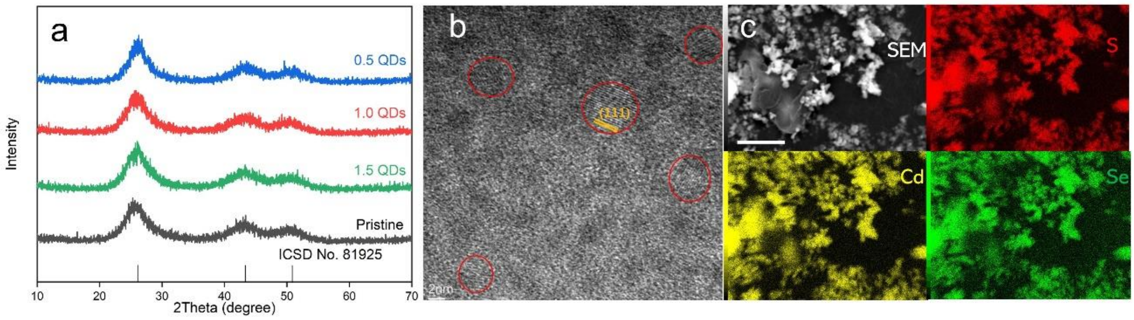

Figure 4.3 (a) XRD patterns the pristine QDs sample and the acid etched QDs samples (b) HRTEM images of pristine QDs. (c) EDS mapping of Cd, S and Se elements. (Scale bar = 5 μm)

The surface states of QDs were examined by XPS analysis. As shown in Figure 4.4, Cd 3d spectrum of QDs showed two distinct peaks at 412.09 eV and 405.26 eV. The 1.0 QDs was selected as the typical sample for comparison. After acid etching, two Cd 3d characteristic peaks shift to 412.18 eV and 405.35 eV, respectively. S 2p spectrum of etched QD shifted from 162.34 eV to 161.77 eV after acid etching. Meanwhile, the Se 3d spectrum of etched QD showed a relatively slight shift from 53.96 eV to 53.81 eV. These shifts indicated that the valence value of Cd slightly increased after acid etching while the valence values of S and Se decreased. According to the studies on elemental ratio that decreasing of Cd contents after acid etching, we proposed the generated Cd vacancies could increase the long pair electrons concentration on S and Se atoms surrounded the Cd vacancies.

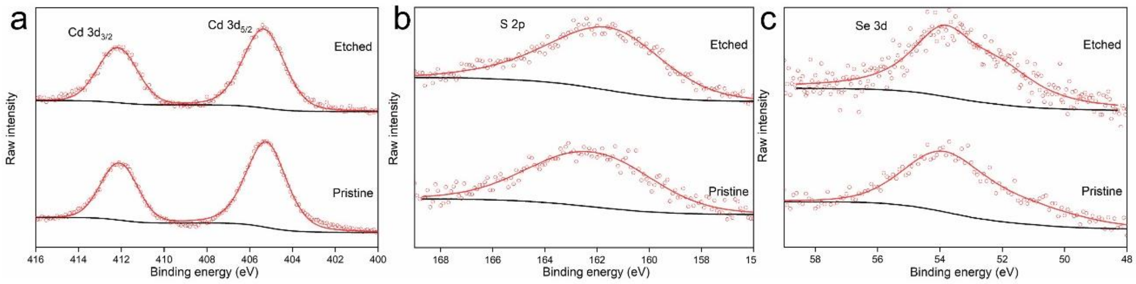

Figure 4.4 XPS spectra of (a) Cd 3d, (b) S 2p, and (c) Se 3d of the pristine QDs sample and the 1.0 QDs sample.

Previous results had proved that acid etching influenced the morphologies and surface states of QD samples. For verifying the effect of Cd vacancies on photocatalytic reactions, we carried out photocatalytic carbon dioxide reduction test to evaluate the influence of Cd vacancies on photocatalytic activity. The $CdS_{0.8}Se_{0.2}$ QD samples were investigated in a DMF solution with triethanolamine (TEOA) as the sacrificial regent and proton donor under visible light irradiation in the pyrex cell. The previous work reported by Fei and coauthor had indicated that the TEOA could donate both protons and electrons in the photocatalytic carbon dioxide reduction reaction. [40] The system using for activity test was shown in Figure 4.5. and the results were shown in Figure 4.6. After 6h light irradiation, the 1.0 QDs system showed the most excellent photocatalytic activity and selectivity, which produced 118.78 μmol CO and 35.28 μmol H_2. The CdS QDs sample was used for comparison and showed much lower activity (Figure 4.6a) It can be concluded that the photocatalytic performance of etched samples exhibited a volcano-type trending, indicating that the excessive amount of Cd vacancies would suppress the photocatalytic ability. No other common CO_2 reduction products (formic acid, methanol, CH_4, and so on) were detected according to NMR test. (Figure 4.7) We use the cycle test of the 1.0 QD sample to evaluate the stability, and the etched sample remained 86.2% activity compared to first test, indicating a good stability. We also use control experiments to show the reaction type. As shown in Figure 4.6b, there was no CO generated without the CO_2 and TEOA, showing the importance of reactant and sacrificial agent in our reaction. Furthermore, there was nothing generated without light irradiation or photocatalyst, indicating that this CO_2 reduction reaction was a photocatalytic reaction. (Figure 4.6c) The $^{13}CO_2$ isotopic test was used to verify the origination of CO. The result in Figure 4.6d indicated that the product CO originated from CO_2 because ^{13}CO was detected while no ^{12}CO indicated that CO was not come from organic component in our system. In addition, we also test apparent quantum yield (AQY) to evaluate the photon utilization efficiency in our photocatalytic CO_2 reduction over etched QD. An AQY as high as 1.66% was reached at the wavelength of 400 nm, indicating a good photon utilization efficiency among representative works about metal sulfide quantum dots for CO_2 photoreduction. (Figure 4.6e) The obtained photocatalytic CO_2 reduction performance over 1.0 QDs without any cocatalyst exceeds that of many represent reported photocatalysts as shown in Table 4.3.

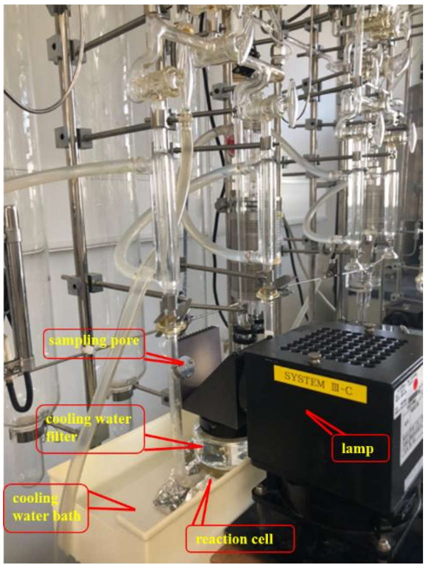

Figure 4.5 The experimental setup for photocatalytic CO_2 reduction.

Table 4.3 Comparison of photocatalytic CO and H_2 evolution rates from CO_2 over different QDs-based photocatalysts.

Photocatalysts	Cocatalyst	Light source	Production	Activity	Ref.
Etched $CdS_{0.8}Se_{0.2}$ QDs	N.A.	300 W Xe lamp ($\lambda > 420$ nm)	CO H_2	$19.79\ \mu mol^{-1}\ h^{-1}$ $5.88\ \mu mol^{-1}\ h^{-1}$	This work
ZnSe QDs	N.A.	AM 1.5G	CO H_2	$240\ \mu mmol^{-1}\ h^{-1}\ g^{-1}$ $960\ \mu mmol^{-1}\ h^{-1}\ g^{-1}$	[26]
ZnSe QDs	N.A.	LED, λ>400 nm	CO H_2	$5.3\ mmol^{-1}\ h^{-1}\ g^{-1}$ $0.02\ mmol^{-1}\ h^{-1}\ g^{-1}$	[27]
Ni:CdS QDs	N.A.	300W Xe lamp	CO	$9.5\ \mu mmol^{-1}\ h^{-1}\ g^{-1}$	[41]
ZnSe QDs	NiCycp	AM 1.5G	CO H_2	$TON_{CO} > 280$ Twice of CO Production	[14]
CdTe QDs	Fe^{2+}	300 W Xe lamp	CH_4 CO H_2	Totally126 $\mu mmol^{-1}\ h^{-1}\ g^{-1}$	[42]
CdSe QDs Aerogel	Ni^{2+}	300 W Xe lamp	CO H_2	$15\ \mu mol^{-1}\ h^{-1}\ g^{-1}$ Trace amount	[43]
CdS QDs	dinuclear cobalt complex	300 W Xe lamp ($\lambda > 420$ nm)	CO CH_4	$4.71\ \mu mol^{-1}\ h^{-1}$ $0.24\ \mu mol^{-1}\ h^{-1}$	[44]
CdS QDs	nickel terpyridine complexes	λ > 400 nm (100 mW cm^{-2})	CO H_2	$0.25\ \mu mol^{-1}\ h^{-1}$ $0.02\ \mu mol^{-1}\ h^{-1}$	[45]

The in situ diffuse reflectance infrared Fourier transform spectroscopy (DRIFTS) investigation was conducted to confirm the reaction process. The 1.0 QDs sample was used as photocatalyst. As shown in Figure 4.6f, the gradually generated peaks centered at 1547 cm^{-1} and 1354 cm^{-1} during the in-situ DRIFTS test are attributed to carbonate-species. And the peak centered at 1744 cm^{-1} were assigned to the adsorbed formate (COOH*) species. [46, 47] These peaks indicated a formation of COOH* intermediate during the photocatalytic CO_2 reduction process over the 1.0 QDs sample.

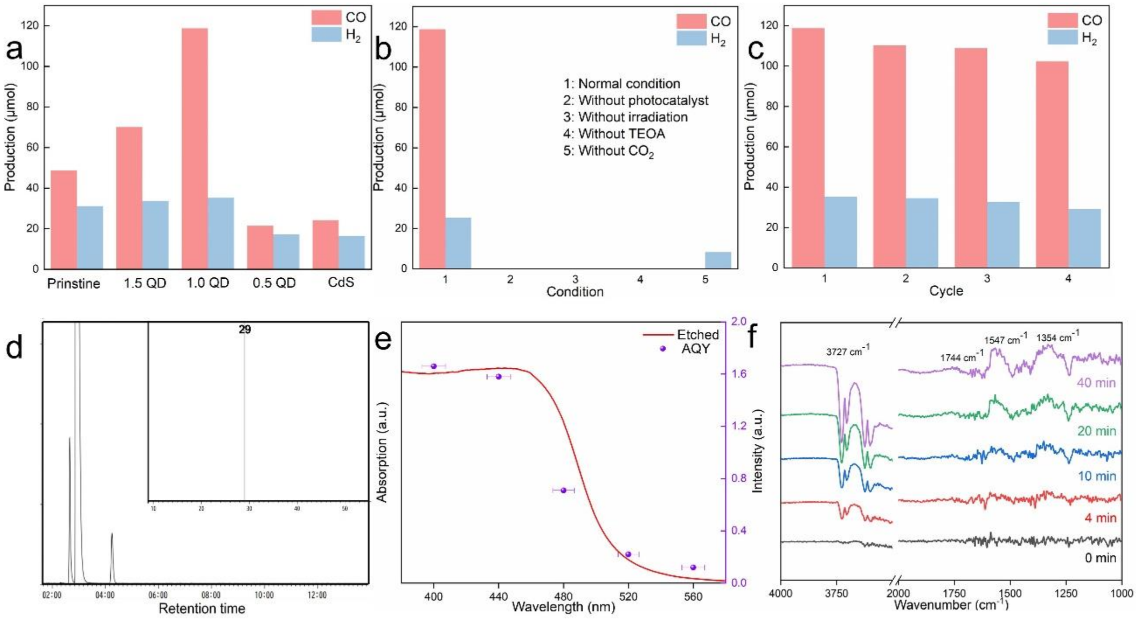

Figure 4.6 (a) Reaction activity of each sample, (b) Control experiment and (c) cycle test over 1.0 QDs sample, (d) GC-MS of CO obtained from photocatalytic reduction of $^{13}CO_2$ over 1.0 QDs sample, (e) UV-vis DRS spectrum and wavelength-dependent AQY of 1.0 QDs sample, (f) In-situ diffuse reflectance infrared Fourier transform spectroscopy for the photocatalytic CO_2 reduction over 1.0 QDs sample.

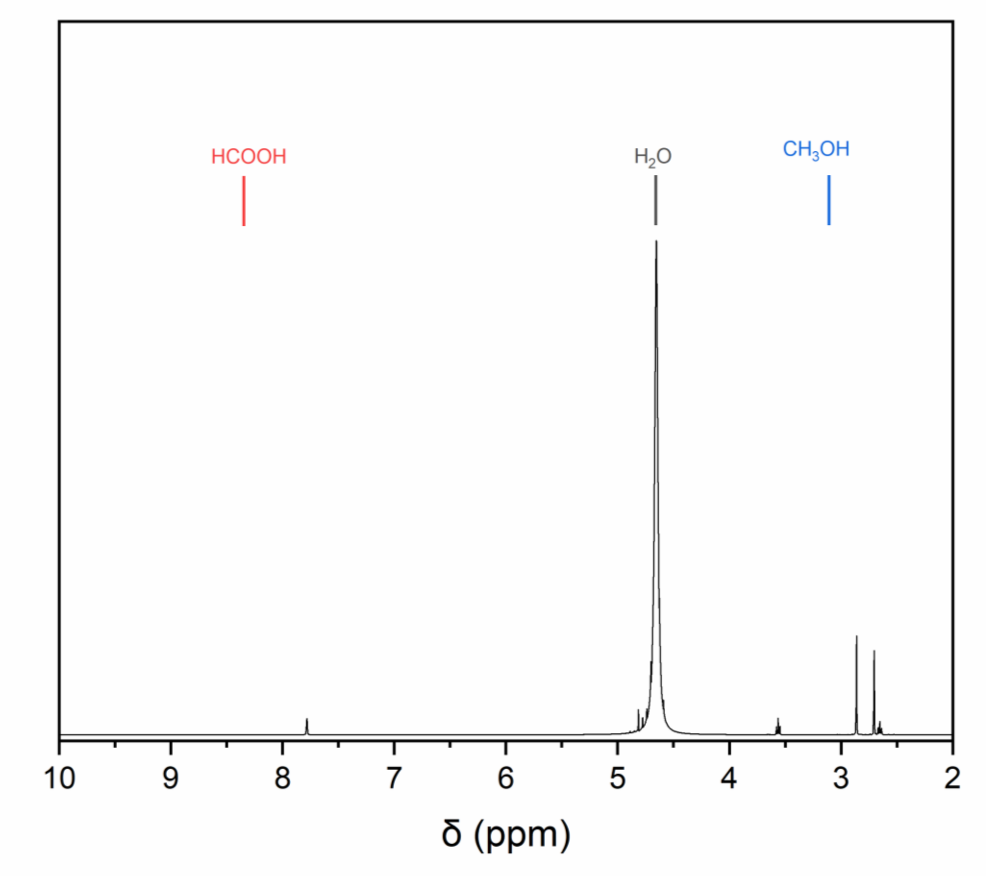

Figure 4.7 1H NMR spectrum of reaction solution.

The photocatalytic CO_2 activity test had proven that the QDs with appropriate Cd vacancies showed more excellent photocatalytic ability compared to pristine QDs. To unravel the influence of Cd vacancies, both experimental characterization and theoretical calculation were carried out. The UV-vis DRS spectra were measured to evaluate their light absorption abilities and shown in Figure 4.8a. As Cd vacancies generated, the light absorption region of etched sample become broad, while the band gaps of etched samples decreased from 2.48 eV to 2.36 eV(by Kubelka-Munk method). Photoluminescence (PL) emission spectra were shown in Figure 4.8b to analyze the photogenerated electron-hole pairs recombination ability of as-prepared QDs. The QDs were excited by the light of 380 nm, and obvious peak centered at about 600 nm were observed. The PL intensity of each sample exhibited the trend as same as that of photocatalytic activity, indicating that the PL intensity may be key factor influencing the photocatalytic performance. Besides, time-resolved transient photoluminescence decay (PL decay) spectra were carried out to analyze the charge carrier lifetime. The 1.0 QDs sample also exhibited the longest lifetime (τ = 2.64 ns) while the 0.5 QDs sample showed the shortest lifetime (Figure 4.8c). The structural defects have a large influence on the lifetime of the charge carriers, because the defects could trap photoinduced charge carriers. [48] Thus, we proposed that the adequate Cd vacancies could prolong the charge carrier lifetime and endow the QDs lower PL intensity and better performance for photocatalytic CO_2 reduction. However, the excessive Cd vacancies trapped too many photo-induced electrons, increasing the chance of charge carrier recombination and lowing the PL intensity. As a result, the 0.5 QDs showed much lower photocatalytic performance compared to other etched QDs sample.

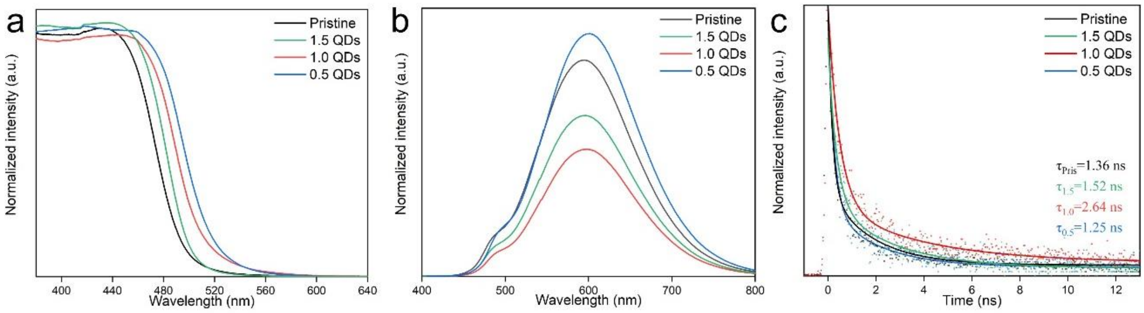

Figure 4.8 (a) Uv-vis DRS spectra, (b) PL spectra and (c) PL decay spectra of pristine sample and etched samples.

Above experimental results had proved that introducing Cd vacancies to QDs could enhance charge carrier separation ability and light absorption ability to improve photocatalytic activity. In order to reveal the influence on reaction kinetics, the DFT calculations were performed. To clarify the effect of Cd vacancies on the kinetics of the CO_2 reduction reaction on the defective QD surface, we calculated the free energy diagram based on the adsorption process of the intermediate. First, we optimized the proton (H) adsorption to elucidate why Cd vacancies can inhibit H_2 production and give high selectivity for the CO_2 reduction reaction. As shown in Figure 4.9a, the free energy of H adsorbed on Cd was closest to zero, indicating that Cd was the reaction active site of H_2 generation in $CdS_{0.8}Se_{0.2}$ QD. We then simulated the CO_2 reduction reaction pathway based on the intermediates of the reaction. The previous in situ DRIFT study had proven the COOH* intermediate generated during the photocatalytic CO_2 reduction process, indicating that the photocatalytic CO_2 reduction process on our QD samples was hydrogen-dissociation path. In particular, CO_2 could be reduced to CO through the following steps: first, the gas phase CO_2 was adsorbed on the surface of catalyst; second, the adsorbed CO_2 (CO_2*) generated adsorbed COOH (COOH*) via a proton-coupled electron transfer (PCET process); then, COOH* was dissociated to CO* and OH*; finally, OH* combines with a proton to form H_2O and CO* was desorbed from surface to form gas face CO. Based on the reaction path way, we carried out first principal study on the $CdS_{0.8}Se_{0.2}$ cluster model with a Cd vacancy. The optimized models were shown in Figure 4.10. And the reduction of CO_2 to CO on Cd vacancy showed much lower energy thermodynamic barrier of 0.58 eV compared to other site, indicating that the Cd vacancy on $CdS_{0.8}Se_{0.2}$ model could decrease energy barrier of CO_2 to CO which is beneficial to CO_2 reduction. (Figure 4.9b) In order to investigate the interaction between the Cd vacancies and adsorbate, the Bader charger analysis was carried out to analysis electrons transfer behavior. The charge transfer amount between adsorbate CO_2 and QD were shown in Table 4.4. We defined the charge shifted from QD to adsorbate as a positive number. The results showed that when the adsorbate was adsorbed by Cd vacancies, the electron transfer between them was significantly stronger than that of other positions, proving that the Cd vacancies generate more lone pairs of electrons due to the absence of Cd. These long pair electrons could transfer to absorbed CO_2 to enhance the reduction reactions. The theoretical research indicated that the introduction of Cd vacancies could enhance CO_2 reduction performance by lowing the energy barrier while inhibiting H_2 generation. Moreover, the Cd vacancies had more electrons for efficient CO_2 reduction. They were the reasons why the introduction of Cd vacancies could enhance the QD's activity and selectivity during the photocatalytic CO_2 reduction process.

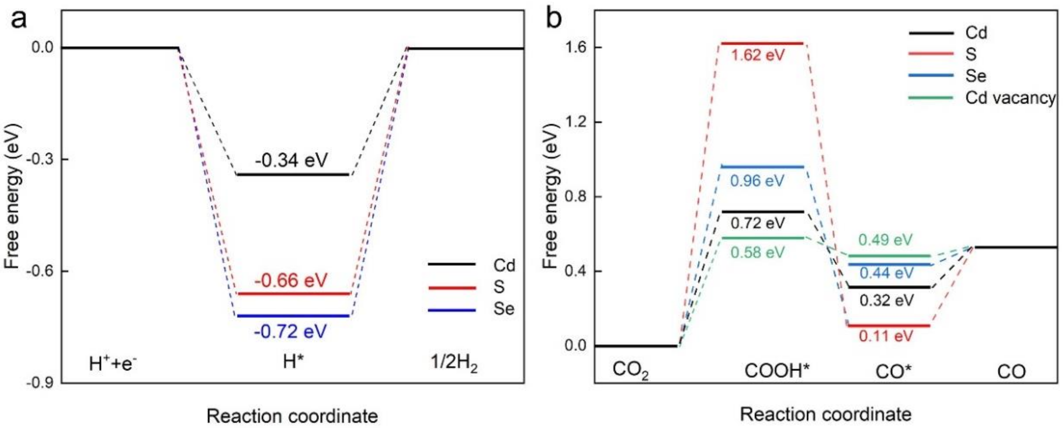

Figure 4.9 (a) H free energy of Cd, S and Se on $CdS_{0.8}Se_{0.2}$ model; (b) Reaction pathways of CO_2 to CO on Cd vacancy contained $CdS_{0.8}Se_{0.2}$ model.

According to experimental and theoretical results, the proposed relationship between photocatalytic CO_2 reduction performance and the introduction of Cd vacancies could be put forward: 1) tailoring light absorption ability and charge carrier separation ability, 2) act as active sites for photocatalytic CO_2 reduction and 3) suppress the H_2 generation reaction. By introducing Cd vacancies to QDs, the light absorption ability was enhanced, and the surface Cd vacancies could trap the photogenerated electrons to prolong the charge carrier lifetime, which was beneficial for the photocatalytic reaction. In addition, according to the DFT calculations, the generated Cd vacancies could act as active sites for photocatalytic CO_2 reduction due to more long pair electrons generated in Se atoms surrounding the Cd vacancies, which showed the lowest energy barrier in the CO_2 reduction reaction. Moreover, the Cd atoms showed the lowest free energy of H*, indicating that Cd atoms were the favorable active site for H_2 generation. The removal of Cd was beneficial for suppressing competitive H_2 generation reaction to enhance the reaction selectivity. The proposed mechanism was shown in Figure 4.11, when the light irradiates the etched QDs, the photo-induced carrier will generate and migrate to the surface of catalyst, and the excited electrons could be trapped by Cd vacancies. The remained photogenerated holes would be consummated by oxidizing TEOA to TEOA*. The Cd vacancies could act as CO_2 reduction active sites, and the trapped excited electrons could transfer to CO_2 to drive the reduction of CO_2 to CO.

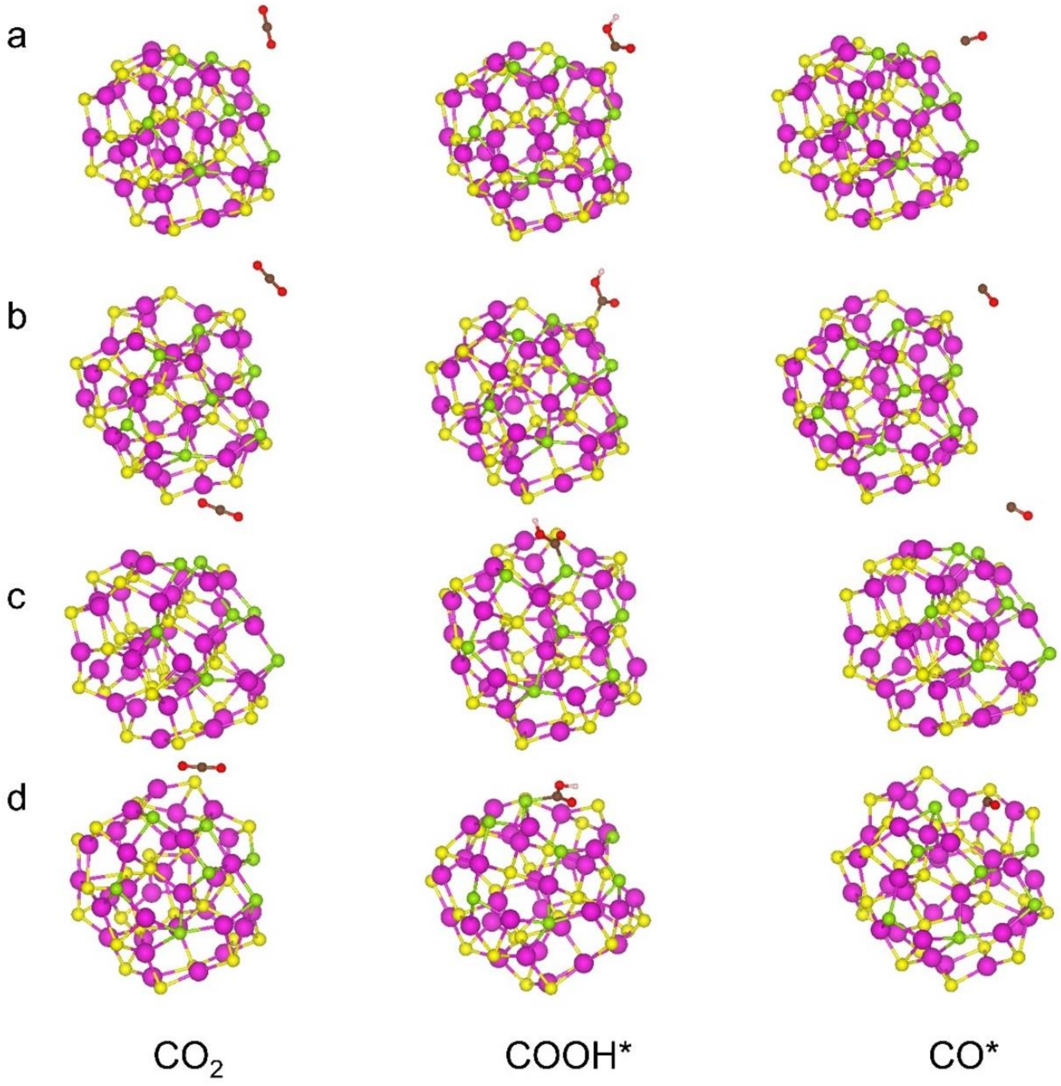

Figure 4.10 Optimized models of CO_2 reduction to CO over (a) Cd site, (b) S site, (Se) site, and (d) Cd vacancy on Cd vacancies contained $CdS_{0.8}Se_{0.2}$ quantum dots.

Table 4.4 Charge transfer between surface site to adsorbed CO_2.

Sites	Cd	S	Se	Cd vacancy
Charge transfer	0.62	0.32	0.11	0.71

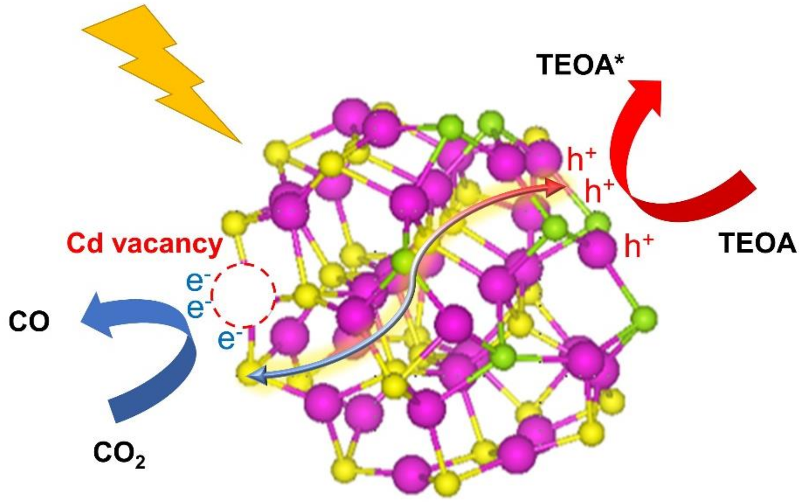

Figure 4.11 Proposed mechanism of CO_2 reduction to CO on Cd vacancies $CdS_{0.8}Se_{0.2}$ quantum dots.

4.4 Conclusions

In conclusion, our study demonstrates an efficient photocatalyst of $CdS_{0.8}Se_{0.2}$ quantum dots with Cd vacancies for CO_2 reduction under visible light. The Cd vacancies were generated by a simple acid etching method, and the etched sample exhibited a higher CO production rate of 19.79 μmol h^{-1} and CO selectivity of up to 77%. Characterization revealed that the Cd vacancies could extend the light absorption region and reduce the charge carrier recombination rate. The DFT calculation indicated that the Cd vacancies reduce the energy barrier of CO_2 reduction and inhibit H_2 generation. These findings provide guidance for the design and construction of highly efficient catalytic materials for CO_2 conversion.

References

[1] X. Jiao, Z. Chen, X. Li, Y. Sun, S. Gao, W. Yan, C. Wang, Q. Zhang, Y. Lin, Y. Luo, Y. Xie, Defect-Mediated Electron-Hole Separation in One-Unit-Cell ZnIn2S4 Layers for Boosted Solar-Driven CO2 Reduction, J Am Chem Soc, 139 (2017) 7586-7594.

[2] Z. Sun, H. Wang, Z. Wu, L. Wang, g-C3N4 based composite photocatalysts for photocatalytic CO2 reduction, Catal. Today, 300 (2018) 160-172.

[3] K. Maeda, Metal-Complex/Semiconductor Hybrid Photocatalysts and Photoelectrodes for CO2 Reduction Driven by Visible Light, Adv Mater, 31 (2019) e1808205.

[4] X. Jiao, K. Zheng, Z. Hu, Y. Sun, Y. Xie, Broad-Spectral-Response Photocatalysts for CO2 Reduction, ACS Cent Sci, 6 (2020) 653-660.

[5] H. Shen, T. Peppel, J. Strunk, Z. Sun, Photocatalytic Reduction of CO2 by Metal-Free-Based Materials: Recent Advances and Future Perspective, Solar RRL, 4 (2020).

[6] S.N. Talapaneni, G. Singh, I.Y. Kim, K. AlBahily, A.H. Al-Muhtaseb, A.S. Karakoti, E. Tavakkoli, A. Vinu, Nanostructured Carbon Nitrides for CO2 Capture and Conversion, Adv Mater, 32 (2020) e1904635.

[7] K. Yang, Z. Yang, C. Zhang, Y. Gu, J. Wei, Z. Li, C. Ma, X. Yang, K. Song, Y. Li, Q. Fang, J. Zhou, Recent advances in CdS-based photocatalysts for CO2 photocatalytic conversion, Chemical Engineering Journal, 418 (2021).

[8] H. Lin, S. Luo, H. Zhang, J. Ye, Toward solar-driven carbon recycling, Joule, 6 (2022) 294-314.

[9] S. Patial, R. Kumar, P. Raizada, P. Singh, Q. Van Le, E. Lichtfouse, D. Le Tri Nguyen, V.H. Nguyen, Boosting light-driven CO2 reduction into solar fuels: Mainstream avenues for engineering ZnO-based photocatalysts, Environ Res, 197 (2021) 111134.

[10] H.L. Wu, X.B. Li, C.H. Tung, L.Z. Wu, Semiconductor Quantum Dots: An Emerging Candidate for CO2 Photoreduction, Adv Mater, 31 (2019) e1900709.

[11] M. Jouyandeh, S.S. Mousavi Khadem, S. Habibzadeh, A. Esmaeili, O. Abida, V. Vatanpour, N. Rabiee, M. Bagherzadeh, S. Iravani, M. Reza Saeb, R.S. Varma, Quantum dots for photocatalysis: synthesis and environmental applications, Green Chemistry, 23 (2021) 4931-4954.

[12] S.S. Brown, A.J. Rondinone, M.D. Pawel, S. Dai, Ternary cadmium sulphide selenide quantum dots as new scintillation materials, Materials Technology, 23 (2013) 94-99.

[13] X.B. Li, Z.J. Li, Y.J. Gao, Q.Y. Meng, S. Yu, R.G. Weiss, C.H. Tung, L.Z. Wu, Mechanistic insights into the interface-directed transformation of thiols into disulfides and molecular hydrogen by visible-light irradiation of quantum dots, Angew Chem Int Ed Engl, 53 (2014) 2085-2089.

[14] M.F. Kuehnel, C.D. Sahm, G. Neri, J.R. Lee, K.L. Orchard, A.J. Cowan, E. Reisner, ZnSe quantum dots modified with a Ni(cyclam) catalyst for efficient visible-light driven CO2 reduction in water, Chem Sci, 9 (2018) 2501-2509.

[15] H. Qin, R.-T. Guo, X.-Y. Liu, X. Shi, Z.-Y. Wang, J.-Y. Tang, W.-G. Pan, 0D NiS2 quantum dots modified 2D g-C3N4 for efficient photocatalytic CO2 reduction, Colloids and Surfaces A: Physicochemical and Engineering Aspects, 600 (2020).

[16] Y. Yuan, R.-t. Guo, Z.-w. Zhang, L.-f. Hong, X.-y. Ji, Z.-d. Lin, W.-g. Pan, Cd0.5Zn0.5S Quantum Dot-Modified CdIn2S4 Nano-octahedron as the 0D/3D Hybrid Heterojunction for CO2 Photoreduction, Energy & Fuels, 35 (2021) 13291-13303.

[17] Y.-C. Chen, H.-H. Chang, Y.-K. Hsu, Synthesis of CuInS2 Quantum Dots/In2S3/ZnO Nanowire Arrays with High Photoelectrochemical Activity, ACS Sustainable Chem. Eng., 6 (2018) 10861-10868.

[18] H. Sheng, M.H. Oh, W.T. Osowiecki, W. Kim, A.P. Alivisatos, H. Frei, Carbon Dioxide Dimer Radical Anion as Surface Intermediate of Photoinduced CO2 Reduction at Aqueous Cu and CdSe Nanoparticle Catalysts by Rapid-Scan FT-IR Spectroscopy, J Am Chem Soc, 140 (2018) 4363-4371.

[19] F. Arcudi, L. Dordevic, B. Nagasing, S.I. Stupp, E.A. Weiss, Quantum Dot-Sensitized Photoreduction of CO2 in Water with Turnover Number > 80,000, J Am Chem Soc, 143 (2021) 18131-18138.

[20] Y.F. Xu, M.Z. Yang, B.X. Chen, X.D. Wang, H.Y. Chen, D.B. Kuang, C.Y. Su, A CsPbBr3 Perovskite Quantum Dot/Graphene Oxide Composite for Photocatalytic CO2 Reduction, J Am Chem Soc, 139 (2017) 5660-5663.

[21] S. Wan, M. Ou, Q. Zhong, X. Wang, Perovskite-type CsPbBr3 quantum dots/UiO-66(NH2) nanojunction as efficient visible-light-driven photocatalyst for CO2 reduction, Chemical Engineering Journal, 358 (2019) 1287-1295.

[22] B. Bhattacharyya, A.K. Simlandy, A. Chakraborty, G.P. Rajasekar, N.B. Aetukuri, S. Mukherjee, A. Pandey, Efficient Photosynthesis of Organics from Aqueous Bicarbonate Ions by Quantum Dots Using Visible Light, ACS Energy Let., 3 (2018) 1508-1514.

[23] A. Li, T. Wang, C. Li, Z. Huang, Z. Luo, J. Gong, Adjusting the Reduction Potential of Electrons by Quantum Confinement for Selective Photoreduction of CO2 to Methanol, Angew Chem Int Ed Engl, 58 (2019) 3804-3808.

[24] R. Li, L. Tang, Q. Zhao, T.H. Ly, K.S. Teng, Y. Li, Y. Hu, C. Shu, S.P. Lau, In2S3 Quantum Dots: Preparation, Properties and Optoelectronic Application, Nanoscale Res Lett, 14 (2019) 161.

[25] S. Lian, M.S. Kodaimati, E.A. Weiss, Photocatalytically Active Superstructures of Quantum Dots and Iron Porphyrins for Reduction of CO2 to CO in Water, ACS Nano, 12 (2018) 568-575.

[26] C.D. Sahm, E. Mates-Torres, N. Eliasson, K. Sokolowski, A. Wagner, K.E. Dalle, Z. Huang, O.A. Scherman, L. Hammarstrom, M. Garcia-Melchor, E. Reisner, Imidazolium-modification enhances photocatalytic CO2 reduction on ZnSe quantum dots, Chem Sci, 12 (2021) 9078-9087.

[27] Z.K. Xin, M.Y. Huang, Y. Wang, Y.J. Gao, Q. Guo, X.B. Li, C.H. Tung, L.Z. Wu, Reductive Carbon-Carbon Coupling on Metal Sites Regulates Photocatalytic CO2 Reduction in Water Using ZnSe Quantum Dots, Angew Chem Int Ed Engl, 61 (2022) e202207222.

[28] H. Pang, X. Meng, H. Song, W. Zhou, G. Yang, H. Zhang, Y. Izumi, T. Takei, W. Jewasuwan, N. Fukata, J. Ye, Probing the role of nickel dopant in aqueous colloidal ZnS nanocrystals for efficient solar-driven CO2 reduction, Appl. Catal., B Environ, 244 (2019) 1013-1020.

[29] L. Lin, Z. Shi, J. Huang, P. Wang, W. Yu, C. He, Z. Zhang, Molecular adsorption properties of CH4 with noble metals doped onto oxygen vacancy defect of anatase TiO2 (1 0 1) surface: First-principles calculations, Applied Surface Science, 514 (2020).

[30] J. Wang, T. Bo, B. Shao, Y. Zhang, L. Jia, X. Tan, W. Zhou, T. Yu, Effect of S vacancy in Cu3SnS4 on high selectivity and activity of photocatalytic CO2 reduction, Appl. Catal., B Environ, 297 (2021).

[31] H. Pang, X. Meng, P. Li, K. Chang, W. Zhou, X. Wang, X. Zhang, W. Jevasuwan, N. Fukata, D. Wang, J. Ye, Cation Vacancy-Initiated CO2 Photoreduction over ZnS for Efficient Formate Production, ACS Energy Let., 4 (2019) 1387-1393.

[32] P. Giannozzi, S. Baroni, N. Bonini, M. Calandra, R. Car, C. Cavazzoni, D. Ceresoli, G.L. Chiarotti, M. Cococcioni, I. Dabo, A. Dal Corso, S. de Gironcoli, S. Fabris, G. Fratesi, R. Gebauer, U. Gerstmann, C. Gougoussis, A. Kokalj, M. Lazzeri, L. Martin-Samos, N. Marzari, F. Mauri, R. Mazzarello, S. Paolini, A. Pasquarello, L. Paulatto, C. Sbraccia, S. Scandolo, G. Sclauzero, A.P. Seitsonen, A. Smogunov, P. Umari, R.M.

Wentzcovitch, QUANTUM ESPRESSO: a modular and open-source software project for quantum simulations of materials, J Phys Condens Matter, 21 (2009) 395502.

[33] P. Giannozzi, O. Andreussi, T. Brumme, O. Bunau, M. Buongiorno Nardelli, M. Calandra, R. Car, C. Cavazzoni, D. Ceresoli, M. Cococcioni, N. Colonna, I. Carnimeo, A. Dal Corso, S. de Gironcoli, P. Delugas, R.A. DiStasio, Jr., A. Ferretti, A. Floris, G. Fratesi, G. Fugallo, R. Gebauer, U. Gerstmann, F. Giustino, T. Gorni, J. Jia, M. Kawamura, H.Y. Ko, A. Kokalj, E. Kucukbenli, M. Lazzeri, M. Marsili, N. Marzari, F. Mauri, N.L. Nguyen, H.V. Nguyen, A. Otero-de-la-Roza, L. Paulatto, S. Ponce, D. Rocca, R. Sabatini, B. Santra, M. Schlipf, A.P. Seitsonen, A. Smogunov, I. Timrov, T. Thonhauser, P. Umari, N. Vast, X. Wu, S. Baroni, Advanced capabilities for materials modelling with Quantum ESPRESSO, J Phys Condens Matter, 29 (2017) 465901.

[34] J.P. Perdew, Burke, K., & Ernzerhof, M., Generalized gradient approximation made simple, Physical review letters, 77 (1996) 3865-3868.

[35] P.E. Blochl, Projector augmented-wave method, Phys Rev B Condens Matter, 50 (1994) 17953-17979.

[36] S. Grimme, J. Antony, S. Ehrlich, H. Krieg, A consistent and accurate ab initio parametrization of density functional dispersion correction (DFT-D) for the 94 elements H-Pu, J Chem Phys, 132 (2010) 154104.

[37] H.J. Monkhorst, J.D. Pack, Special points for Brillouin-zone integrations, Physical Review B, 13 (1976) 5188-5192.

[38] S. Wang, X. Wang, Photocatalytic CO 2 reduction by CdS promoted with a zeolitic imidazolate framework, Appl. Catal., B Environ, 162 (2015) 494-500.

[39] A.E. Raevskaya, O.L. Stroyuk, Y.V. Panasiuk, V.M. Dzhagan, D.I. Solonenko, S. Schulze, D.R.T. Zahn, A new route to very stable water-soluble ultra-small core/shell CdSe/CdS quantum dots, Nano-Structures & Nano-Objects, 13 (2018) 146-154.

[40] H. Fei, M.D. Sampson, Y. Lee, C.P. Kubiak, S.M. Cohen, Photocatalytic CO2 Reduction to Formate Using a Mn(I) Molecular Catalyst in a Robust Metal-Organic Framework, Inorg. Chem., 54 (2015) 6821-6828.

[41] J. Wang, T. Xia, L. Wang, X. Zheng, Z. Qi, C. Gao, J. Zhu, Z. Li, H. Xu, Y. Xiong, Enabling Visible-Light-Driven Selective CO2 Reduction by Doping Quantum Dots: Trapping Electrons and Suppressing H2 Evolution, Angew Chem Int Ed Engl, 57 (2018) 16447-16451.

[42] Y. Bao, J. Wang, Q. Wang, X. Cui, R. Long, Z. Li, Immobilization of catalytic sites on quantum dots by ligand bridging for photocatalytic CO2 reduction, Nanoscale, 12 (2020) 2507-2514.

[43] G. Jiang, J. Wang, N. Li, R. Hübner, M. Georgi, B. Cai, Z. Li, V. Lesnyak, N. Gaponik, A. Eychmüller, Self-Supported Three-Dimensional Quantum Dot Aerogels as a Promising Photocatalyst for CO2 Reduction, Chemistry of Materials, 34 (2022) 2687-2695.

[44] Q.-Q. Bi, J.-W. Wang, J.-X. Lv, J. Wang, W. Zhang, T.-B. Lu, Selective Photocatalytic CO2 Reduction in Water by Electrostatic Assembly of CdS Nanocrystals with a Dinuclear Cobalt Catalyst, ACS Catalysis, 8 (2018) 11815-11821.

[45] M.F. Kuehnel, K.L. Orchard, K.E. Dalle, E. Reisner, Selective Photocatalytic CO2 Reduction in Water through Anchoring of a Molecular Ni Catalyst on CdS Nanocrystals, J Am Chem Soc, 139 (2017) 7217-7223.

[46] B. Han, X. Ou, Z. Deng, Y. Song, C. Tian, H. Deng, Y.J. Xu, Z. Lin, Nickel Metal-Organic Framework Monolayers for Photoreduction of Diluted CO2 : Metal-Node-Dependent Activity and Selectivity, Angew Chem Int Ed Engl, 57 (2018) 16811-16815.

[47] Y. Liu, S. Chen, X. Quan, H. Yu, Efficient Electrochemical Reduction of Carbon Dioxide to Acetate on Nitrogen-Doped Nanodiamond, J Am Chem Soc, 137 (2015) 11631-11636.

[48] J. Du, S. Ma, H. Liu, H. Fu, L. Li, Z. Li, Y. Li, J. Zhou, Uncovering the mechanism of novel AgInS2 nanosheets/TiO2 nanobelts composites for photocatalytic remediation of combined pollution, Appl. Catal., B Environ, 259 (2019) 118062.

Chapter 5 Conclusions and future prospects

5.1 General conclusions

In this thesis, the main objective is to construct ternary metal sulfides with suitable electronic structures and abundant reaction sites by tuning the metal element ratios and surface defect engineering and applying them to photocatalytic CO_2 reduction. The results of this study provide new insights into the design of metal sulfide based photocatalysts and highlight the importance of tuning the electronic structure for the photocatalytic reduction of CO_2. The detailed study can be concluded in the following parts.

1. Selective conversion of CO_2 to CO under visible light by modulating Cd to In ratio: A case study of Cd-In-S colloidal catalysts

In this part, Cd-In-S colloids samples with different Cd to In ratio were constructed for high-efficient visible-light-driven CO_2 reduction. The CO production rate achieved 22.9 $\mu mol \cdot h^{-1}$ at the optimized condition when using $Co(bpy)_3^{2+}$ as cocatalyst. Furthermore, an AQY up to 1.75% was reached at a wavelength of 400 nm. The mechanistic investigation revealed that by the introduction of Cd, both the electronic structure of Cd-In-S solid solution and the charge transfer behavior between Cd-In-S and cocatalysts could be modulated, which synergistically determines the overall catalytic performance. The findings in this work offer a unique insight into the construction and modulation strategy of bimetallic sulfide-based photocatalysts toward CO_2 reduction.

2. Nanoscale Ag-In-S quantum dots towards efficient photocatalytic CO_2 reduction with Ag/In molar ratio dependent activity and selectivity

In this part, non-stoichiometric Ag-In-S QDs were synthesized as photocatalysts for efficiency. The introduction of CoBPY into the reaction system not only promotes the conversion of CO_2 to CO reaction but also improves the photo-stability of Ag-In-S QDs. The photocatalytic syngas production rates and the selectivity of CO are strongly dependent on the Ag to In molar ratios in Ag-In-S QDs, and the 2Ag-In-S QDs sample with the Ag to In molar ratio of 0.154:1 exhibits the highest CO production rate of 9.20 $\mu mol\ h^{-1}$ and H_2 production rate of 3.13 $\mu mol\ h^{-1}$, which outperform most of the reported QDs based photocatalysts. The mechanism investigation reveals that the increasing of Ag to In molar ratios in Ag-In-S QDs leads to the enhanced light absorption ability, the increased lifetime of photogenerated charge carriers, and the decreased reduction potential of electrons, which play competitive roles in the photocatalytic syngas production reaction.

3. Construction surface vacancies on colloid CdS_xSe_{1-x} quantum dots for efficient photocatalytic CO_2 reduction

In this part, an efficient photocatalyst of CdS_xSe_{1-x} quantum dots with Cd vacancies for CO_2 reduction under visible light were demonstrated. The Cd vacancies were generated by a simple acid etching method, and the etched sample exhibited a higher CO production rate of 19.79 μmol h^{-1} and CO selectivity of up to 77%. Characterization revealed that the Cd vacancies could extend the light absorption region and reduce the charge carrier recombination rate. The DFT calculation indicated that the Cd vacancies reduce the energy barrier of CO_2 reduction and inhibit H_2 generation. These findings provide guidance for the design and construction of highly efficient catalytic materials for CO_2 conversion.

5.2 Future prospects

Although some achievements have been made in developing efficient metal sulfide for CO_2 reduction, there are many challenges towards the significant enhancement of photocatalytic CO_2 reduction.

(1) Up to now, it is still dramatically challenging to achieve overall photocatalytic CO_2 reduction in the current heterogeneous liquid-solid reaction system. The main reason is that the photogenerated holes left after the photoelectron reaction cannot be easily consumed. These remaining holes would oxidize the catalyst and cause photocorrosion of the catalyst if they are not consumed in time. Currently, the common practice is to add a sacrificial agent to the reaction for small photogenerated holes. However, the oxidation products of these sacrificial agents are usually complex and of little use, resulting in considerable waste. To solve this problem, one better approach is to develop novel CO_2 reduction photocatalysts with the ability to oxidation of the sacrificial agent to the specified product.

(2) There are still many possibilities for semiconductor quantum dots to be explored for photocatalytic CO_2 reduction. In our works, we have applied two approaches including elemental ratio modification and acid etching to modify quantum dots for enhancing photocatalytic CO_2 reduction ability. More approaches can be used on quantum dots to

gain a more understanding of photocatalytic CO_2 reduction. For example, template etching QDs, construction of QDs/MOF(COF) structure, and core-shell structure QDs.

(3) Although we have applied the acid-etching method to make surface defects and achieved high photocatalytic performance, it was still not accurate enough to make defects. More approaches can be explored, such as hydrothermal synthesis, elemental doping, and organic etching, to gain more controllable surface defects to promote photocatalytic CO_2 reduction.

Acknowledgment

After 4.5 years life in NIMS/Hokkaido university, I will finish my Ph.D. candidate period. This is my first time to study and live in a foreign country. I won’t get the Ph.D. degree without everyone’s help. Here, at the end of my Ph.D. thesis, I would like to express my gratitude to those who have helped me a lot in my daily life and studies.

First of all, I would like to express my most sincere gratitude to my supervisor Prof. Jinhua Ye. Thank you for giving me the opportunity to conduct my Ph.D. study at Hokkaido University and NIMS. Thank you for your valuable guidance, fruitful discussions, incredible patience, and continuous encouragement throughout my study. In fact, I almost give up my Ph.D. at the 3rd degree due to my laziness and lack of confidence while I also caused a lot of trouble. However, I finally finished my Ph.D. thesis and defense under your continuously patient guidance. I would like to say you are the best supervisor in the world. The time I studied under your supervising is the most valuable treasure in my life.

I am also grateful to my supervisors, Prof. Kiyoharu Tadanaga and Prof. Naoto Shirahata. Thank you for all your suggestions and kind help during my PhD study. I would like to thank the support from National Institute for Materials Science during my PhD study.

Then, I also want to thank all the members in the Photocatalytic Materials Group in NIMS and the persons who have helped me. I will give special thanks to Dr. Shunqin Luo and Dr. Xiaohui Ren for their important advice in my paper and Ph.D. They help me a lot in daily study and life. Thanks for Mr. Bowen Deng and Mr. Davin Philo who company me together to get the Ph.D. degree. Thanks for Dr. Li Shi who help me designing and teaching me the photocatalysis research. I will cherish these memorable days with you forever. I would like to express my thanks to Dr. Huiwen Lin, Dr. Gaoliang Yang, Dr. Yunxiang Li, Dr. Sijie Li, Dr. Shuang Song, Dr. Yu He, Dr. Lan Li, Dr. Shengyao Wang, Dr. Xusheng Wang, Dr. Yiming Zhang, Dr. Hong Pang, Dr. Fumihiko Ichihara, Dr. Tetsuya Kako, Dr. Mitsutake Oshikiri, Ms. Kanae Hasegawa and Ms. Haruna Kaunang for their kind helps in both experiments and daily life.

I also want to give my thanks for my friend, Mr. Qi Li and Mr. Yi Wang. You are my important friends in my life. I thank my seniors Dr. Bo Zhu, Dr. Xiaofang Su, Dr. Yu

Tian for their help in theoretical calculations. I also give thanks to Mr. Yue Liu, Mr. Xuming Mao and Mr. Jiayi Wang for daily life.

Finally, I would like to express my deepest gratitude to my dearest family members, my grandparents, my aunt, my uncles, my siblings and also my parents. Thank you for your eternal love and constant encouragement during my Pd.D. candidate period. Your love is the source of my happiness.

Finishing Ph.D. degree is just a start, but not end. I hope to be a useful person to my motherland and people. Just like a famous chinese poetry saying: 苟利国家生死以，岂因祸福避趋之。